Max-Planck-Institut für Kolloid- und Grenzflächenforschung

Functional Nanoporous Carbon-Based Materials derived from Oxocarbon-Metal Coordination Complexes

Dissertation

zur Erlangung des akademischen Grades
Doktor der Naturwissenschaften
(Dr. rer. nat.)
in der Wissenschaftsdisziplin „Kolloidchemie“

eingereicht an der
Mathematisch-Naturwissenschaftlichen Fakultät
der Universität Potsdam

von

Christian Mbaya Mani

Geboren am 27.01.1988 in Kinshasa, D.R. Kongo

Potsdam-Golm, im September 2017

Dedicated to my family

“The important thing in science is not so much to obtain new facts as to discover new ways of thinking about them”

Sir William Henry Bragg

Acknowledgements

I would like to thank **Prof. Dr. Markus Antonietti** for the opportunity to work in his group and for his support, supervision, and all the contributions to the success of the present thesis. It has been a great honor and inspiration to work with you.

My particular thanks go to **Dr. Nina Fechler** for the excellent supervision, countless support and the many fruitful discussions. I really appreciate that I could always knock on your door and count on your advice. Thank you for the comments, criticism and hard questions which caused me to look at my research from innovative and uncommon perspectives.

I thank **Prof. Andreas Taubert** and **Prof. Arne Thomas** for agreeing to examine my dissertation.

I am grateful to **Dr. Valerio Molinari** and **Dr. Martin Oschatz** for the many scientific (and sometimes also very non-scientific) discussions in the hallways, laboratories, offices, Chez Briel and on various balconies of the Max-Planck-Institute. Thanks to **Carolin Nuglisch** for proofreading my thesis and for the moral support. My sincere thanks also go to my group members **Dr. Thomas Jordan** and **Thomas Berthold** as well as to my office mates **Dr. Jochen Willersinn** and **Hui-Chun Lee** for the amazing teamwork, the myriad of laughter, and the inspiring discussions we had about work, family and life. Furthermore, I would like to thank **Regina Rothe** for the constant support in the laboratory and the personal encouragement throughout the whole PhD time. Many thanks to **Heike Runge** and **Rona Pitschke** for the introduction into the SEM and TEM devices and for the many images you recorded for me. Thanks to **Max Braun** for introducing me into the world of the heterogeneous catalysis. A huge thank to all the past as well as present colleagues who have contributed to an excellent and entertaining working environment. I sincerely thank my friends Haddom, Ornella, Mitch, Mario, Kevin, Marcel, Moh, André, Nevena (Olga), Konrad (Jason), and Arno, for being there when I needed you the most.

Finalement, je remercie **Dieu** pour la bonne santé et la force qu'il m'a donné de persister et persévérer dans me buts. Merci à **mes parents** et à mes sœurs **Julia et Odaline**; vous êtes la vraie source de ma force et de ma motivation de toujours vouloir atteindre plus. *Je vous aime*.

Table of Contents

1. Introduction

From stone to silicon, materials have fundamentally shaped the history of human civilization and affect how we build, eat, progress, work, and communicate. Each new era has been dominated by a new class of materials which possessed better and more developed properties than the materials of the preceding ages. Each era has brought up a number of innovations which revolutionized the landscape of human civilization from both the social and economic point of view. While the 20th century has been significantly marked by silicon based materials, in the course of the 21st century the spotlight has shifted to another class of materials which is about to dominate a new industrial era referred to as the "new carbon age".[1, 2]

Carbon is the fourth most abundant element in the universe and of fundamental importance for life on earth.[3] It can possess a range of outstanding properties and is becoming the material of choice in a wide spectrum of applications, ousting silicon and dominating developments in both modern science and industry.[2, 4, 5] As a chemical element, carbon possesses at least three stable bonding schemes given by the hybridization states (sp^3, sp^2 and sp) which can be easily transformed into each other by variation of temperature and pressure or via chemical reactions, thus allowing for the flexible formation of various shapes and geometries. In addition, carbon possesses the exceptional ability to form stable bonds with itself and other elements (e.g. H, O, N, B, metals, etc.) in many different ways, thus giving rise to a variety of compounds and nanostructures.[6] These points are important as they allow for the control of structure and chemical functionality with the highest chemical resolution i.e. precision down to the Angstrom level.[7] Among the different carbon forms, the sp^2 (graphite, nanotube, fullerene) and sp^3 (diamond) allotropic configurations (**Figure 1.1**) attracted much interest as each of them exhibits a list of remarkable properties.[8] For instance, carbon nanotubes possess extraordinary high stiffness and can be 60 times stronger than steel wire.[9] Furthermore, they exhibit high thermal and electrical conductivity, which can be either semi-conducting or metallic depending on the graphitic structure.

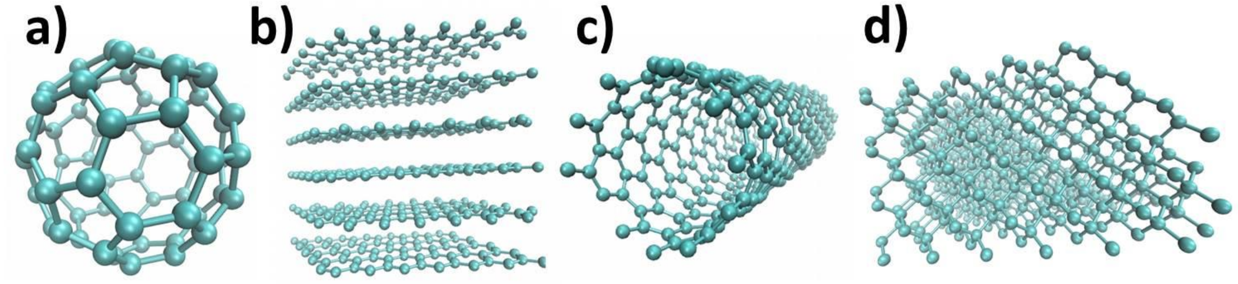

Figure 1.1 Allotropes of carbon with (a) Fullerene, (b) Graphite, (c) Nanotube, and (d) Diamond.

Humans have been practically using carbon-based materials in different structures and forms already since the pre-historic area, for instance as ink in cave paintings around 28,000 years BP or for water purification purposes in ancient Egypt around 2,000 BC. [10,11] However, the full bandwidth of properties and possible applications associated with the different carbon structures are just becoming apparent. With expanding research, better scientific understanding, developments in the field of nanotechnology, and improved equipment new materials are emerging on the basis of the many allotropes of carbon.[7] Nowadays, carbon-based materials can be encountered in form of powders, fibers, foams, fabrics, or composites in almost every aspect of our modern civilization. In this context, they provide the strongest fibers, one of the best gas storage medium, the best electrically conducting material, and the basis for a promising energy storage system.[12, 13]

Nanoporous carbon materials are of particular interest for both science and industry owing to their exceptional features such as high surface area, high pore volume, high chemical stability as well as high electric and thermal conductivity.[14, 15] In industry, nanoporous materials proved to be technologically useful for a wide spectrum of applications including energy storage and conversion in fuel cells, Li-ion batteries and super-capacitors, for catalysis, sorption and separation technologies, in electronic and magnetic devices.[16-18] Despite the fact that these technological advances enable greater living standards, they come along with some severe challenges that menace our environment as well as the welfare of the upcoming human generations. One of the major issues overshadowing our modern industrialized society in the 21st century includes the expansive material and energy consumption which lead to an increasing demand for these goods. This can largely be attributed to the growing global population:

According to the United Nations Department of Economic and Social Affairs, Population Division, human population is estimated to grow by ca. 23 % to 9.2 billion in 2050.[19] Along with the exponential consumption of materials and energy, we are about to experience a rapid depletion of non-renewable fossil resources including water, coal, minerals, natural gas, and oil. It is widely acknowledged that we will run short on oil, if we maintain the current demand.[20] Moreover, burning fossil fuels releases carbon dioxide (CO_2) into the atmosphere which is reported to be the driving force for global warming and climate changes.[21] In order to meet the growing demand for goods without both being limited by the supply of the needed raw materials and harming the environment, modern science is obliged to find new synthesis routes which employ existing raw materials more efficiently and make use of substances which are abundant in nature.

The preparation of nanoporous carbons classically involves thermal carbonization of the carbon precursors at elevated temperatures and an activation step. Owing to the relatively unpredictable processes at such high temperatures, thermal carbonization is often compared to “synthesis in a black box”, thereby giving no access to observe or to intervene in the course of the reaction during the heat treatment. This makes it difficult to control structural and textural properties of the product carbon materials. The resulting carbons mostly exhibit a disordered pore structure with a relatively broad pore size distribution. In order to gain more control over the pore structure, so called hard and soft templates can be employed in the synthesis, yielding ordered porous carbon materials with a narrow pore size distribution and well-accessible pore structures and large surface areas. [22, 23] However, this approach requires numerous synthesis steps including the controlled synthesis of the template materials beforehand and their removal afterwards, which is why it can be considered as laborious, costly, and to a certain extend environmentally harmful. Furthermore, depending on the precursor material, only low carbonization yields can be achieved as most molecules are released as volatile fragments. A simple, efficient and sustainable approach for the synthesis of porous carbons is the hydrothermal carbonization (HTC) approach. It involves the decomposition and conversion of carbohydrates under mild conditions to structured carbons. By using sodium borate (borax) as catalyst in the hydrothermal carbonization of glucose, Antonietti *et al.* prepared porous carbon aerogels with high specific surface areas and total pore volumes without the use of classical hard or soft templates.[24, 25] Moreover, this strategy provides the possibility to control the porosity and introduce nitrogen functional groups by tuning the ratio sugar/borax and sugar/nitrogen source, respectively.[26]

For the rational design of nanoporous carbons, the general idea is to define and adjust the functional properties of the carbons (e.g. electrical conductivity, bad gap, and their specific interaction with other molecules) in the earliest preparation steps as possible on the molecular level.[7] One possible approach to achieve this includes the use of precursor materials with pre-defined structural and compositional characteristics (e.g. surface polarity and pore structure).[27] Recently, ionic liquids (ILs) have been introduced as promising precursor materials for the synthesis of nanoporous carbon materials.[28] ILs are salts which are liquid below 100 °C and possess a negligible vapor pressure as well as high thermal stabilities. These characteristics facilitate the processing of these compounds (i.e. casting, molding, or printing), whereby high carbonization yields can be achieved upon thermal carbonization of the ILs. Furthermore, the in-situ introduction of heteroatoms such as nitrogen (N) and boron (B) is possible by appropriate cation/ion combinations, thus allowing for a wide spectrum of carbon nanostructures.[29] In order to control and improve the pore structure, salt templating was proven to be a powerful approach. Here, ordinary salts such as sodium chloride (NaCl), potassium chloride (KCl), and zinc chloride ($ZnCl_2$) can serve as porogens as well as high temperature solvents in mixtures with the carbon precursors leading to porous heteroatom-doped carbons with high surface areas of up to 2000 m^2 g^{-1}.[30, 31] As shown by Fechler *et al.* in 2013, the pore structure can be easily tuned by the choice as well as amount of the template salt used, whereby the resulting aerogel-like products were shown to outperform conventional N-doped carbons with regard to their activity in the oxygen reduction reaction (ORR).[30, 32] Despite the numerous advantages associated with the use of ILs as precursor to produce nanoporous carbon materials with high surface areas and good carbon yields, commercial ILs are quite expensive. In the attempt to reduce the costs, Esposito *et al.* reported the synthesis of ILs based on symmetric, bifunctional imidazolium compounds that were derived from natural amino acids as green starting materials.[33] These compounds were successfully used as carbon precursors, whereby N-doped carbons with N contents of up to 17 wt% could be achieved with very high surface areas of up to 2650 m^2g^{-1} by using the salt templating approach.[34]

Another class of promising precursor materials allowing to define the material properties by the choice of the molecular building blocks are crystalline porous compounds that possess a high carbon content. Particularly crystalline materials, which are constituted of an organic compound coordinated to a metal ion are beneficial from the standpoint of material design, because they exhibit a wide range of chemical and physical properties which can be easily tuned by proper crystal engineering.[35-37] As a prominent example for this class of materials, metal-organic frameworks (MOFs) have shown to serve as both a sacrificial template and a carbon precursor itself for the production of various carbon based nanomaterials with advanced properties.[38, 39] In this context, Yamauchi *et al*. reported on the synthesis of amorphous nanoporous carbons by the direct carbonization of a zeolitic imidazolate framework (ZIF-8).[40] The resulting microporous carbons were reported to possess high surface areas of 1110 m^2 g^{-1}. Recently, various MOFs such as MOF-5, HKUST-1 as well as the MIL and ZIF series have successfully been used as carbon precursors in the synthesis of nanoporous carbons and showed much promise in their applications in gas adsorption, catalysis, and energy storage.[16, 41, 42] By using heteroatom-rich MOFs as precursors, heteroatom-doped carbons were prepared with high surface areas and high heteroatom contents, thus enhancing the physicochemical properties of the final products.[43, 44] However, MOFs generally suffer from very low thermal stabilities which make it difficult to control the transformation processes during the heat treatment and therefore the morphologies and properties of the resulting porous carbons.[45]

Driven by the motivation to overcome these limitations, in our research group, we developed an alternative synthetic strategy that is based on the use of mesocrystalline microparticles as carbon precursors. In this context, we synthesized coordination complexes constituted of a natural polyphenol, namely ellagic acid, coordinated to zinc ions.[46] Via control of the synthesis conditions, their self-assembly behavior could be tailored into round and elongated “peanut”-like mesocrystals. The subsequent heat treatment of these mesocrystals under an inert atmosphere yielded hierarchically porous carbon nanomaterials in high yields with a bimodal micro- and mesoporous architecture without any additional templating or washing step. Moreover, the morphologies of the pristine mesocrystals could be preserved throughout the whole synthesis procedure. The resulting porous carbons were shown to possess promising properties such as high mass transport and uptake which was demonstrated by high CO_2 gas adsorption.

1.1. **Outline**

This thesis aims to establish a facile and alternative strategy for the synthesis of functional nanoporous carbon materials with defined and controllable properties. Inspired by the preceding work of Yang *et al.*, mesocrystalline structures based on metal-coordination complexes with pre-defined structural information are herein employed as carbon precursors.[46] Following the concepts of molecular material design, the properties of the resulting carbonaceous nanomaterials can be easily tuned by controlling the way in which the constituent molecules arrange. The resulting mesocrystals possess overall three-dimensional (3D) structures which are defined by strong non-covalent intermolecular interactions between the constituent building units, including coordination and hydrogen bonding giving rise to highly stable and robust materials. These structures can be subsequently transformed into the corresponding porous carbon materials while the pre-defined properties are preserved.

A schematic representation of the herein developed synthesis strategy is depicted in **Figure 1.2**. As already stated above, this concept was already published by Yang *et al.* in 2015 and is presented herein in a broader context.[46] In this work, squaric acid and croconic acid, respectively, are used as multi-functional organic ligands to form stable crystalline particles based on coordination complexes various divalent 3d block metal ions including Zn^{2+}, Cu^{2+}, and Ni^{2+}. In these early steps, materials properties such as structure, morphology, and texture can be adjusted by controlling the crystal formation and growth processes. This can be achieved by choosing appropriate synthesis conditions including solvent, temperature, counterion, organic ligand and metal ion concentration. The resulting crystals are subsequently heat treated at elevated temperatures in a nitrogen (N_2) atmosphere yielding a carbon composite material. The latter can be further treated to yield a purely carbon material while preserving the characteristics of the pristine crystals.

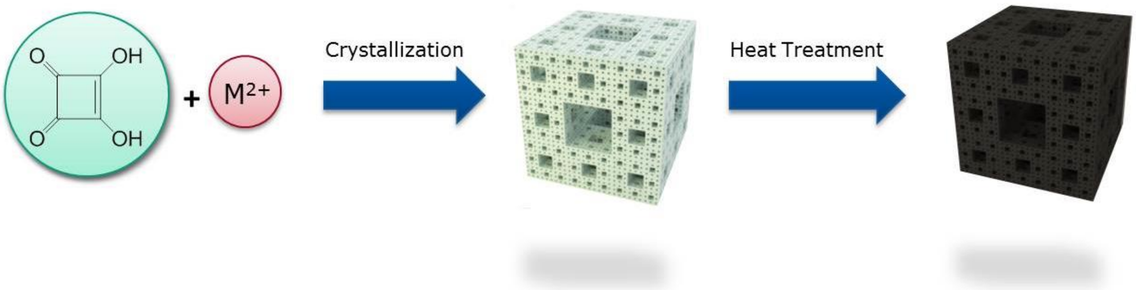

Figure 1.2 Schematic representation of the synthesis concept developed in this thesis. Reproduced from Mani *et al.* with the permission from Wiley.[47]

The controlled design of the material properties requires fundamental understanding of both the coordination chemistry of the respective system and of the impact of different synthesis parameters on the crystal formation and growth mechanisms which may influence the properties of the resulting carbonaceous materials. The squarate and the croconate ions belong to the family of the aromatic "oxocarbons anions" and as such exhibit several intriguing electronic and spectroscopic properties. For instance, they possess several donor and acceptor sites, which is why they can undergo a variety of unusual coordination modes.[48-51] Owing to these features, these molecules represent promising building blocks for the construction and design of 1D-, 2D-, and 3D- coordination structures. Although the coordination chemistry of the oxocarbon anions is well elaborated in numerous structural and spectroscopic studies, the crystalline materials resulting from their coordination complexes have not been employed so far as precursor material to synthesize functional porous carbon materials. Using highly stable coordination complexes as carbon precursor allows circumventing the aforementioned "black box" issue by maintaining control over the materials features at all preparation stages. A further benefit of this approach is that it does not require classical hard or soft templates to direct the pore structure of the resulting carbons. This makes this approach more cost-effective and less time-consuming than the conventional approaches.

In the following section (chapter 2), the theoretical fundamentals concerning the synthesis and applications of nanoporous carbon materials are introduced and discussed with emphasis on the molecular design strategy. Furthermore, the basic principles of the classical and non-classical crystallization theory, respectively, are reviewed and discussed.

In chapter 3, the synthesis of crystalline materials based on coordination complexes of the squarate with various divalent 3d block metal ions is reported along with the characterization of the structural and textural properties of the respective crystals and evaluation of the results. The impact of various synthesis parameters including aging temperature, ligand/metal molar ratio, solvent and the organic ligand system are presented and discussed.

Chapter 4 is mainly concerned with the synthesis of nanoporous composites and carbons by using mesocrystals with pre-defined structural information as precursor in order to tailor and adjust the properties of the resulting carbonaceous materials.

Chapter 5 focusses on different concepts to employ the prepared composite and carbon materials in different application. On the one hand, they are tested as electrode material for electric double-layer capacitor (EDLC), on the other hand they serve as support material to immobilize metal nanoparticles. The resulting composite is then employed as catalyst in a catalysis reaction.

2. Theoretical Fundamentals

2.1. Porous Carbon Materials

The concept of introducing pores into a solid's framework is acknowledged as a powerful tool to fabricate numerous kinds of materials with advanced properties.[52] Taking nature as inspiration, pores can be employed to store, separate and transport molecules, and to promote catalytically enhanced chemical reactions, among others. [53] In the process of biomineralization, for instance, nanopores can be useful for the construction of light-weight structures with high mechanical properties.[54] There is a large variety of materials with pores in the nanometer size regime including natural materials such as zeolites, biominerals, wood, and soil as well as synthetic porous materials such as porous silica, MOFs, and porous carbonaceous materials.

Porous carbon materials possess exceptional features such as a large surface area, high pore volume, high chemical stability as well as high electric and thermal conductivity.[14, 15] Up to date, they have been successfully established in a large range of applications including catalysis, gas storage and separation, and energy related applications.[55-57] Here, the performance of a carbon material in a specific application depends on several factors such as the chemical composition of the material and the textural and structural properties, among others. Hence, to produce high-performance carbon materials, it is important to have control over the material's characteristics.[7] This requires a fundamental understanding of the phenomena that govern at the nanoscale along with the processing effects which involve the careful selection of the carbon precursor, the carbonization process, and concepts of structuring the porous carbon.

Carbon precursors can be converted into nanostructured carbons by several methods including the classical carbonization process and the HTC approach, inter alia. The latter commonly involves the decomposition and conversion of carbohydrates to structured carbons in water at elevated temperatures (140-220 °C) in a closed autoclave system: This approach aims to mimick the natural coalification process on a timescale of hours and days, rather than millions of years.[58] HTC has the advantage that it requires fairly mild synthesis conditions and is considered to be quite insensitive to small deviations in concentration, temperature or reaction time.[59]

The classical carbonization process involves the heat treatment of the starting materials at elevated temperatures in the continuous flow of an inert gas. In the course of this process, the pyrolytic decomposition of the precursor materials goes along with the evolution of tarry and gaseous products resulting in a solid carbon mass with a rudimentary pore structure.[14] Here, the precursor material should preferably have a high density and low volatile content in order to achieve high carbonization yields along with the potential preservation of the precursor structures at the carbonization conditions. Some carbon precursors (e.g. coal pitch and petroleum pitch, inter alia) can form a liquid-crystalline phase during carbonization which favors a so called pre-orientation of graphite-like layers into groups of parallel layers. As crosslinking between the layers is weak, crystal growth is facilitated in terms of a regular rearrangement of the whole layer-planes or groups of layer-planes resulting in highly ordered graphitic structure upon high-temperature treatment.[60] These carbon materials are referred to as graphitizing carbons (**Figure** 2.1 **a**). [61, 62] In contrast, non-graphitizing carbon materials develop a strong system of crosslinking between the randomly oriented crystallites, hence yielding a rigid amorphous structure. Crystal growth in such systems and rearrangement of the layer-planes into regular orientated groups is hindered even after high temperature treatment (**Figure 2.1 b**).[63] However, as the resulting carbons possess specific surface areas of just few square meters per gram, further processing is necessary in order to generate well-developed and accessible pores and correspondingly large surface areas.

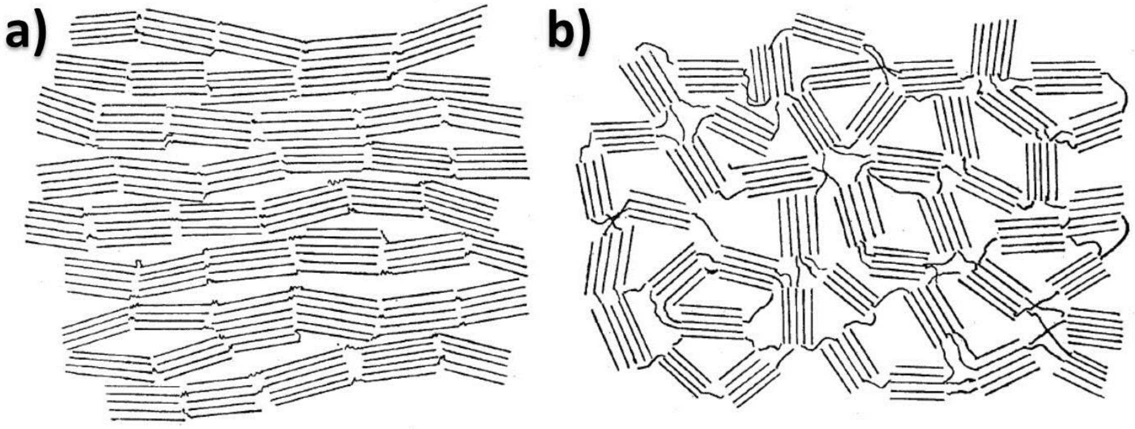

Figure 2.1 Schematic representations of the structure of a) graphitizing carbon and (b) non-graphitizing carbon. Adapted from Franklin *et al*.[61]

Generally, nanoporous materials are classified according to their pore diameters into three categories based on the International Union of Pure Applied Chemistry (IUPAC):[64] micro-, meso-, and macroporous materials (**Table 1**).

Table 1 Classification of porous materials according to IUPAC.

Type of porosity	Pore size [nm]
Microporous	< 2
Mesoporous	2-50
Macroporous	> 50

Each pore size regime offers certain benefits as well as limitations regarding the pore accessibility and diffusion mechanism of ions, molecules, and/or particles within the pores. For instance, microporous carbon materials typically possess high surface areas and low pore volumes. Furthermore, they exhibit superior adsorption abilities making them highly desirable for size- and shape-selective applications including gas storage and separation. However, a major drawback is the slow mass transport which arises due to space confinements as a result of the small pore sizes. In contrast, mesoporous carbon materials possess moderate surface areas but offer higher total pore volumes and well accessible pores, which provide an effective diffusion path for reaction substrates, among others. Macropores are defined as cavities that are larger than 50 nm in diameter but suffer from a low specific surface area. Macroporous carbons can be beneficial in several applications as photonic gap and dielectric materials but also as catalyst supports.[65-67]

Various approaches for the introduction of porosity into a solid structure have been reported recently. Here, the most common strategies include activation and template based methods.

The activation approach, which is mostly used to create micropores, basically involves the use of oxidizing substances in order to generate a well-developed pore structure along with a large internal surface area.[5] Two major types of activation techniques are generally distinguished, namely the chemical and the physical activation.[68] The chemical activation approach is a single-step reaction between the carbon precursor and an appropriate oxidizing agent at temperatures up to 1000 °C in an inert gas atmosphere. Classical chemical activating agents are phosphoric acid (H_3PO_4), sodium hydroxide (NaOH), hydrogen peroxide (H_2O_2), and potassium hydroxide (KOH), whereas the latter is considered to be the most effective and commonly used one.[69, 70]

In contrast, the physical activation approach proceeds in two successive steps. Here, the first step involves the carbonization of the precursor material along with the formation of a somewhat rudimentary pore structure that is partially blocked by tarry products. In the second step, the as-prepared carbon material is exposed to an oxidizing gas (e.g. CO_2 or H_2O steam) to enlarge and free the blocked pores, thus yielding a material with well accessible pores. Both activation methods have advantages and drawbacks: For instance, chemical activation is reported to produce higher carbon yields along with higher surface areas and a better developed pore structure allowing for operating at lower processing temperatures. However, it requires a final washing step to remove any residual chemical agents, which may cause water pollution. On the other hand, the physical activation approach is considered to be the more environment friendly and benign technique.

The templating based approach basically allows for the synthesis of carbonaceous materials with well-developed and uniform mesoporous structure via replication from a template material that already features a homogenous pore structure. Based on the nature of the template material, it is differentiated between the soft templating and the hard templating (nanocasting) approach. The former involves the use of organic amphiphilic molecules such as surfactants, polymers or biopolymers as structure-directing agents (SDA) which self-assemble into 2D- or 3D- structured supramolecular aggregates in interaction with an inorganic precursor material. An ordered porous structured material is consequently obtained after conversion of the organic-inorganic composite intermediate to the target material followed by template removal.[71] The hard templating approach is based on a porous and rigid inorganic framework, mostly produced via the soft templating route, as “hard template”.

The general synthetic procedure for the porous carbons synthesis via the templating based approach involves four major steps:

1) Synthesis of the porous template material
2) Infiltration of the porous template material with the precursor material
3) Conversion of the precursor to the carbonaceous material under the particular conditions
4) Removal of the template material yielding a uniform porous carbon material

In addition, the terms exo- and endo-templating are used depending on whether the desired product material is produced inside the template’s pores (exo) or formed around it (endo).

Despite the numerous advantages, the so far presented methods for preparation of both ordered and disordered porous carbon materials are still laborious as they involve several preparation steps and/or make use of hazardous chemicals for the removal of the inorganic template material. Therefore, these methods are not appropriate for large-scale production.

2.1.1. Hierarchical Porous Carbons

A hierarchical porous material is defined as a system of well-organized and interconnected pores of two (or more) different pore types, i.e. micro-, meso-, and macropores (**Figure 2.2**). According to the interplay between the different pore regimes, it can be distinguished between two types of hierarchy in porous materials, namely hierarchy-type I and II.[72] Type I hierarchy refers to materials in which a level of larger pores subdivides into the next level of smaller pores and so on. Type II involves a system of interconnected pores in which the smaller pores emerge from the larger ones. In comparison to classical porous materials, hierarchical porous materials have been shown to exhibit advanced properties in many applications including energy storage, photonics, water purification, and heterogeneous catalysis.[56, 73-76] The hierarchical structure combines the properties and advantages of the individual pore types, which it is comprised of, in one single material. In this context, macropores can serve as ion-buffering reservoirs that minimize the diffusion distance to the interior surfaces, whereas mesopores provide larger accessible surface area and lower ion-transport resistance. Micropores are associated with high surface areas and strong adsorption abilities combined with shape- and size-selectivity. Particular interest has been devoted to carbon materials which possess 3D ordered hierarchical pore structure as they exhibit high specific surface areas combined with well-accessible pore sites and short diffusion paths that can facilitate ion transportation within the nanopores.[76]

For the synthesis of hierarchically porous carbon materials, a multi-step approach is mostly applied combining the individual methods for pore structure generation including activation and templating techniques in an appropriate manner.[13, 77] For instance, Zhao and co-workers synthesized a hierarchical porous carbon consisting of ordered macro- and mesopores by using a two-step templating approach involving silica-based hard templating in the first step and a triblock copolymer F127 as soft template in the second step.[78]

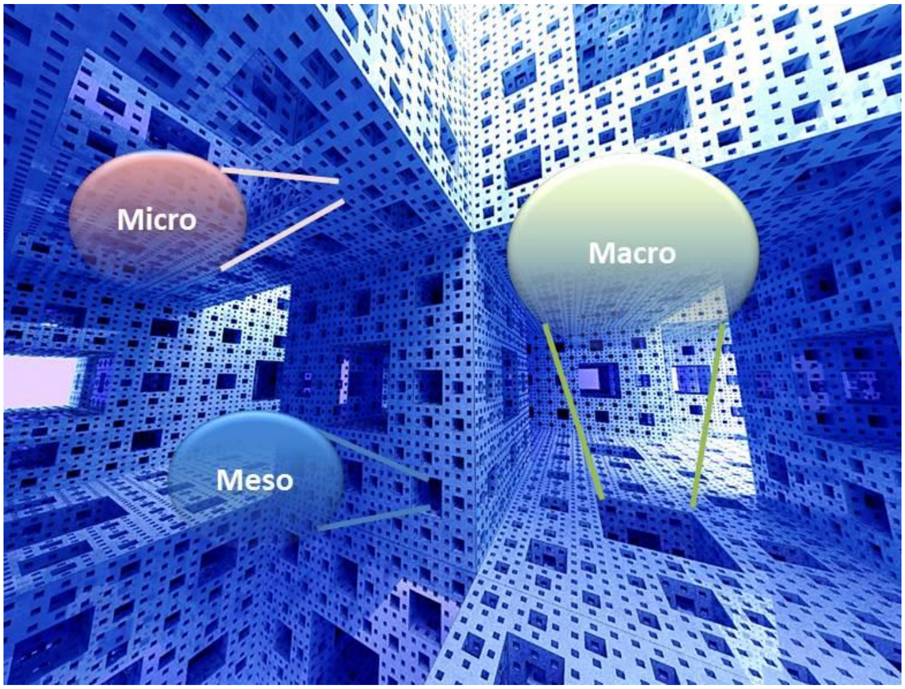

Figure 2.2 Schematic illustration of a hierarchical pore structure consisting of interconnected micro-, meso- and macropores. Reproduced from Mani *et al.* with the permission from Wiley.[47]

Antonietti and co-workers prepared hierarchically structured carbon aerogels with well-developed micro- and mesopores structure via hydrothermal carbonization using glucose as the carbon precursor and sodium borate as SDA.[24] In another work, Lu and co-workers reported on the preparation of hierarchically porous carbons via post-activation of a premanufactured soft-templated phenolic resin.[79] However, these approaches require several processing steps i.e. synthesis of the template material, impregnation of the precursor material followed by its conversion to the carbon product, and removal of the templating material. Furthermore, hazardous and toxic chemicals are used for template removal as well as in the activation process making these methods in general expensive, time consuming, environmentally unfriendly, and therefore not appropriate for large-scale production. New emerging strategies in the synthesis of hierarchically ordered porous carbons involve the use of MOFs in a template-free approach.

2.1.2. MOF-derived porous carbon materials

MOFs represent a class of crystalline materials which are constituted of multidentate organic ligands coordinated to transition-metal cations and hence extend to 3D assemblies.[80-82] The resulting structures exhibit a rigid and microporous framework associated with very high surface areas and large pore volumes. Because of these properties, they have been widely applied for gas separation and storage as well as heterogeneous catalysis and sensing applications.[83-86] In general, coordination compounds offer the benefit that features such as morphology, functionality, and surface area can be easily tailored by the appropriate combination of metal ion and organic linker.[87] Through the wide choice of possible metal ions and organic ligands, including polytopic pyridine-like and carboxylate-based ligands, a wide spectrum of structural, magnetic, electrical, and optical properties can be targeted.[82,83]

Because of their rigid framework and high carbon content, MOFs can be used as both a self-sacrificial rigid template material and a carbon precursor itself without the need of additional precursors. In 2008, Xu and co-workers first employed MOFs as template in the preparation of nanoporous carbons by impregnating the pores of the MOF with another carbon precursor such as furfuryl alcohol.[88] Heat treatment to 800 °C in an inert atmosphere yielded a nanoporous carbon containing both micro- and mesopores with a high surface area of 1732 $m^2 g^{-1}$, whereby the MOF template decomposed around 500 °C. In 2012, several groups reported simultaneously on the direct carbonization of MOFs to synthesize nanoporous carbons with high surface areas. For instance, Yang *et al.* used isoreticular MOF-1 (IRMOF-1) to synthesize a porous carbon (denoted MDC-1) which exhibited a hierarchical porous structure consisting of ultramicro-, micro-, meso-, and macropores with high surface areas (up to 3174 $m^2 g^{-1}$): These materials showed good and reversible H_2 storage capacities.[89] Yamauchi and co-workers used the commercially available ZIF-8 in the preparation of nanoporous carbons. ZIF-8 possesses a sodalite network which is constituted of coordinated zinc ions and methylimidazole.[40] Direct carbonization of this irregular shaped precursor at 1000 °C yielded an amorphous microporous carbon with a BET surface area of 1110 $m^2 g^{-1}$. In contrast, nanoporous carbons obtained via direct carbonization of the cobalt-based ZIF-67 led to a highly graphitized carbon framework owing to the catalytic effect of the cobalt nanoparticles.[90] Consequently, corresponding nanoporous carbons showed higher conductivity and improved capacitance retention. Additionally, the polyhedral morphology of the initial MOF is retained throughout the carbonization procedure.

By the use of 3D-structured MOFs as precursor, nanoporous carbons with high surface areas and large pore volumes can be easily prepared in a simple one-step synthesis approach. Furthermore, this approach allows for the control over the textural and structural properties of the final carbon materials by pre-defining the features of the crystalline precursors. In this context, crystal engineering represents a powerful and important tool as it provides a deeper understanding of the structure-property relationship of materials and thus empowers to control the material features in a more effective and rational manner.

2.2. **Crystal Engineering**

The rational design of crystalline materials with advanced properties is an important and constantly growing field of research.[91] Recent progress in this field has brought up a variety of novel materials with a large spectrum of physical and chemical properties which proved to be useful in a range of applications.[35, 92] Here, crystal engineering represents a promising and powerful concept which allows to predict the structures of the crystals based on the intermolecular interactions (e.g. covalent bonds, coordination bonds, van der Waals interactions, and hydrogen bonds, amongst others) between the building units. Furthermore, it aims to understand the relationship between the crystal structures and the properties of the materials well knowing that the material properties are often determined by the way in which their constituent building blocks are arranged.[36] Bottom-up strategies that start from building blocks such as atoms, ions, or molecules to produce single crystals or highly ordered superstructures are nowadays very common. They provide the ability to manipulate the morphology, particle size, and particle size distribution as well as porosity and thus the properties of the resulting crystalline materials.[93] Thereby, a fundamental understanding of the various crystal growth processes is indispensable for designing new materials with advanced properties as well as improving current systems.

In general, crystallization is a complex process, which basically involves two major steps, namely the nucleation of small crystals in solution and their subsequent growth into single crystals. According to the classical crystallization theory, nucleation takes place as the system becomes supersaturated with the solute molecules.[94] The as-formed crystals grow subsequently via attachment of the building units (e.g. atoms, molecules, or ions) in the solution yielding single crystals whereof the morphologies are determined by the intrinsic crystal structure.[95] However, the classical crystallization route often fails in explaining complex processes such as biomineralization, which lead to the formation of very complex morphologies with hierarchical order and superior materials properties.[96-98] An alternative crystallization pathway was recently proposed by Cölfen and Antonietti, who suggested that crystal growth during biomineralization involves the arrangement of nanoparticles into highly ordered and aligned structures via a mesoscale transformation.[96, 98] The resulting mesocrystals can further be transformed to single crystals upon crystallographic fusion of their constituting nanoparticles.[99] This concept is known as the non-classical crystallization and is depicted schematically along with the classical crystallization in **Figure 2.3**.

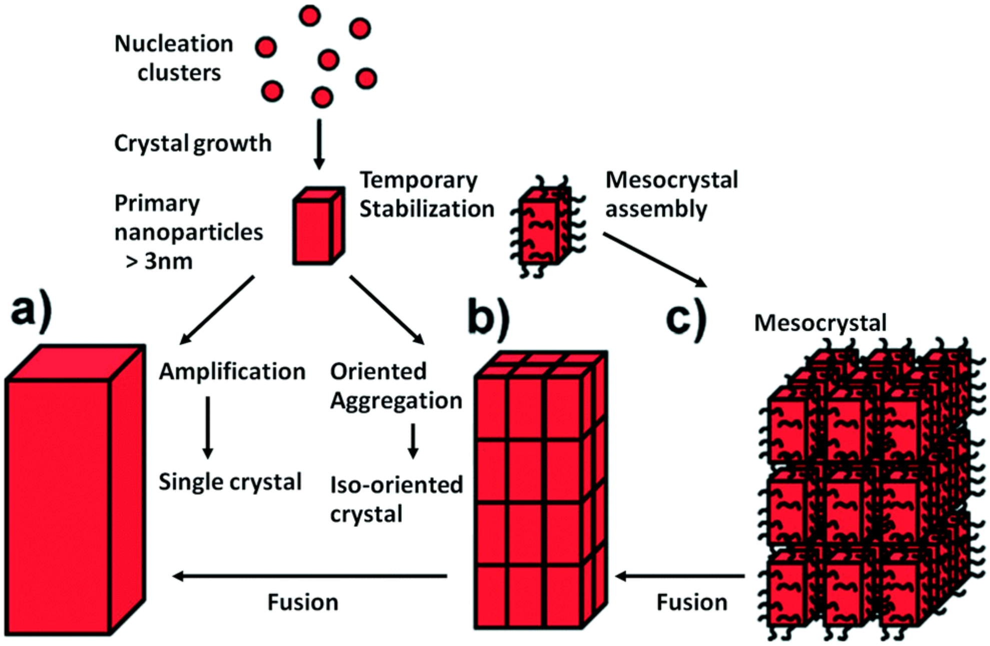

Figure 2.3 Schematic representation of the classical and non-classical crystallization models. a) Classical crystallization mechanism, b) oriented attachment and fusion of primary nanoparticles into iso-oriented crystals, c) mesocrystal formation via mesoscale assembly and fusion of the nanoparticles. Adapted from Niederberger and Cölfen.[100]

2.2.1. Classical Crystallization

The classical crystallization theory is useful to explain the crystallization process of single elements such as metals as well as the crystallization of covalent and ionic crystals in solution.[101] While the former assumes that liquid and crystalline phase have the same chemical composition, the latter is considered to be more complicated as it involves different chemical compositions and, therefore, a chemical potential between the two phases. The main principle underlying the classical crystallization is the attachment of building blocks such as atoms, ions, or molecules via a precipitation reaction on the surface of a stable nucleus to form a single crystal. Here, the thermodynamic driving force is the solvent supersaturation, which is expressed by the following equation:[102]

$$\mathbf{S = \frac{a}{K_{sp}}} \tag{2.1}$$

where S is the relative supersaturation, a is the concentration of the solute molecules in solution, and K_{sp} is the equilibrium solubility product. Generally, it can be distinguished between three different nucleation processes for the formation of crystals: homogenous, heterogeneous and secondary nucleation.[103] However, for the sake of simplicity, only the homogeneous nucleation process will be introduced in the following.

From a thermodynamic point of view, nucleation can be described as the process of forming stable crystal nuclei inside a large volume of a metastable solution phase. This implies that the overall free energy (ΔG) during nucleation is equal to the sum of the free energy related to the formation of the solute crystals (ΔG_S) and the free energy of new volume (ΔG_V). This relationship is given by the following equation:[94, 101]

$$\boldsymbol{\Delta G = \Delta G_S + \Delta G_V = -\frac{4}{3}\pi r^3 \rho_s T \Delta\mu + 4\pi r^2 \sigma} \tag{2.2}$$

where σ is the interfacial tension, ρ_s is the density of the solid material, r is the radius of the nucleus, and μ is the chemical potential. **Figure 2.4 a** shows the Gibbs free energy profile in dependence of the crystal size. According to that, nuclei below the critical size (r_c) are unstable and tend to dissolve rather than grow. However, when the nuclei size exceeds the critical size (r_c)

they will form stable entities as they can overcome the activation energy barrier. Here, the rate of nucleation strongly depends on the solution concentration, as with higher concentrations the activation energy and the critical size decrease. Moreover, nucleation can be controlled by varying parameters such as temperature, pressure, and pH, respectively, as they might reduce the solubility and increase the degree of supersaturation, respectively.[104] In general, nucleation cannot occur in solutions with concentrations below a certain solubility limit (C_s) (**Figure 2.4 b**). Over this point, the system becomes metastable and some nuclei are formed spontaneously. However, as the driving force for nucleation is still low at this point, some nuclei will dissolve again. When the concentration exceeds C_{min}, the system becomes supersaturated allowing for the rapid and spontaneous nucleation of small crystals whereas the concentration of the solute decreases. When the concentration falls below C_{min}, the nucleation of new crystals stops and only crystal growth takes place.[91]

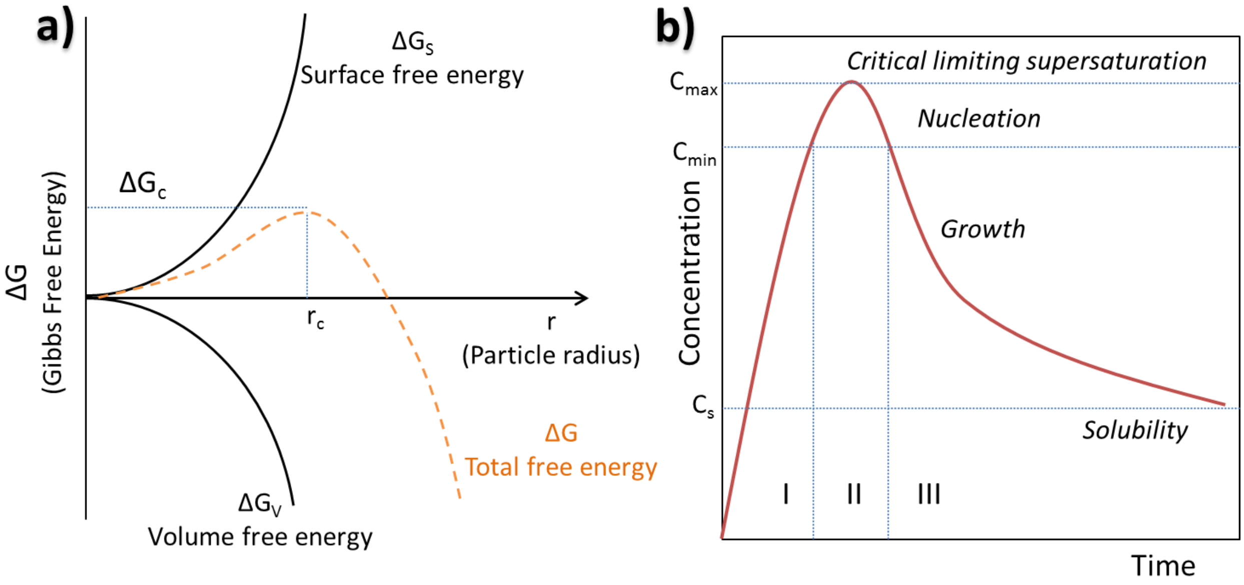

Figure 2.4 Schematic illustration of a) the nucleation and growth process showing the Gibbs free energy (ΔG) as a function of the particle radius, b) LaMer model used to describe nucleation and nucleus growth.

According to LaMer's model (**Figure 2.4 b**), monodisperse particles can be obtained when the nucleation and growth processes proceed successively.[105] Therefore, the nucleation process should preferably proceed at very high rates allowing for the rapid formation of a large number of nuclei in a short period. These initial nuclei can subsequently grow quickly, whereby the concentration decreases below the supersaturation level (C_{min}). This leads to a slower continuing growth of the crystals making the growth period longer compared to the nucleation period.[37] In contrast to that, polydisperse particles with a broad size distribution are obtained when the nucleation and growth periods overlap. As with progressing crystal growth, ions or molecules are consumed from the bulk solution and attach onto the crystal's surface, the degree of supersaturation in solution decreases. As a consequence, the critical size for spontaneous nucleus formation is shifted towards larger sizes whereby the crystal particles, that were considered to be stable, move into the unstable regime and dissolve again. In the course of the reaction, larger particles are grown at the expense of the smaller ones. This process is widely known as Ostwald ripening.[37, 91]

The resulting single crystals often exhibit intriguing polyhedron morphologies with smooth surfaces, whereby the final morphology is largely determined by the relative growth rates of the different crystal faces. A crystal face, in turn, is predominantly determined by the internal arrangement of the atoms in the crystal structure and develops along the lattice planes. Here, the driving force for the development of the faces is the reduction of the surface energy, i.e. faces with a high surface energy grow faster and diminish at some point.[95]

2.2.2. Non-Classical Crystallization

The non-classical crystallization concept has significantly contributed to the understanding of the crystallization mechanism in biological systems e.g. the bio-mineralization of intriguing structures which possess amazingly complex morphologies but at the same time behave like single crystals.[98, 106] Recently, Cölfen and Antonietti proposed a mesoscale transformation process towards single-crystalline structures over mesocrystal intermediates as a possible pathway for biomineralization.[96] In contrast to the classical crystallization route, the non-classical crystallization pathway does not proceed through successive attachment of ions, molecules, or atoms, but proceeds through the arrangement and mesoscale transformation of primary nanoparticle building blocks into single-crystalline 1D-, 2D-, or 3D- superstructures. Here, the library of possible building blocks that can self-assemble into mesocrystals is quite large including crystalline nanoparticles as well as amorphous and liquid precursors.[107-110] Compared to the classical crystallization, the non-classical crystallization offers the benefit that it is more independent of ion products or molecular solubility and proceeds without changes in pH or osmotic pressure while allowing for the synthesis of highly complex material morphologies.[99, 100]

As shown in the schematic illustration of this model in **Figure 2.3**, the non-classical crystallization can generally proceed via different pathways, including:

- The formation of primary nanoparticle building blocks.
- Arrangement of the primary building blocks into iso-oriented crystals via the oriented attachment pathway.
- Mesoscale assembly of organic-inorganic nanoparticles into mesocrystals.

2.2.2.1. Oriented attachment

The oriented attachment process was named and first reported by Penn and Banfield in the late 1990's, who upon studies on the hydrothermal coarsening of nanocrystalline titania (anatase) observed an exceptional crystal growth behavior which could not be explained by the classical Ostwald ripening.[111-113] Nowadays, the oriented attachment mechanism represents a very important crystallization pathway that allows for the formation of unique crystal morphologies and nano-architectures. In basic terms, oriented attachment involves the mutual crystallographic arrangement of nanosized building blocks into so-called iso-oriented crystals that can form single crystals upon crystallographic fusion. The driving force for this mutual crystallographic orientation, which determines the shape and size of the resulting single crystals, is the systems tendency to minimize the surface energy that can be achieved by fusion of the faces with the highest surface energy.[102] Basically, it can be distinguished between two different pathways for the oriented attachment of nanoparticles, namely: a) fusion of neighboring nanoparticles after their effective collision, b) coalescence of misaligned nanoparticles in contact after their rotation toward low-energy configuration.[101, 114]

The first mechanism occurs predominantly in a dispersed colloidal state, in which the growth rate via oriented attachment mainly relates to the collision rate among the nanoparticles. Here, the collision of nanoparticles with the same crystallographic orientation, which is called effective collision, is supposed to result in an irreversible attachment of these nanoparticles.[114] Collisions between nanoparticles with different crystallographic orientations or where coalescence is not possible are called non-effective collisions. The second possible mechanism for oriented attachment is mostly observed in weakly flocculated colloidal states.[101] Here, the oriented attachment process is not controlled by collisions, but rather determined by interactions between particles in the medium- and short-range, where the attractive forces such as van der Waals forces are higher than the repulsive forces (e.g. electrostatic interactions and steric hindering). Furthermore, the rotational freedom between the nanoparticles needs to be taken in account, as it is important to achieve high crystallographic alignment in the single crystal.[102]

In fact, the oriented attachment mechanism allows for the synthesis of superstructures of different dimensionalities via the arrangement of the single nanoparticles in a hierarchical manner. Thus, also mesocrystals with intriguing morphologies can be obtained, whereby the exposed faces are not controlled thermodynamically but rather kinetically.

2.2.2.2. Mesocrystal formation

Mesocrystals (mesoscopically-structured crystals) are defined as ordered superstructures composed of individual crystals of mesoscopic sizes, i.e. 1-1000 nm.[99] These nanocrystals are aligned in a perfect 3D mutual arrangement resulting in an inner crystalline structure that exhibits scattering properties and behavior in polarized light identical to a single crystal. In their pioneering work on bioinspired crystallization, Cölfen and Antonietti have proposed several non-classical crystallization pathways that can lead to mesocrystal formation.[96, 98] This includes the oriented attachment of nanoparticles, crystallization of amorphous or liquid precursors, and the mesoscale assembly of nanocrystalline building units. Mesocrystals are considered to be metastable as they can be easily transformed to single crystals via the oriented attachment process which includes the fast crystallographic fusion of their nanocrystalline building units. This is particularly observed in systems which exhibit high surface energies and thus provide a high driving force for the oriented attachment of the nanocrystals and their subsequent fusion. Therefore, it is often difficult to identify mesocrystals as they exhibit equal scattering and light polarization properties to single crystals, which can lead to misinterpretation.[115] However, mesocrystals can be stabilized by coating the nanoparticles with organic additives or by introducing charge on the nanoparticle surfaces. In this case, mesocrystal formation is proposed to occur via the mesoscale assembly pathway.

The mesocrystal concept has evolved to a very effective tool for the rational synthesis of crystalline materials with complex and fascinating morphologies and functions. New material properties are expected to result from the synergistic combination of the properties of the individual building units showing potential in many applications, for example for optical and electronic devices.[115]

However, the particular growth mechanism for the formation of the diverse kinds of mesocrystals has not been fully understood yet and is still a matter of current intense research.[116] Various mechanisms for the mutual 3D nanoparticle alignment have been proposed recently in literature, whereby the most discussed ones are the following:[99, 102, 115]

- Nanoparticle ordering by physical fields such as electric, magnetic or dipole fields.
- Epitaxial growth involving mineral bridges which connect the nanoparticles.
- Entropy-driven nanoparticle alignment by spatial constrains.

3. Crystalline superstructures of oxocarbon-based coordination complexes

3.1. Background and State-of-the-Art

Oxocarbons represent a class of organic carbocyclic compounds containing one or more oxo-groups. Since the pioneering work of Robert West in 1963, oxocarbon anions of the general formula $(C_nO_n)^{2-}$ have gained immense interest owing to their aromatic nature, stabilized by the strong delocalization of π-electrons in the ring.[117-119] This provides the possibility of π-stacking interactions between the rings as well as of transmission of electronic effects between the paramagnetic centers.[120] Furthermore, the oxocarbon anions display good donor ability as they possess several electron donating O-atoms that can be beneficial in the construction of coordination complexes in their interactions with metal ions. The respective crystal lattices are then stabilized by strong H-bonds and by π-π interactions between adjacent layers giving rise to extended supramolecular 3D structures.[121] Among the different oxocarbon anions, the most popular examples include the deltate (n=3), squarate (n=4), croconate (n=5) and rhodizonate (n=6).[117, 119, 122-124]

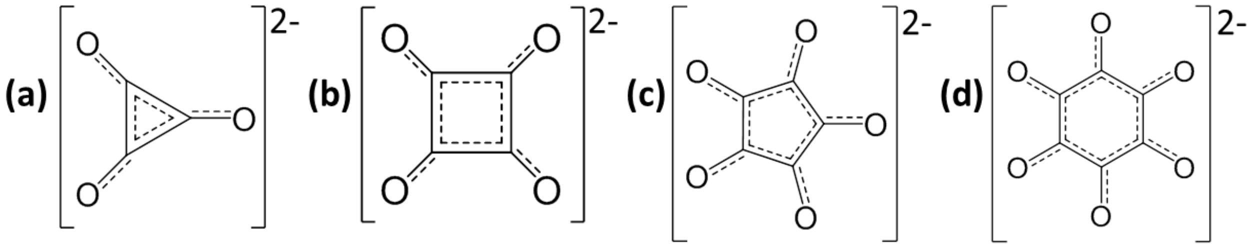

Figure 3.1 Aromatic series of the oxocarbon anions family stabilized by symmetrical resonance (Hückel's rule for planar monocyclic systems): a) deltate, (b) squarate, (c) croconate, (d) rhodizonate.

The structural and electronic properties of the oxocarbons dianions have been subject of intense discussions with controversial conclusions on the aromaticity and electronic structure of these species.[122, 125-127] For instance, West *et al.*[122] argued on the basis of the planarity and cyclic conjugation of the oxocarbon dianions in consistence with large π-electron delocalization energies as evidence for their aromatic nature. It was further observed that the electron delocalization energies decreased significantly with the ring size. On the other hand, Schleyer *et al.* concluded based on the nucleus-independent chemical shift (NICS) concept that only the deltate and squarate species are aromatic, whereby the degree of aromaticity decreases with the increasing ring size. [128]

Generally, in their neutral forms oxocarbons represent strong dibasic acids and possess high dissociation constants (pK_1=0.8-4.3 and pK_2=2.2-6), whereby the pK values depend on the ring size.[121] In this context, squaric acid (pK_1=1.5 and pK_2=3.4) is considered to be less acidic than deltic acid (pK_1=2.57 and pK_2=6.03), but a stronger acid than croconic acid (pK_1=0.8 and pK_2=2.24).[121] These high acidities can be attributed to the strong resonance stabilization of the resulting monoanion $[C_4O_4]^-$ and dianion $[C_4O_4]^{2-}$, respectively, [121, 129] whereby the latter is formed more predominantly in aqueous solutions.

In the recent years, a lot of research has been conducted with regard to the coordination chemistry of different oxocarbon ions in complexes with various metal ions.[121, 130] However, among these studies, a big majority focused on the metal-complexes that are based on the squarate and croconate as organic ligands, respectively.[50, 131, 132] Unlike its neutral form, the squarate is completely symmetrical as all C-C and C-O bond lengths are equal due to the redistribution of the electron density over the ring.[124] Given the strong donor and acceptor abilities of the squarate, it represents a versatile ligand allowing for a variety of coordination modes in complexes with divalent d-block metal ions. As was shown in several studies, these complexes can exhibit bridging μ-1,2 and μ-1,3 bis-, tris- and tetrakis (monodentate), as well as bidentate, or bis-bidentate coordination modes, respectively.[121, 133, 134] Thereby, in complexes with 3d block metal ions the bridging bis-monodentate (μ-1,2 or μ-1,3) coordination mode is observed predominantly. This can be attributed to the large bite angle of the squarate anion with the d-block metal ions.[135] However, chelating and bis-chelating coordination modes can be observed in complexes of squarate with alkaline- and alkali-earth cations as a result of the lower bite angles.[50, 51] Depending on the synthesis conditions, many of these coordination complexes can exhibit 3D architectures which are additionally stabilized by intermolecular π-π interactions and by strong hydrogen-bonds between the squarate and coordinated water molecules.[136, 137]

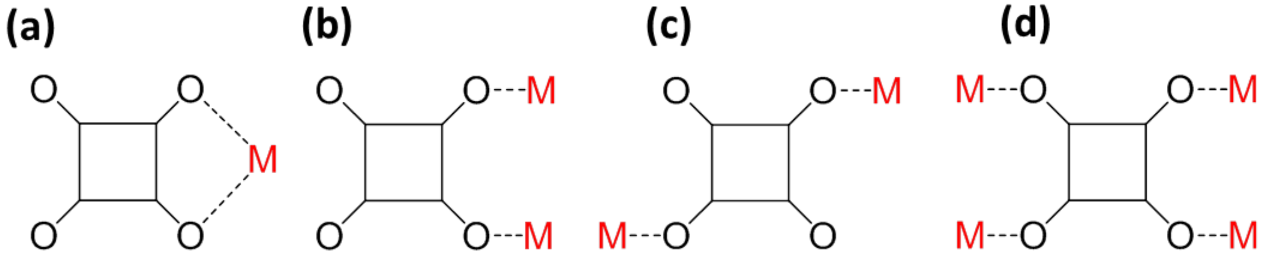

Figure 3.2 Schematic representation of the various possible coordination modes of squarate metal complexes. a) μ-1,2-bidentate chelating, (b) μ-1,2-bis(monodentate), (c) μ-1,3-bis(monodentate), and (d) tetrakis(monodentate).

Intriguing crystal structures have also been reported by using the croconate anion as ligand for the synthesis of metal coordination complexes. Owing to the fact that it possesses five keto groups, it can adapt more coordination motifs compared to the squarate. Up to date, 15 different coordination modes of the croconate have been reported, as recently reviewed by Artizzu *et al*.[138] This includes the monodentate, bidentate, and several other bis(bidentate chelating and bridging, respectively) coordination modes. For instance, the croconate yields coordination complexes of the general formula $M(C_5O_5)$ in reaction with the divalent ions of the d-block metals such as Zn^{2+}, Cu^{2+}, Ni^{2+}, Co^{2+}, Mn^{2+}, and Fe^{2+}, respectively.[119, 139] These compounds were reported to be isomorph, i.e. they all possessed a orthorhombic crystal structure, whereby each metal ion is coordinated by three croconate units and to one water molecule.[140]

The recent years have witnessed an exponential increase regarding the study of coordination compounds, particularly of those with a porous structure. This led to the development of more than 20,000 new functional crystalline materials within the past view years, showing excellent performances in a wide spectrum of applications. This includes gas storage and separation, drug delivery, photoluminescence, and catalysis, among others.[141-143] Crystalline materials composed of an organic ligand system coordinated to a metal ion are attractive from the viewpoint of crystal engineering. The variable selection of organic ligands and metal ions allows for a high number of possible combinations leading to a wide range of materials with intriguing physical and functional properties. However, it is to be noted that the relative amount of studies reporting on the crystal growth mechanisms and kinetics of the formation of coordination compound superstructures, particularly of those based on oxocarbon-metal complexes, is scarce compared to the work related to their applications. This leads to a lack of understanding, which is actually necessary for the development of rational concepts that allow controlling properties of crystalline materials such as particle size, morphology and particle size distribution.

In general, the classic crystallization theory describes the crystallization process starting from a supersaturation induced nucleation step. This leads to the formation of stable nanocrystals which further grow by unit-cell replication through successive attachment of the building blocks (atoms, ions, molecules, and small clusters) on the nuclei surfaces.[91] The final product is a single crystal with a characteristic morphology that is related to the intrinsic unit cell structure and defined by the faces with the lowest surface energy (Wulff's rule).[91] However, many intriguing structures with highly complex morphologies cannot be explained by the classical crystallization theory, but rather underlie a non-classical crystallization pathway as proposed by Cölfen and Antonietti.[99] The non-classical crystallization theory has significantly contributed to the understanding of the formation of single crystals in very complex systems, such as in biomineralization. According to that, single crystals and so-called mesocrystals can be generated by the arrangement of primary nanocrystals into highly ordered 1D-, 2D-, and 3D-superstructures via the oriented attachment mechanism.[100] Such synthetic hybrid materials with defined crystal faces, but derived from the perfect alignment of nanocrystals, have already been postulated for systems including calcium carbonate, copper oxalate, $BASO_4$, and $CoPt_3$.[144] Cölfen and Antonietti suggested that crystallization via mesocrystal formation may even represent a common phenomenon for the synthesis of single crystals.[96, 99] Recent studies have revealed that MOFs and other coordination compounds can crystallize via the oriented attachment and fusion of nanocrystals to form mesocrystals or superstructures.[145-147] For instance, Zheng *et al.* recently demonstrated that Prussian blue (PB) microcrystals could be generated via the mesoscale self-assembly of PB nanoparticles into mesocrystals under the hydrothermal conditions.[148]

The oxocarbon anions, in particular the squarate and the croconate, are characterized by strong donor and acceptor abilities making them a versatile ligand system for the rational design of stable coordination complexes.[120] Despite the numerous reports on their coordination behavior in complexes with various metal ions, the majority of these studies focused on the crystallographic and spectroscopic investigations of the crystal structure and electronic properties of these squarate-based compounds.[50, 131] To the best of our knowledge, the crystal growth mechanism of coordination complexes of the oxocarbon anions with divalent 3d block metal ions has not been investigated, yet.

In this chapter, concepts for the rational design of crystalline 3D superstructures will be elaborated using coordination compounds of squaric acid with various metal ions. The influence of various synthesis conditions such as temperature, metal-ligand ratio, solvent as well as the ligand choice on the crystal growth processes will be explored and shown to contribute to the morphology, habit, and shape of the resulting crystals.

3.2. **Characterization of the coordination compounds**

The structuration of coordination compound based nanocrystals into ordered crystalline 3D superstructures by using bottom-up strategies relies on the control over the nucleation and crystal growth processes. For the rational design of functional crystalline materials, it is important to understand how different synthesis parameters may affect the thermodynamics and kinetics of the crystallization process, which in turn define characteristics such as morphology, shape, and habit of the crystals.[149, 150]

Care must be taken with the terms morphology, shape, and habit that are necessary to describe the external form of a crystal. The term shape is generally used to describe the overall appearance of a crystal and includes, among others, cube, tetrahedron, octahedron, rhombohedron as well as their truncated forms.[91] The term morphology refers to the sum of faces and edges enclosing a crystal, whereby the crystal face is predominantly determined by the internal arrangement of atoms in a crystal structure.[91, 151] The crystal habit is defined by the relative dimensions of the faces of a crystal and is determined by the growth rates of the crystal in different directions.[152] The faster the crystal grows in a particular direction, the smaller the face extends perpendicular to that direction and vice versa. Depending on the growth rate of the respective faces in a certain direction, three types of habits are distinguished, namely equant, planar or tabular, and prismatic or acicular (needle-shaped).[152] As exemplarily shown in **Figure 3.3 a**, crystals can have identical morphologies but different habits as the relative dimensions of the crystals are different. However, it is also possible for two crystals to exhibit different morphologies with similar habits.

In general, a crystal face develops along lattice planes and the crystal edge is defined by a set of lattice lines i.e. the crystal face is more pronounced and developed the more lattice points it covers. Crystal faces are commonly described by using the Miller indices (hkl) as depicted in **Figure 3.3 b**. For instance, relating to a Cartesian coordinates system in three dimensions, the crystal face (100) refers to a set of crystal planes which intersect the a-axis and are parallel to the b and c-axis.

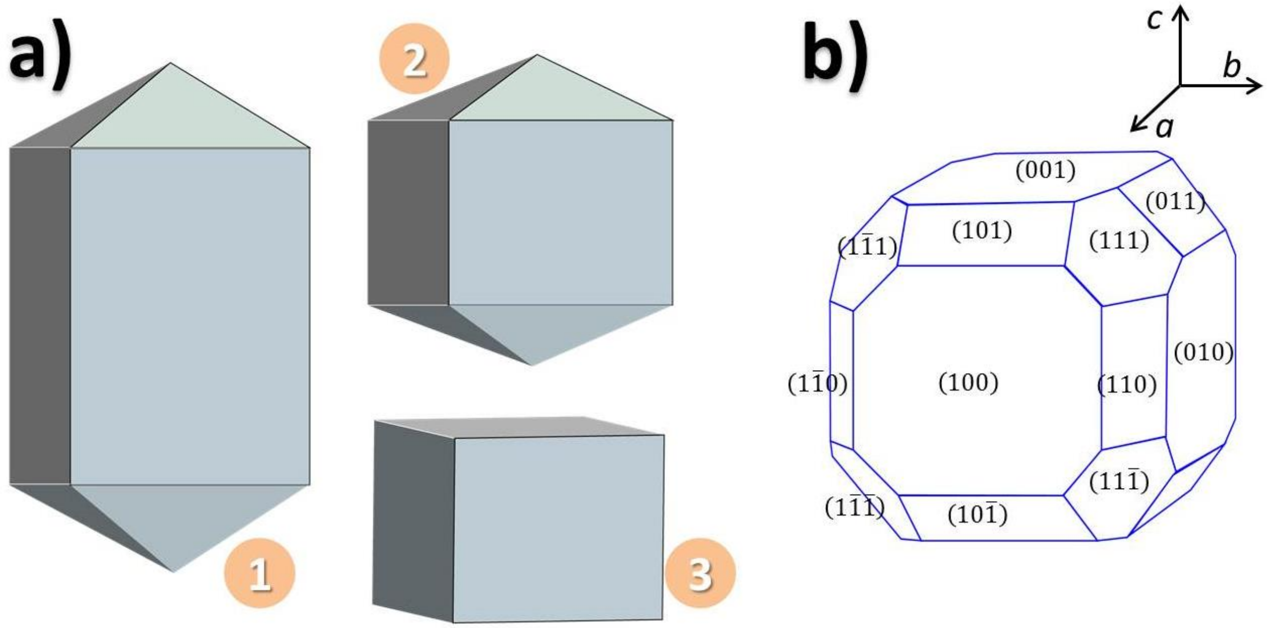

Figure 3.3 a) Schematic illustration of the relationship between crystal morphology and habit whereby the crystals 1 and 2 have the same morphology but different habits while crystals 2 and 3 exhibit different morphologies, but have similar habits. b) Crystal faces of a truncated cube with the corresponding Miller indices.

3.2.1. Squarate-Zinc coordination complexes

In the following, coordination complexes of the squarate with Zn^{2+} were chosen as starting compound. In general, Zn^{2+} has a filled d-shell (d^{10} electron configuration) and therefore possesses no Ligand Field Stabilization Energy (LFSE) and also no geometric preference in its coordination complexes.[153] Consequently, Zn^{2+} can adopt several coordination geometries, which are mainly determined by the radii of both the metal ion and the coordinating ligand atoms or ions. However, in aqueous solutions, the octahedral geometry is predominantly observed.[154] Herein, crystals were grown from squarate-zinc coordination complexes by using squaric acid (SA) and zinc acetate dihydrate (ZAD) as starting reagents. In a typical synthesis, aqueous solutions of SA and ZAD were mixed at the respective molar ratios at room temperature (RT). The resulting colorless crystals were then aged overnight at the respective temperatures, filtered, washed with water, and finally dried in vacuum at 60 °C overnight. Throughout this thesis, the resulting crystals are denoted as SAZn_R_T, where R refers to the molar ratio of SA/Zn and T refers to the aging temperature. The crystals precipitated very quickly and a colorless microcrystalline powder, insoluble in water, was obtained as the final product.[36] A striking odor typical of acetic acid was noticed during the synthesis procedure indicating that acetic acid was released as by-product. This hints to the fact that the squarate might coordinate to Zn^{2+} by substituting the acetate groups which consequently were released as acetic acid. In the following, the crystals prepared at a SA/Zn molar ratio of 1:1 and aged at 80 °C overnight (referred to as SAZn_1_80) were investigated with respect to their structural and textural properties. Optical microscope (OM) images of SAZn_1_80 (**Figure 3.4 b**) reveal monodisperse particles with a three-dimensional (3D) morphology. The crystalline nature of the complex is evident from the corresponding polarized optical microscope image showing strong birefringence which points to a high degree of ordering in the crystal. For the sake of comparison, the OM image of squaric acid recrystallized in water is illustrated in **Figure 3.4 (a)** showing particles with a truncated tetrahedral shape. This strongly suggests that the 3D cube shape observed for the crystalline SAZn_1_80 is mainly driven by the coordination of Zn ions to the squarate units. The corresponding scanning electron microscopy (SEM) images allow for a finer depiction of the crystal morphology. **Figure 3.4 (c, d)** reveals monodisperse particles with an average diameter of 24 µm and an intriguing truncated cube shape. Moreover, the particles exhibit unusual openings and voids (~3 µm in diameter) particularly centered on the low index faces $(100), (010), (\bar{1}00), (0\bar{1}0), (001)$, and $(00\bar{1})$. In spite of the numerous and extensive studies on the coordination chemistry of squaric acid in complexes with various divalent 3d block metal ions, this kind of morphology has not been reported yet for squarate-based metal complexes, to the best of our knowledge. The high-resolution SEM image of the cube (**Figure 3.4 e**) highlights the rough nature of the surface and reveals nanoparticles agglomerated in a characteristic manner whereby the resulting superstructure exhibits several voids and pores. According to the definition given by Cölfen and Antonietti, such 3D superstructures composed of nanocrystals which are arranged in a crystallographic manner are called mesocrystals.[96, 99, 100] Depending on the synthesis conditions, they can be formed via the mesoscale assembly of organic-inorganic nanoparticles or via the oriented attachment pathway. In order to gain more insights into the growth process, SEM images of the mesocrystalline SAZn_1_80 were recorded after a crystal aging period of only 1h at 80 °C. The corresponding SEM image (**Figure 3.4 f**) shows a cube shaped particle which measures approximately 20 µm in particle diameter and exhibits a rough surface. However, the previously mentioned openings at the centers of the low index faces cannot be observed at this crystal growth stage.

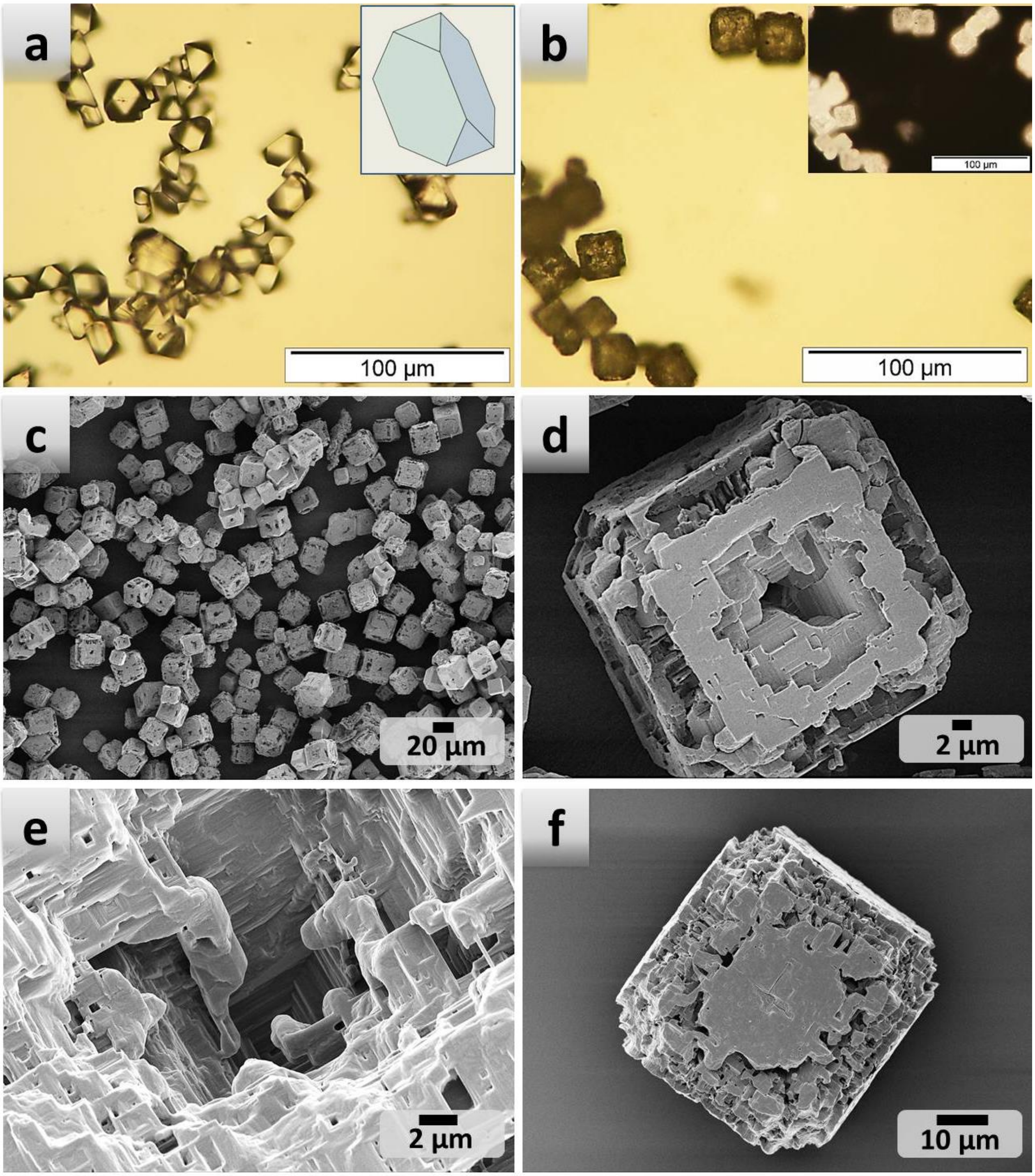

Figure 3.4 a) Optical microscope image of squaric acid recrystallized in water, b) Optical microscope image of SAZn_1_80 aged overnight, c-e) SEM micrographs of SAZn_1_80 aged overnight, f) SEM micrograph of SAZn_1_80 aged for 1h. The inset in (a) depicts a truncated tetrahedron for better comparison, the inset in (b) shows the polarized optical microscope image of SAZn_1_80 aged overnight.

Therefore, it is suggested that the formation of the striking openings on the face-centers is largely determined by the aging temperature and occurs at the later stages of the growth process. Reports on similar observations during the synthesis of crystals can be found in several literatures, in which the void formation inside the crystals is attributed to the Kirkendall effect.[155-157] This phenomenon basically refers to a non-equilibrium diffusion process at the interface between two components of a material with different diffusion rates.[158] Here, the unbalanced material flow is compensated by the formation of voids in solids. In solutions, the Kirkendall effect is sometimes accompanied by grain coarsening in a material at high temperatures.[159] According to several observations described in the literature, Zn containing materials are likely to show the Kirkendall effect leading to the outward diffusion of the Zn ions. More insights into the formation and evolution of the observed voids and openings can be obtained by preparing crystals and different aging temperatures. This will be discussed hereafter.

Analysis by X-ray diffraction (XRD) confirmed the crystalline nature of SAZn_1_80 (**Figure** 3.5 **a**).

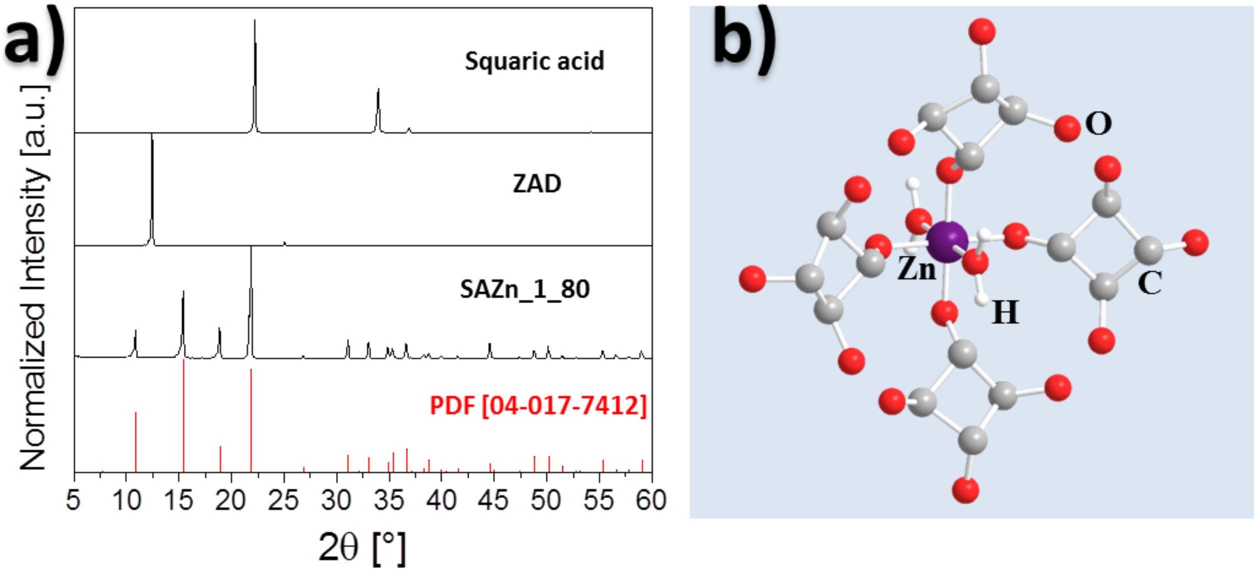

Figure 3.5 a) XRD diffractograms of squaric acid, zinc acetate dihydrate, the coordination complex SAZn_1_80 and the reference pattern PDF [04-017-7412]. b) Coordination environment in the coordination compound SAZn_1_80 (color code: Zn, purple; O, red; C, grey; H, white).

The corresponding diffraction pattern was compared to the crystallographic data collected from the International Centre for Diffraction Data (ICDD) revealing the following crystal composition $Zn(H_2O)_2\,(C_4O_4)$.[137] According to that, the Zn atoms are each coordinated by four squarate units and two water molecules in trans-position to each other forming a slightly distorted octahedron as depicted in (**Figure 3.5 b**). In this complex, the crystal lattice extends to a 3D network, which is probably stabilized by strong intermolecular hydrogen bonds between the squarate units and the crystallization water molecules.[137, 160] The resulting nanocrystals further arrange either via mesoscale assembly or via oriented attachment into the 3D cube mesocrystals.

Further structural characterization of SAZn_1_80 was made by Fourier transform infrared spectroscopy (FTIR) studies. The FTIR spectrum of SAZn_1_80 (**Figure 3.6,** blue line) reveals absorption bands characteristic of both squarate and zinc salt dihydrate units. For instance, an absorption band of medium intensity can be observed at 1761 cm^{-1} corresponding to the ν(C=O) stretching mode. In addition, a strong absorption band can be observed at 1496 cm^{-1} and assigned to the ν(C=C) + ν(C=O) stretching mode of the squarate unit. The absorption band at 1104 cm^{-1} is characteristic of the ν(C-C) mode. Compared to the FTIR spectrum of SA, the vibrational bands of SAZn_1_80 are shifted to lower wavenumbers and the band related to ν(C=C) at 1635 cm^{-1} in the spectrum of SA is not present in the spectrum of SAZn_1_80. These insights strongly suggest enhanced electronic delocalization and correspondingly increasing degrees of aromaticity in the crystal SAZn_1_80. This can be attributed to the fact that the squarate units are present in their dianion form $[C_4O_4]^{2-}$.[161] From the spectrum of ZAD, two bands stand out as they are not visible in the spectrum of SAZn_1_80, namely the symmetric and asymmetric absorption bands of the carboxyl groups of the acetate anion visible in the wavenumber region 1549-1436 cm^{-1} (**Figure** 3.6**,** red line). These bands are characteristic of the bidentate coordination of the acetate groups to the zinc ion.[162] The absence of these characteristic absorption bands in the FTIR spectrum of SAZn_1_80 in combination with the striking odor noticed during the synthesis strongly support the suggestion that the coordinated acetate groups are replaced by the squarate units and further released as by-product. The broad absorption band at 3227 cm^{-1} in the spectrum of SAZn_1_80 can be assigned to the ν(OH) stretching mode of water molecules coordinated to the zinc ion. However, it is striking that this band is shifted to higher wavenumbers compared to the corresponding ν(OH) band in the spectrum of ZAD (3070 cm^{-1}). This might be attributed to the fact that in ZAD hydrogen bonding is much stronger owing to the fact that the -OH groups can undergo intermolecular hydrogen bonding with the coordinated water molecules as well as with the carboxyl group of the acetate groups.[163] In general, these insights give a good picture of the structure of the complex SAZn_1_80 which is in good accordance to the XRD evaluation.

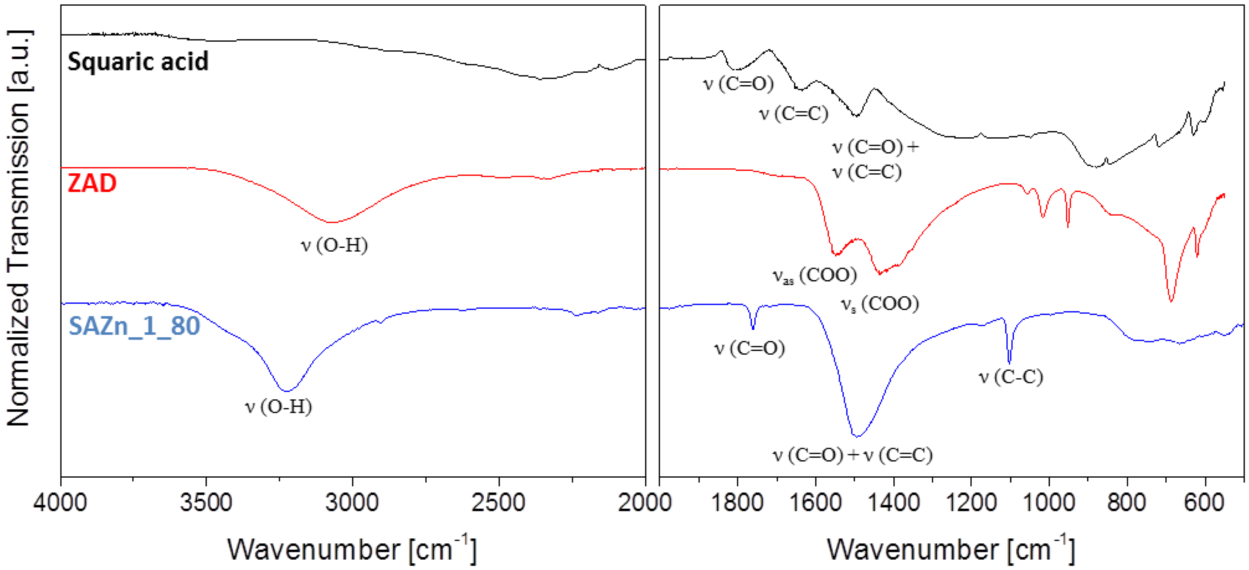

Figure 3.6 FTIR spectra of squaric acid (black line), zinc acetate dihydrate (red line) and the coordination compound SAZn_1_80 (blue line) showing characteristic symmetric and asymmetric absorption bands.

The evaluation of the SEM images (**Figure 3.4**) of SAZn_1_80 revealed the presence of nanopores and voids in the crystalline superstructure, which are suggested to be due to the particular arrangement of the cube nanocrystals at the given synthesis conditions. Nitrogen sorption measurements were performed in order to obtain more insights into the pore structure of the mesocrystalline material. The surface area, total pore volume, and pore size distribution were determined using the Brunauer-Emmet-Teller (BET) model and the nonlocal density functional theory (NLDFT) equilibrium model method for slit and cylindrical pores, respectively. The nitrogen sorption isotherm of the crystal SAZn_1_80 (**Figure 3.7 a)** exhibits combined characteristics of a type I and type IV isotherm with steep uptakes at a low relative pressures ($P/P_0 < 0.1$) as well as at a high relative pressures around $P/P_0 = 0.9$. The relative steep nitrogen uptake at low relative pressures can be attributed to the filling of micropores, whereby the subsequent two-step adsorption profile along with the hysteresis loop hints to capillary condensation in bimodal mesopores. The high nitrogen uptake around $P/P_0 = 0.9$ indicates the presence of macropores, which are not filled with the adsorbate at the atmospheric pressure. The two-step desorption profile is suggestive of both equilibrium evaporation and cavitation effects.[164] The first desorption step at higher relative pressures is associated with evaporation of the condensed phase from open pores (macropores), followed by the emptying of blocked mesopores via cavitation. Cavitation basically describes the spontaneous formation of gas bubbles in the metastable condensed phase. Moreover, it assumes bottle-ink type pores, where the pore neck width is much smaller than the pore body diameter. In this case, the pore neck remains filled while the pore body first empties during the desorption process.[64] According to Thommes *et al.*, cavitation controlled evaporation is typical for interconnected micro- and mesopores.[165] Based on the Kelvin equation, relative pressures less than 0.3 correspond to pore diameters smaller than 3 nm. Hence, the observed hysteresis closure at low relative pressures around P/P_0= 0.1 can be attributed to evaporation from pores widths smaller than 3 nm. The corresponding pore size distribution (PSD) reflects very well the suggestions made on the basis of the nitrogen sorption isotherm evaluation. In this context, Figure 3.7 b reveals a narrow bimodal mesopores distribution with peak maxima around 5.3 and 3.8 nm, respectively. Moreover, it shows a narrow peak in the micropores regime around 1.7 nm. Based on these results, it can be suggested that the mesocrystalline SAZn_1_80 possesses a hierarchical pore structure consistent of open macropores as well as interconnected micro- and mesopores, whereby the mesopores exhibit both open and partially narrowed or blocked pores.

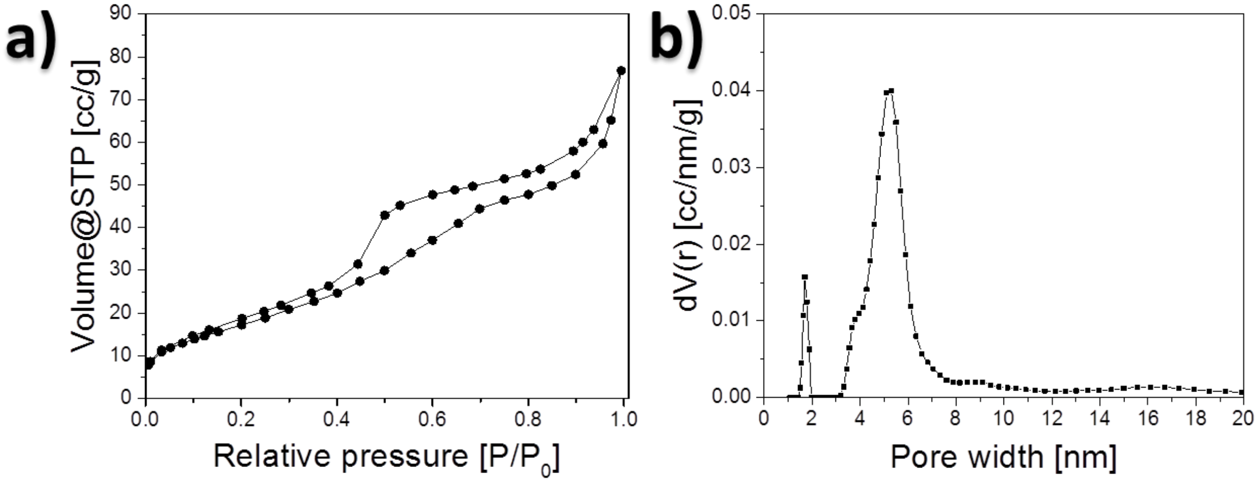

Figure 3.7 a) Nitrogen sorption isotherm of the coordination complex SAZn_1_80, b) corresponding PSD curve calculated based on the NLDFT model for slit and cylindrical pores.

3.2.1.1. Impact of the crystal aging temperature

In order to understand the influence of the temperature on the shape evolution of the mesocrystals, squarate-zinc-complex based mesocrystals were prepared at various aging temperatures ranging from 4 to 100 °C. From the corresponding OM and SEM images (**Figure** 3.8), it can be seen that the aging temperature significantly impacts the crystal appearance. The crystals aged at 4 °C, named SAZn_1_4, exhibit a cube shape with truncated edges and smooth surfaces, whereby no voids or openings can be observed. By increasing the aging temperature to RT and 80 °C, respectively, micrometer-sized openings become visible on the centers of the low index faces $(100), (010), (\bar{1}00), (0\bar{1}0), (001)$, and $(00\bar{1})$ and develop along with an increase of the surface roughness as the aging temperature is augmented. According to literature, such a shape evolution may be possibly explained by the Kirkendall effect which involves the outward diffusion of Zn ions along with the void formation.[166] In this case, the Zn ions diffuse to the outer surface of the crystals where they are exposed to solute molecules forming additional nanocrystals on the surfaces of the primary mesocrystals. This may explain the observed increase of the surface roughness, as with increasing aging temperature more Zn ions diffuse to the outer surface of the crystals and react with the solute molecules. However, the crystals aged at 100 °C (SAZn_1_100) exhibit a distinct particle shape, whereby **Figure 3.8 e** reveals that the mesocrystals are composed of individual nanocrystals which are arranged in a hierarchical manner. Along with the Kirkendall effect, which is likely to take place in Zn-containing crystals, the effect of the temperature on kinetics and thermodynamics of the crystallization process (i.e. interfacial energy, diffusion and growth rate coefficients as well as equilibrium solubility) also need to be considered.[104] For instance, the activation barrier for nucleation is decreased and allow for the formation of small crystals at higher temperatures.[91] Taking this into consideration, it is suggested that in the course of the aging process at 100 °C additional nanocrystals are formed and quickly attach onto the primary mesocrystals which exhibit the Kirkendall effect induced outer diffusion of the Zn ions. As the diffusion of the nanocrystals is high at such high temperatures, the collision rate between the nanocrystals and the primary mesocrystals is also high leading to structures which are not very highly ordered but porous. This suggestion is further supported by the XRD analysis (**Figure S 1**), which revealed similar diffraction patterns for the crystals aged from 4-80 °C hinting to the crystal composition $Zn(H_2O)_2(C_4O_4)$.[137] In addition to these characteristic reflection signals, the diffractogram of SAZn_1_100 reveals also other reflections which hint to the presence of nanocrystals with a distinct crystal structure.

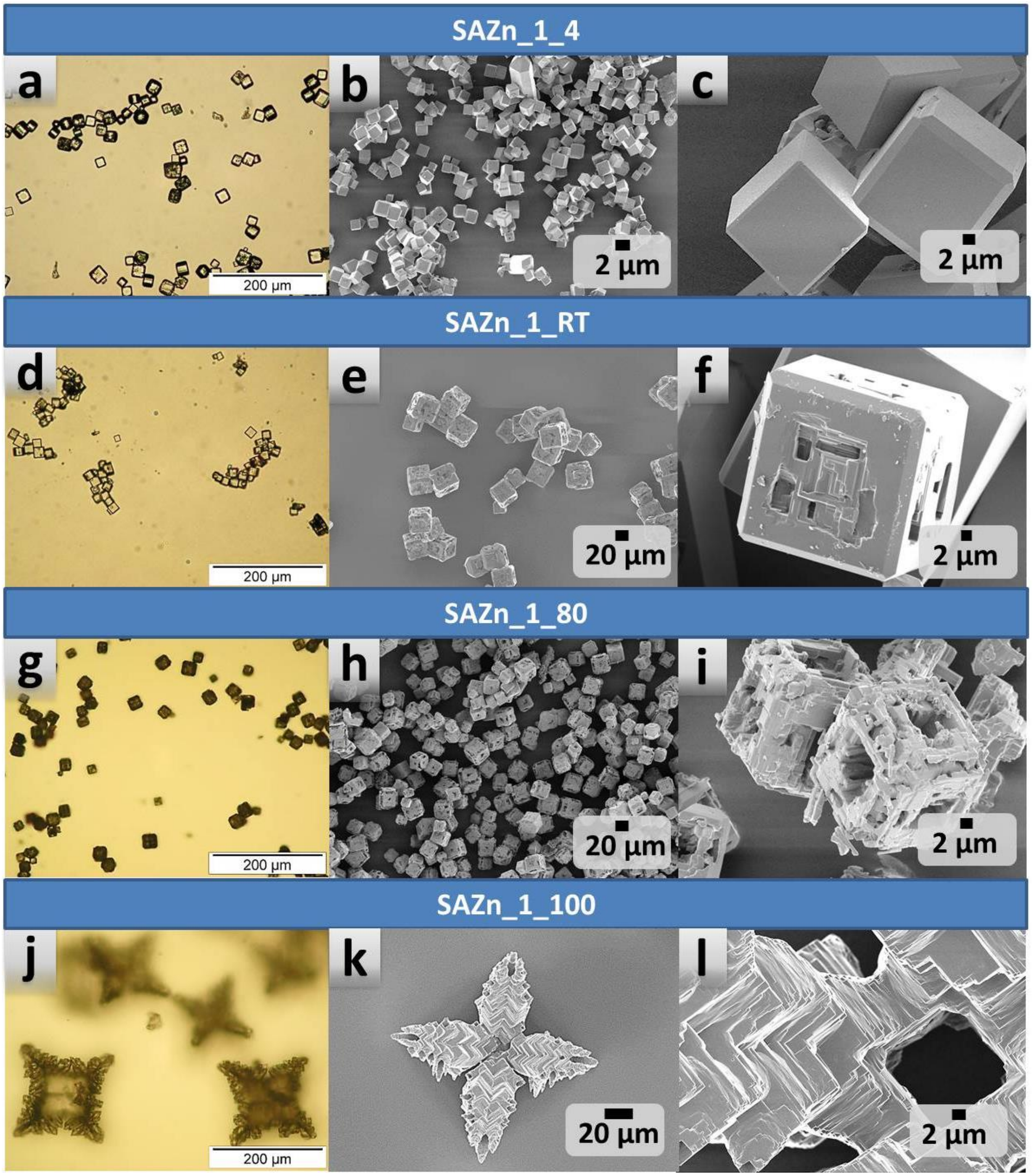

Figure 3.8 Crystal morphologies and shapes in dependence on the crystal aging temperature. (a,d,e,j) OM images of SAZn_1_4, SAZn_1_RT, SAZn_1_80 and SAZn_1_100, respectively. (b,c) SEM micrographs of SAZn_1_4, (e,f) SEM micrographs of SAZn_1_RT, (h,i) SEM micrographs of SAZn_1_80, (k,l) SEM micrographs of SAZn_1_100. Reproduced from Mani *et al.* with the permission from Wiley.[47]

3.2.1.2. Impact of the Squarate-metal molar ratio

The effect of the total metal ions concentration on the crystal growth process was investigated by varying the molar ratio of squaric acid to zinc from 1:0.5 to 1:2 at an aging temperature of 4 °C. The corresponding SEM images are presented in **Figure 3.9** and reveal that the SA/Zn molar ratio significantly impacts the crystal morphology. At low molar ratios (1:0.5), the cubes exhibit a truncated cube shape with striking large faces at the edges (i.e. $(101), (\bar{1}01), (10\bar{1}), (\bar{1}0\bar{1}), (011)$, $(01\bar{1})$, $(0\bar{1}1)$, $(0\bar{1}\bar{1})$ as well as $(110), (\bar{1}10)$, $(1\bar{1}0)$, and $(\bar{1}\bar{1}0)$). With the increase of the molar ratio to 1:1, the faces at the cube edges diminish and are even grown to full edges upon further increase of the molar ratio to 1:2. According to the non-classical crystallization theory, the driving force for the oriented attachment process is the reduction of the surface energy. In this context, the nanocrystalline building blocks are arranged into the growing crystals and aligned in such a manner that the high surface energy is minimized. Here, increasing the total concentration of the Zn ions increased the amount of nanocrystal building blocks that are available for structuration into highly ordered crystals with minimized surface energies. In this case, the thermodynamic equilibrium shape is achieved at the molar ratio of 1:2 (**Figure 3.9 c**). Further increase of the molar ratio to 1:3 yielded a mixture of crystals with different habits. This can be explained by the fact that the equilibrium ratio of 1:2 was exceeded and along with the particles that already reached the equilibrium shape, new crystals were formed by assembling the excess nanocrystals. It is to be noted that all crystals aged at 4 °C exhibit fully covered and smooth surfaces regardless of the SA/Zn molar ratio. Furthermore, the effect of the SA/Zn molar ratio on the face evolution and thermodynamics of the crystallization was observed irrespective of the aging temperature (**Figure S 2**).

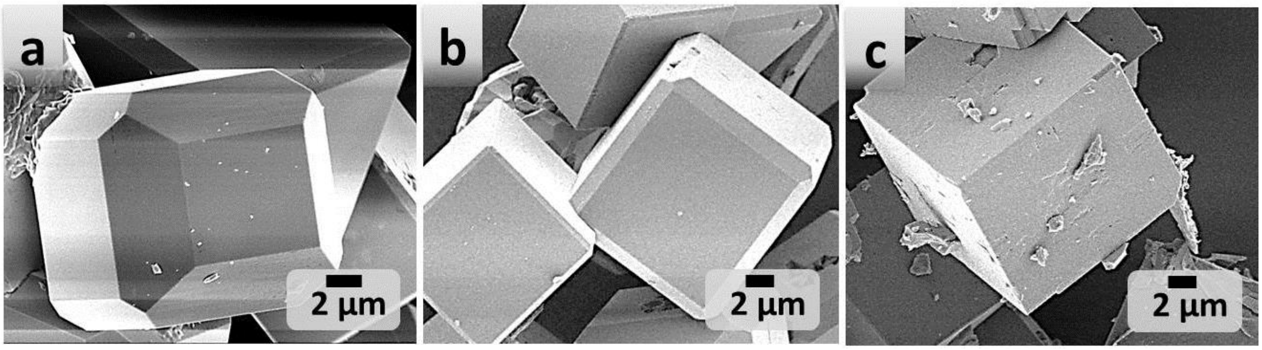

Figure 3.9 SEM micrographs of the squarate-zinc complexes aged at 4 °C at different SA/Zn molar ratios. a) SAZn_05_4. b) SAZn_1_4 and c) SAZn_2_4.

3.2.1.3. Impact of the solvent

Another crucial parameter that needs to be considered when designing crystalline materials is the solvent as it is known to influence the solubility of the components and thus the thermodynamics of the crystallization process. Furthermore, the solvent molecules themselves can coordinate to the metal ion and compete with the organic ligands, thus significantly affecting the crystal structure and consequently the particle morphology. In order to demonstrate the importance of the ligand-solvent interactions, SAZn_1_80 crystals were exemplarily synthesized in DMSO. The OM image of the resulting crystals reveals 2D micro-sized particles with a plate-morphology (**Figure 3.10 a**). The corresponding polarized OM image in **Figure 3.10 b** shows strong birefringence confirming the high degree of anisotropy in the material.

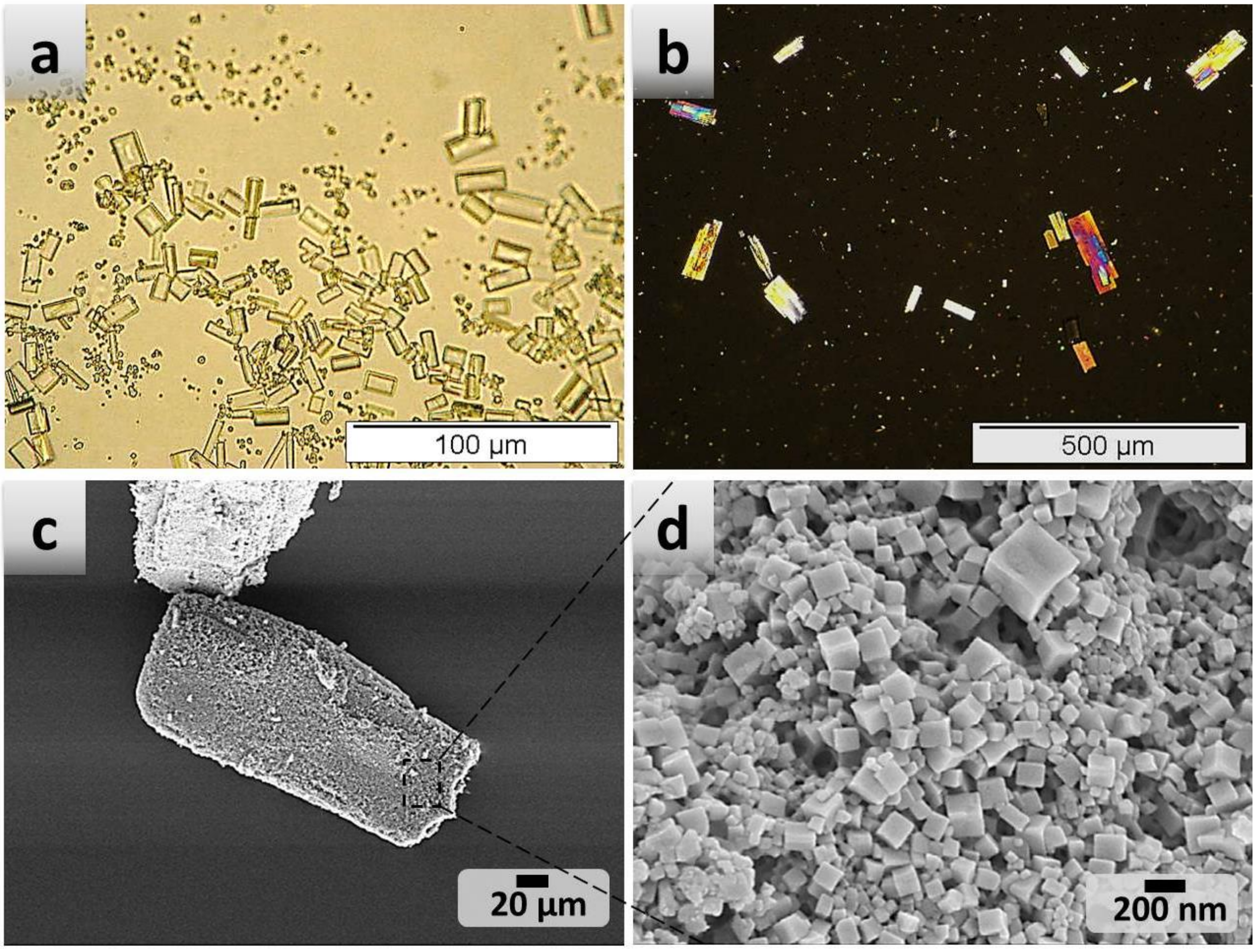

Figure 3.10 a) Optical microscope image of SAZn_1_80 crystals synthesized in DMSO, b) the respective polarized optical microscope image. c,d) SEM micrographs of SAZn_1_80 crystals synthesized in DMSO.

The high magnification SEM image (**Figure 3.10 c**) reveals that the plate crystals are composed of cube nanoparticles of several hundred nanometers in size, which are agglomerated in a disordered and random manner giving rise to the 2D superstructure. The high crystallinity of the material is again confirmed by XRD analysis, whereby the XRD pattern of the crystals synthesized in DMSO is identical to the pattern of the SAZn_1_80 crystals synthesized in water (**Figure 3.11**). Therefore, it can be suggested that both materials possess identical crystal structures and that the DMSO molecules compete neither with the squarate units nor with the coordinated water molecules. Consequently, it can be stated that the individual nanocrystals obtained in DMSO possess following crystal composition $Zn(H_2O)_2(C_4O_4)$. However, while the precipitation and formation of the primary nanocrystalline building blocks seems to occur irrespectively of the solvent system (water and DMSO), the subsequent assembly and orientation of the building blocks is shown to be significantly disturbed in DMSO. This can be attributed e.g. to differences in the interactions between the solutes and the solvent as well as to changes in the mass transport processes which also may affect the crystal growth processes and thus the resulting superstructure morphology.

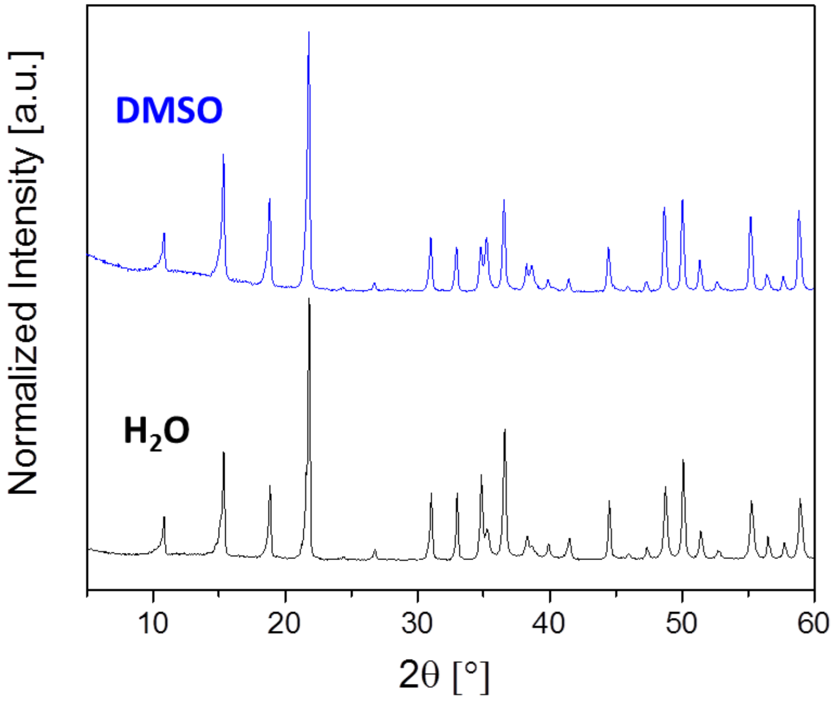

Figure 3.11 XRD diffractograms of the crystals of the squarate-zinc coordination complexes (SAZn_1_80) synthesized in DMSO (blue) and water (black).

3.2.2. Coordination complexes of the squarate ions with various divalent metal ions

A coordination compound is typically characterized by the nature of the metal ion, its oxidation state, and the number, kind, and arrangement of the ligands. The coordination behavior of the squarate ion in complexes with various metal ions is well investigated and reported in the literature. However, the synthesis of mesocrystalline superstructures based on these coordination compounds has not been reported, to the best of our knowledge. Aiming to understand how the choice of the metal ion can affect the structural and textural properties of the resulting crystals, we prepared crystals based on the coordination compounds of the squarate with Cu^{2+}, Ni^{2+}, Co^{2+}, and Cd^{2+}. In a typical synthesis aqueous solutions of SA and the acetate hydrate salts of the respective metals were mixed at RT at a molar ratio of 1:1 and aged at 80 °C overnight. The resulting crystals are named SACu_1_80, SANi_1_80, SACo_1_80 and SACd_1_80, respectively. As can be seen from **Figure 3.12**, crystals of SACu_1_80, SANi_1_80 and SACo_1_80 are colored, whereas the SACd_1_80 are colorless. Based on the Crystal Field Theory (CFT), the d-orbitals of a transition metal ion split into high energy and low energy orbital when ligands coordinate around the transition metal ion.[167] Thereby, the magnitude of the d-orbital splitting (Δ_0) relates to the energy required to promote an electron from the lower to the higher energy level.[168] Consequently, when light interacts with the sample, photons of the same energy as Δ_0 are absorbed and electrons are promoted into the higher energy orbitals. Based on the wavelength absorbed, the complex appears to the human eye in the complementary colors of the absorbed wavelength.[168] However, if the ions possess completely filled d-orbitals, as in the case of Zn^{2+} and Cd^{2+}, then their complexes appear colorless as there is no free orbital to promote the electrons into. The corresponding SEM images (**Figure 3.12**) of the crystals are presented for SACu_1_80, SANi_1_80, SACo_1_80 and SACd_1_80 and reveal that the morphologies of the crystals differ with the nature of the metal ion. For instance, crystals of SACu_1_80 exhibit an intriguing plate-like morphology, and the high-magnification SEM image of the crystals reveals that the micro-particles are composed of nanocrystals which are aggregate in a hierarchical manner.

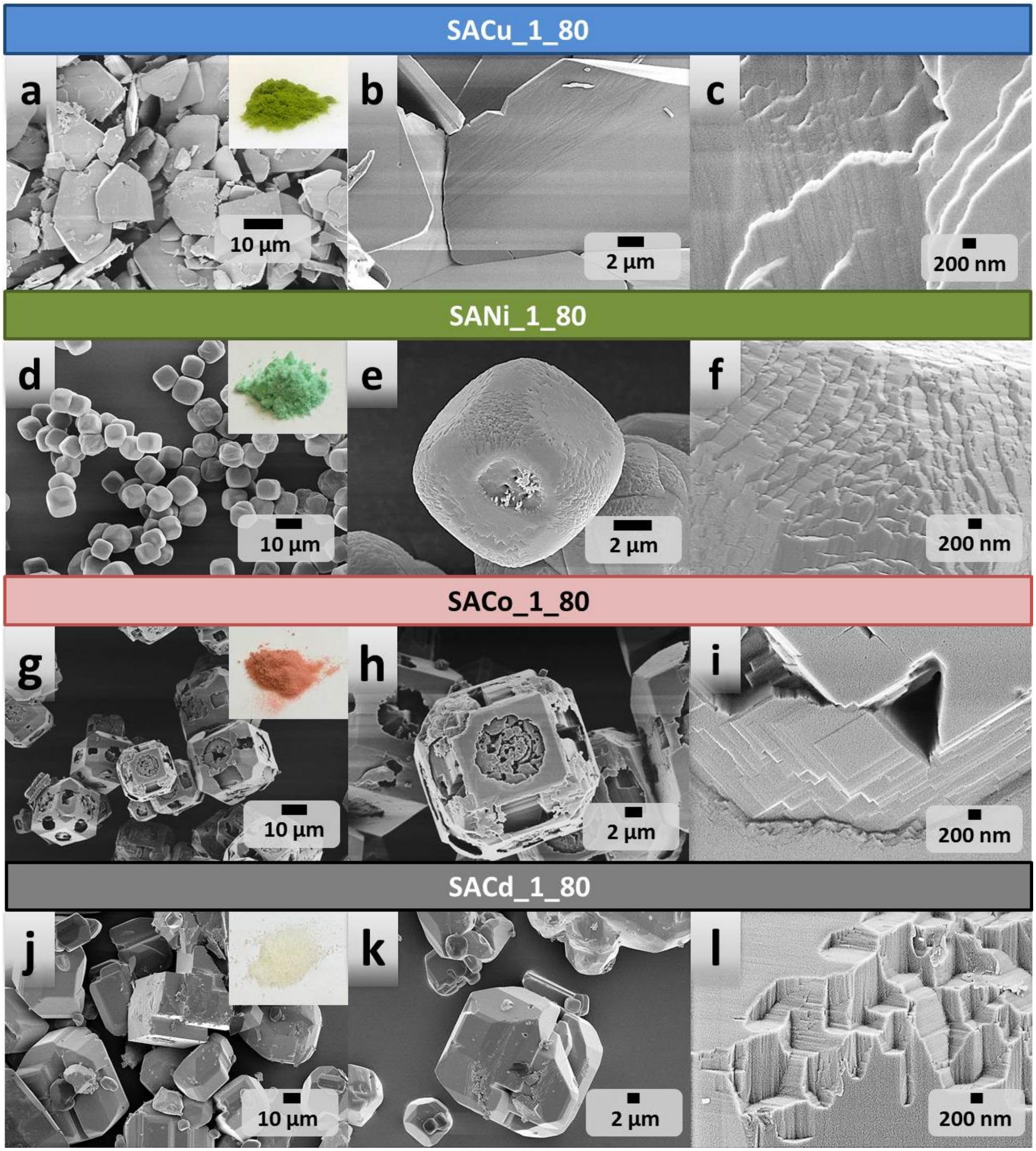

Figure 3.12 SEM micrographs of the coordination complexes of the squarate with various divalent metal ions. a-c) SACu_1_80, d-f) SANi_1_80, g-i) SACo_1_80, j-l) SACd_1_80. The insets in a,d,g,j show the respective microcrystalline samples which exhibit different colors.

Crystals of SANi_1_80 reveal a 3D cube morphology, similar to that observed for the squarate-zinc based crystals, and their mesocrystalline structure is evident from the high-magnification SEM image (**Figure 3.12 f**) which reveals the highly ordered arrangement of the single nanocrystalline building blocks. SEM images of the SACo_1_80 crystals (**Figure 3.12, g-i**) also exhibit an intriguing 3D cube shape, with truncated edges and openings on the high-index faces. SACo_1_80 crystals also exhibit a structure which is characteristic of a mesocrystal, as the high-magnification SEM reveals that the cubes are formed by the crystallographic arrangement of the single nanocrystalline building blocks. In contrast, mesocrystals based on squarate-Cd complexes (SACd_1_80) are polydisperse and not regularly shaped as the corresponding SEM images reveal (**Figure 3.12, j-l**). The crystalline nature of the respective mesocrystalline compounds and the differences in their crystal structure are shown by XRD analysis (**Figure S 5, Figure S 6, Figure S** 7). As reported before, mesocrystalline superstructures can form via different pathways, including the mesoscale assembly of organic-inorganic nanoparticles and the arrangement of primary nanocrystalline building blocks into iso-oriented crystals via the oriented attachment pathway. The latter is, among others, determined by the effective collision of nanocrystals which possess the same crystallographic orientation and by their subsequent arrangement into highly ordered 3D superstructures with minimized surface energy. In this context, varying the metal ion is a promising strategy to synthesize mesocrystals with different morphologies as the respective nanocrystal building blocks differ in their crystal structure and crystallographic orientation.

3.2.3. Croconate-Zinc coordination complexes

The choice of the ligand is also an important point which needs to be considered for the rational design of coordination compounds as it alters the coordination behavior of the metal ions and hence can lead to various crystal structures and morphologies. Herein, the organic ligand system is expanded to another member of the aromatic oxocarbon-anions family, namely the croconate. According to literature, the croconate ion represents a versatile organic ligand which can adopt a wide variety of coordination motifs in its complexes with various metal ions. In the following, the synthesis of crystals based on coordination compounds of the croconate with Zn ions is reported and will be discussed with regard to their structural properties. In a typical synthesis, aqueous solutions of croconic acid (CA) and ZAD were mixed at a CA/Zn molar ratio of 1:1 at room temperature (RT). The resulting colored crystals (CAZn_1_80) were then aged overnight at the 80 °C, then filtered, washed with water and finally dried in vacuum at 60 °C. OM and SEM images of the resulting crystals are presented in **Figure 3.13**, respectively, and reveal particles with an intriguing 3D hexagonal prism morphology. The optical microscope image shows strong birefringence which hinting to a high degree of anisotropy in the crystal. The crystals are polydisperse and exhibit particle sizes in the range between 20-70 nm in diameter. The high magnification SEM image (**Figure 3.13**) reveals that the crystal is composed of nanocrystals which are arranged in a hierarchical manner thus giving rise to a 3D superstructure which contains pores and voids between the single nanocrystals. The crystalline nature of the mesocrystalline CAZn_1_80 is also evident from XRD analysis (**Figure S 11**).

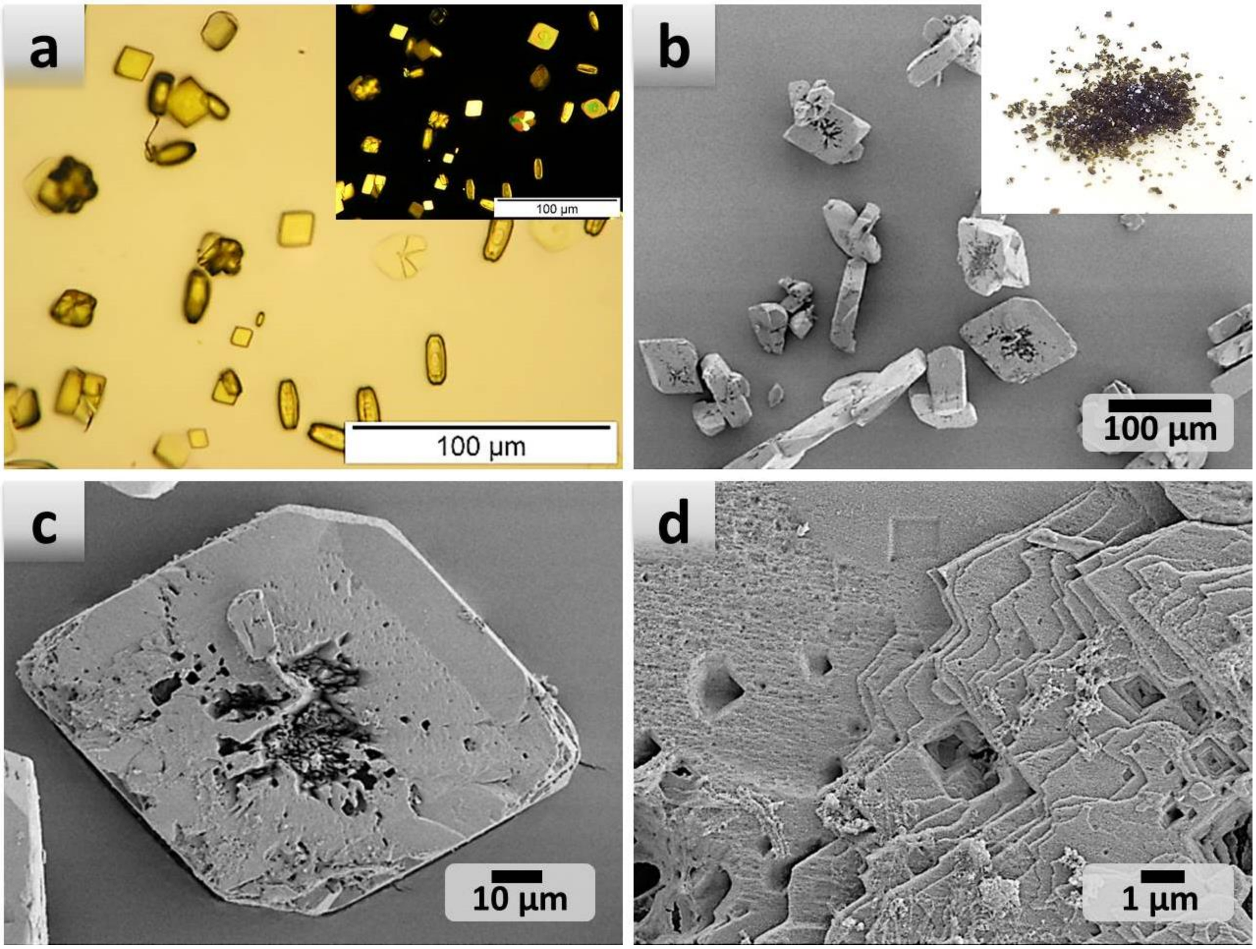

Figure 3.13 a) Optical microscope image of CAZn_1_80, b-d) corresponding SEM micrographs. The inset in (a) shows the polarized optical microscope image, in (b) shows the microcrystalline sample after washing in water and drying in vacuum.

Nitrogen sorption analysis reveals a type IV isotherm with a hysteresis loop of type H3, which according to IUPAC classification, is given by a mesopores structure consisting of non-rigid aggregates of plate-like particles but also by macropores which are not filled at the atmospheric pressure ($P/P_0 = 1.0$).[165] The BET surface area and total pore volume were determined to be 30 $m^2\,g^{-1}$ and 0.04 $cm^3\,g^{-1}$, respectively.

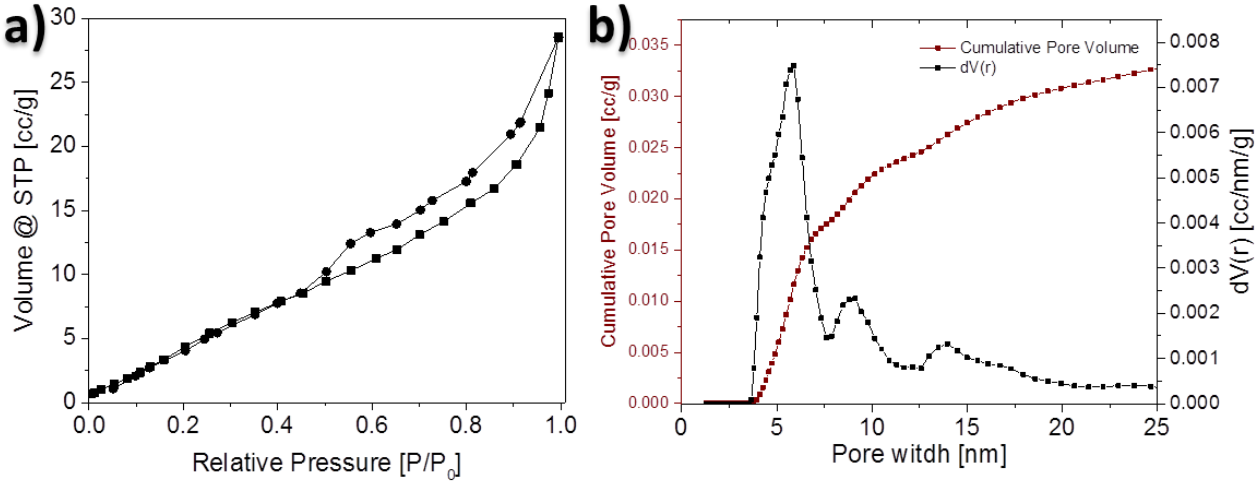

Figure 3.14 a) Nitrogen sorption isotherm of the coordination complex CAZn_1_80, b) corresponding PSD curve calculated based on the NLDFT model for slit and cylindrical pores.

The variation of the organic ligand system is shown to represent a further useful strategy in order to prepare mesocrystalline materials with intriguing 3D geometries. The distinct particle shape and size, which clearly differs from the shapes and sizes of the mesocrystals obtained with squarate-based coordination complexes, can be attributed to the different crystal structures and hence crystallographic orientation of the nanocrystals. This leads to a distinct shape evolution as the individual nanocrystal building blocks arrange in a different manner. The resulting mesocrystal CAZn_1_80 also shows the tendency for the formation of micro-sized openings at the face centers, which again can be attributed to the outward diffusion process of Zn atoms due to the Kirkendall effect.

4. Functional Porous Carbon-based Materials

4.1. Background and State-of-the-Art

The term "functional material" basically describes a compound which possesses the ability to perform a certain function in a specific application.[17] Here, materials can be processed in such a way that they acquire certain chemical and/or physical properties which are necessary to exhibit a specific function. This is important as on the molecular scale the properties of a material strongly rely on their structure and/or morphology.[169, 170] For instance, hierarchically porous carbons combine properties such as high surface area, excellent electrical conductivity and high chemical and thermal stability with a 3D interconnected pore structure consistent of micro-, meso- and macropores.[78, 171] Owing to this wide spectrum of properties they are considered as material of choice in several energy and environment-based applications. In this context, they can serve as catalyst support, adsorbent, gas storage and electrode material for energy storage applications, among others.[56, 172, 173] More function can be added to the carbon materials by incorporating heteroatoms (e.g. N, B, S, P, metals etc.) into the carbon structures, which may affect properties such as wettability, surface polarity as well as the electrochemical landscape.[7, 174] State-of-the-art synthesis of functional hierarchically porous carbon commonly involves the combination of template-assisted methods with chemical or physical activation of the carbon.[171] Besides, Antonietti *et al.* reported on the preparation of hierarchically porous carbon aerogels via the HTC process of carbohydrates.[24, 25]

An alternative approach, which allows guiding and controlling the properties of the resulting nanoporous carbons in a facile manner includes the molecular design of porous carbon materials.[7, 27] This approach is based on the use of molecular building blocks such as ionic liquids, bio molecules, or coordination compounds with predefined structural and compositional characteristics as carbon precursors, allowing for the more rational design of functional hierarchically porous carbons with defined architectures and advanced properties.

Using porous coordination complexes as carbon precursor i.e. crystalline materials which are constituted of rigid organic molecules coordinated to metal ions to form 1D-, 2D-, or 3D structures, [35-37] is beneficial from the standpoint of material design as they exhibit a wide range of chemical and physical properties which can be easily controlled by proper crystal engineering. In this context, MOFs have attracted much attention as precursor material for preparing nanoporous composite and carbon materials possessing high surface areas and total pore volumes. In 2012, various research groups reported simultaneously on the synthesis of nanoporous carbons via the direct carbonization of MOFs without the need of any additional carbon source.[89, 175, 176] Thereby, the structural and textural properties of the resulting composites and carbons strongly depended on the type of MOF used as well on the carbonization temperature. For instance, Yang *et al.* synthesized hierarchically porous carbons consisting of ultramicro-, micro-, meso- and macropores with large BET surface areas of up to 3174 m^2 g^{-1} and high total pore volumes of up to 4.06 cm^3 g^{-1} via the direct carbonization of IRMOFs at 900 °C for 3h.[89] Here, the thermal conversion of the IRMOFs to the respective porous carbon was based on the partial decomposition of the organic ligands along with the release of CO_2 and CO. Moreover, intermediately formed ZnO is reduced in the presence of the carbonaceous material to Zn, which then vaporized upon heating at 900 °C for 50 min. By using the commercial available ZIF-8 as carbon precursor, Chaikittisilp *et al.* synthesized nanoporous carbons with maximum BET surface areas and total pore volumes of 1110 m^2 g^{-1} and 0.62 cm^3 g^{-1} via the direct carbonization at 1000 °C.[176] However, the ZIF-8 derived carbons were mainly microporous and required a washing step with HF and water in order to remove residual inorganic components. In all the cases reported so far, the structural characteristics of the pristine crystalline precursors could be preserved throughout the whole carbonization process allowing for the synthesis of carbon-based materials with intriguing 3D morphologies.

In general, nanoporous composite and carbon materials derived from the direct carbonization of MOFs have been shown to exhibit good performances in their applications in heterogeneous catalysis, gas storage as well as electrochemical energy storage and conversion. Given the various structures known for MOFs, composite and carbon materials with different topologies, porosities and functionalities could be realized. In this context, Torad *et al.* reported on the synthesis of a composite constituent of magnetic Co nanoparticles well-dispersed on a carbon framework by the facile heat treatment of the cobalt-based MOF ZIF-67.[90] The resulting composites exhibited a moderate surface area (345 m^2 g^{-1}) along with highly graphitized carbon frameworks which were attributed to the catalytic graphitization effect of the Co nanoparticles. Owing to their graphitic nature, ZIF-67-derived carbons showed superior capacitance retention in their use as supercapacitor electrode material compared to the ZIF-8-derived porous carbons.[177]

However, owing to the low thermal stabilities of the MOFs and the lack of understanding of the transformation processes during the heat treatment at temperatures up to 1000 °C, control over the pore structures and morphologies is poor and limits the use of MOFs as carbon precursor.[178] For certain MOF structures, such as MOF-5 and Cu-BTC, partial collapse of the pore structures after the heat treatment step were reported resulting in carbon materials with disordered pore structures.[42]

Aiming to overcome these limitations, our group developed a facile synthesis route for the preparation of nanoporous carbon materials. Here, coordination complexes of polyphenols with metal ions allowed for the formation of very well organized 3D frameworks, that assembled in an ordered manner into stable mesocrystals.[46] These pre-defined mesocrystalline structures could be easily transformed into hierarchically porous carbon materials with high carbonization yields by their direct carbonization without the need of classical hard or soft templates.

In the preceding chapter, crystalline microparticles were synthesized based on the coordination of squarate ions to metal ions. This enabled the formation of well-organized 3D frameworks, which are stabilized by the strong coordinate bonds as well as by intermolecular π-π interactions and by strong hydrogen-bonds between the squarate and coordinated water molecules.[136, 137] By the careful choice of the metal ions and organic building units as well as by adjusting synthesis parameters such as temperature and total metal ion concentration, properties on the macroscopic scale (e.g. shape and arrangement) as well as on the molecular level (e.g. chemical functionality, porosity) could be controlled. Herein, these complexes, which possess pre-defined structural information, are used as precursor to prepare nanoporous composite and carbon materials with advanced properties.

4.2. Composite and carbon materials derived from squarate-zinc complexes

In chapter 3, the coordination complexes of squarate ions and Zn^{2+} were shown to possess an intriguing 3D cube morphology as well as a pre-defined hierarchical pore structure. By adjusting the crystal aging temperature from 4 to 80 °C, the crystal morphology could be successfully tuned from covered and dense cube particles with smooth surfaces to cube particles with intriguing 3 µm sized openings face-centered on each side of the cube. The direct heat treatment of these complexes at elevated temperatures represents a facile approach to convert these mesocrystalline particles into the corresponding nanoporous composite and carbon materials with high surface areas and total pore volumes. The benefit of this approach is that it allows for the rational design of the carbon structures and properties by defining the structural and textural characteristics of the coordination complexes and their controlled arrangement into crystalline 3D mesostructures.

For the synthesis of the nanoporous carbon materials, two different strategies were developed. By heat treatment at 900 °C in a nitrogen atmosphere, the complex SAZn_1_80 was successfully converted into the respective composite material. Subsequent washing with a 1 *M* HCl solution and water yielded the respective carbon material. Alternatively, direct heat treatment of the crystalline SAZn_1_80 at 1000 °C enabled the one-step preparation of the carbon material without the need of a washing step. Here, the temperature of 1000 °C was chosen in order to facilitate the carbonization process along with the evaporation of Zn which typically boils at 907 C.[179, 180] The resulting composites and carbons were finally obtained at yields of 30 and 16 %, respectively, and are denoted as SAZn_1_80_CM, SAZn_1_PC and SAZn_1_DPC, respectively, where CM refers to composite material, PC to porous carbon and DPC to direct porous carbon. SEM images of the respective composites and carbons are presented in **Figure 4.1** showing that all the materials consist of 3D cube shaped particles with openings of approximately 3 µm face-centered on each side of the cube. From the overview SEM image of the carbon SAZn_1_80_PC (**Figure 4.1 d**), it can be seen that the carbon cube particles are uniform in size and, furthermore, could be preserved throughout all processing steps emphasizing the high stability of the prepared materials. Overall, it is shown that the morphology of the pristine crystalline SAZn_1_80 could be maintained throughout the whole synthesis procedure and this emphasizes the high stability of the prepared materials. From the high-resolution SEM image of the carbon material (**Figure 4.1 e**) the porous nature of the carbon cubes becomes evident, as the image reveals the presence of meso- as well as macropores in the carbon framework.

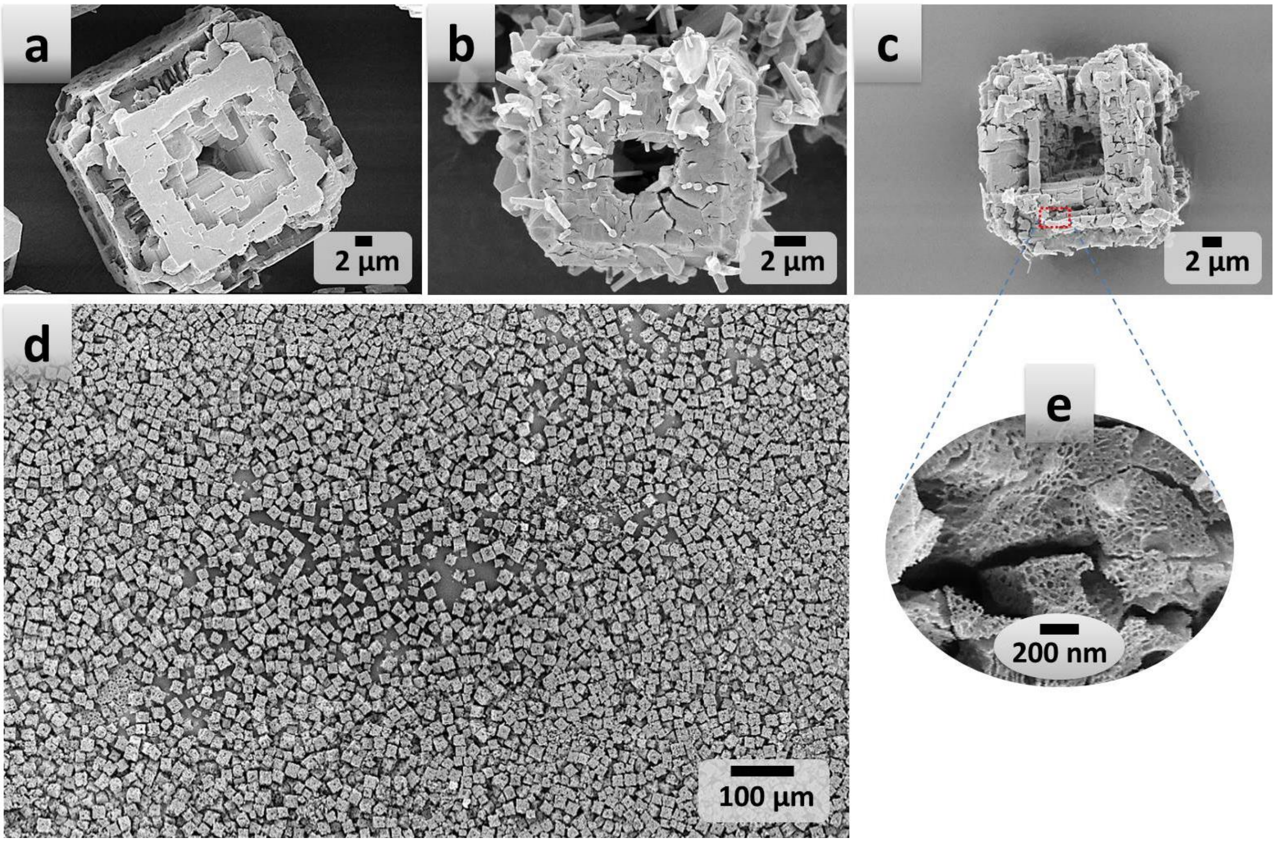

Figure 4.1 SEM micrographs of a) the mesocrystalline SAZn_1_80, (b) the corresponding composite material SAZn_1_80_CM, (c) the porous carbon SAZn_1_80_PC, (d) overview micrograph of SAZn_1_80_PC, and (e) high maginification micrograph of showing the pores in the carbon structure of SAZn_1_80_PC. Reproduced from Mani *et al.* with the permission from Wiley.[47]

The XRD diffractograms of the prepared materials are depicted in **Figure 4.2 a**. The XRD pattern of the composite material, SAZn_1_80_CM, displays reflections at $2\theta = 31.7°$, 34.5°, 36.3°, 47.6° and 56.6°, which can be well indexed and assigned to the (100), (002), (101), (102) and (110) planes of crystalline ZnO. In contrast, the XRD patterns of the carbons SAZn_1_80_PC and SAZn_1_80_DPC do not reveal any signals characteristic of the crystalline ZnO phase. Here, the low signal intensities point to an amorphous carbonaceous material. Analysis of the elemental composition via elemental analysis (EA) and inductively coupled plasma optical emission spectroscopy (ICP-OES) (**Table 2**) reveal a Zn content of approximately 59 wt% for the composite SAZn_1_80_CM, whereby an insignificant amount of Zn (0.13 wt%) was detected in the washed porous carbons SAZn_1_80_PC. It is suggested that during the heat treatment process to 900 °C, the carbonaceous framework is formed along with ZnO nanoparticles. The latter could be removed to a large extend from the carbon framework by washing with 1 *M* HCl and water. Alternatively, upon heat treatment at 1000 °C, the as-formed ZnO nanoparticles can be reduced to metallic Zn by the carbon (carbothermal reduction), whereby Zn subsequently vaporizes at such high temperatures and is released during the heating process.[180]

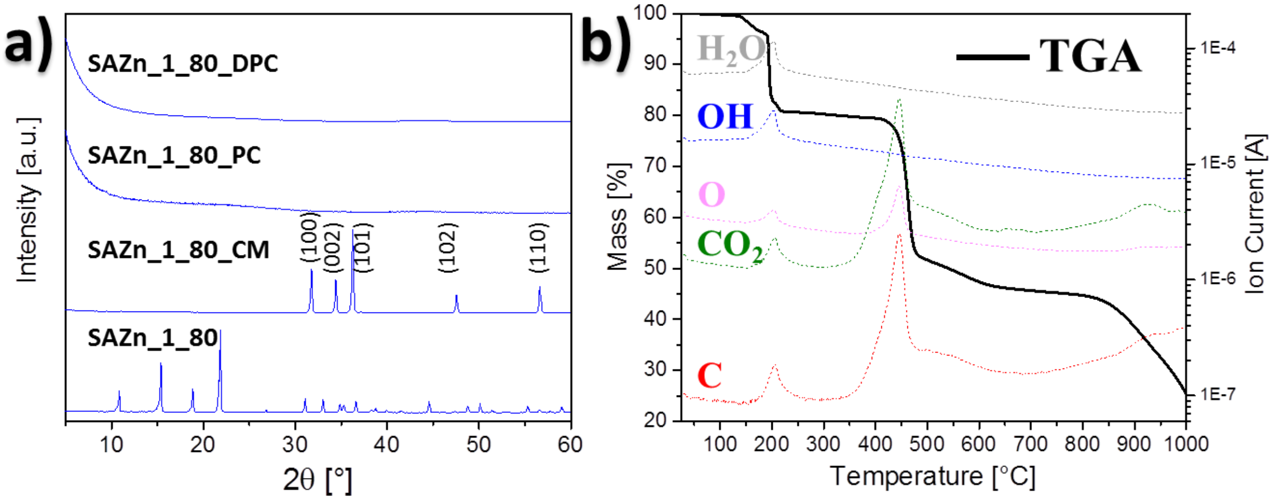

Figure 4.2 a) XRD diffractograms of the complex SAZn_1_80, the composite material SAZn_1_80_CM, the porous carbon SAZn_1_80_PC and the carbons obtained by direct carbonization SAZn_1_80_DPC. b) TGA-MS profile of the complex SAZn_1_80 with signals which can be assigned to C (red), CO_2 (green), O (pink), OH (blue) and H_2O (grey), measured in nitrogen atmosphere at a heating rate of 10 °C min^{-1}.

The thermal stability and degradation profile of the complex SAZn_1_80 was evaluated using thermogravimetric analysis (TGA) in nitrogen atmosphere coupled with mass spectroscopy (MS) (**Figure 4.2 b**). Supported by mass spectroscopy (MS), the TGA profile reveals mass loss of approximately 20.5 % at 200 °C which can be assigned to the loss of water and small amounts of CO_2. The subsequent degradation steps involve partial decomposition of the squarate unit which is disclosed in a two-step preceding release of CO_2 and CO at 465 °C and 560 °C with mass losses of 27 % and 7 %, respectively. The degradation step at 910 °C is accompanied with a mass loss of 20.5 % and is ascribed to the release of Zn that typically boils at 907 °C.[179] The residual mass of 25 % can be considered mainly being constituent of carbon. Nitrogen sorption measurements were performed in order to obtain more insights into the pore structure of the prepared materials. The surface area, total pore volume and pore size distribution were determined using the Brunauer-Emmet-Teller (BET) model and the nonlocal density functional theory (NLDFT) equilibrium model method for slit and cylindrical pores, respectively.

As the nitrogen sorption isotherms in **Figure 4.3 a** reveal, the materials SAZn_1_80_CM, SAZn_1_80_PC and SAZn_1_80_DPC exhibit similar sorption profiles. In this context, the isotherms show a steep uptake at low relative pressure ($P/P_0 < 0.1$) due to the filling of micropores, followed by a hysteresis loop at high relative pressure between 0.4 and 0.9, which is associated to capillary condensation in the mesopores. Moreover, the isotherms reveal a steep uptake at high relative pressure ($P/P_0 > 0.8$) whereby no final saturation plateau can be observed. This indicates the presence of macropores that are not completely filled with nitrogen at the atmospheric pressure ($P/P_0 = 1.0$).[165] According to IUPAC convention, the observed hysteresis loop can be assigned to type H4 which is characteristic of hierarchical porous materials consisting of micro-, meso- and macropores.[64] Furthermore, all hysteresis loops close at the same point, namely at relative pressures between 0.4 and 0.5 and therefore can be ascribed to a cavitation controlled evaporation of the adsorbate from the pore networks.[164] This suggests a system consisting of mesopores that are only accessible through pores of diameters below 5 nm.[165] Recent work has revealed that in the case of pore diameters smaller than 11 µm the closure point of the hysteresis, i.e. the onset of cavitation strongly depends on the pore size and geometry.[181] Based on these observations, it can be deduced, that the composites, the washed as well as the direct obtained carbons possess a well-developed hierarchical pore structure of interconnected micro-, meso- and macropores, which is inherited from the mesocrystalline SAZn_1_80. Within the series, the surface area and the total pore volume increased from the crystalline SAZn_1_80 over the composite SAZn_1_80_CM to the porous carbons SAZn_1_80_PC and SAZn_1_80_DPC (**Table 2**) along with an increased total nitrogen uptake and enlargement of the hysteresis loops indicating enhanced mesopores contributions. The highest surface area and total pore volume of 1957 $m^2\ g^{-1}$ and 2.31 $cm^3\ g^{-1}$, respectively, could be realized for SAZn_1_80_DPC. Based on the above results, it can be suggested that ZnO clusters are formed during the heating process to 900 °C along with the evolution and release of CO and CO_2 resulting in an accessible nanoscale porosity. Here, the as-formed ZnO nanoparticles, that are well-distributed throughout the carbon framework, are suggested to act as a local template allowing for the formation of new pores and the development of the pre-defined hierarchical pore structure upon their removal by the washing process.[46, 88] Alternatively, a well-developed pore structure is obtained due to the carbothermal reduction of the as-formed ZnO nanoparticles and subsequent evaporation of the resulting Zn at temperatures above 900 °C along with the release of CO_2 and CO. This molecular etching process not only allows for the effective removal of the inorganic compounds but also for the controlled formation of well-accessible pores.[182]

The corresponding PSD curves (**Figure 4.3 b**) reveal similar pore size distributions for all the materials investigated showing narrow peaks with maxima around pore diameters of 5.3 nm and 1.7 nm, respectively. In agreement with the results from the previous studies, this outcome supports the suggestion that the prepared materials possess a 3D hierarchically porous structure.

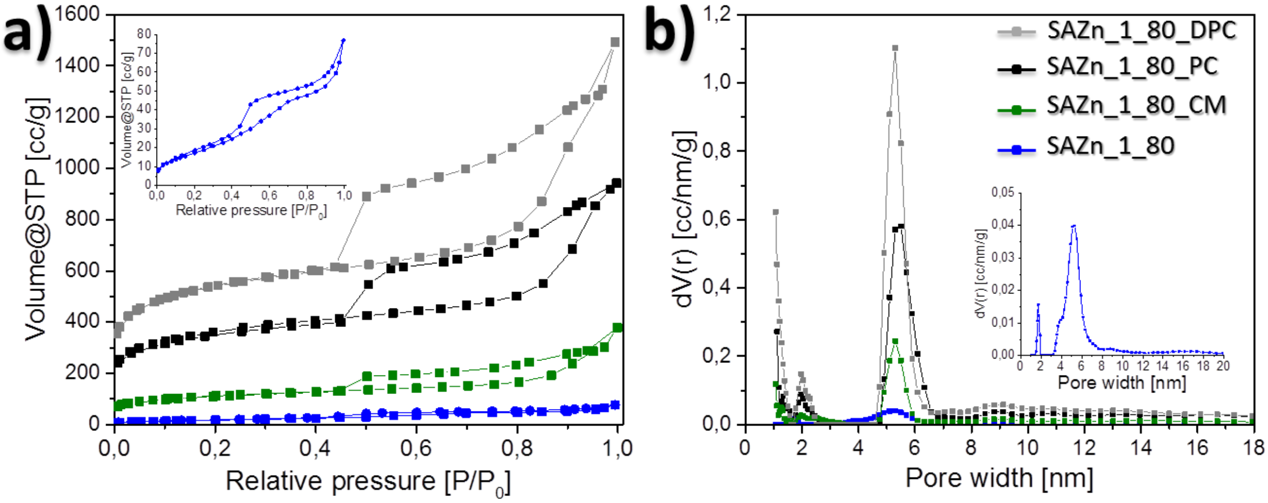

Figure 4.3 a) Nitrogen sorption isotherms of the complex SAZn_1_80 (blue), the composite SAZn_1_80_CM (green), the washed carbon SAZn_1_80_PC (black), and the direct obtained SAZn_1_80_DPC (grey). b) Corresponding PSD curves calculated based on the NLDFT model for slit and cylindrical pores. The insets in (a) and (b) represent the high-magnification of the resulting diagrams of SAZn_1_80.

In conclusion, the coordination complex SAZn_1_80 were shown to be a suitable precursor for the preparation of nanoporous composite and carbon materials. Here, the structural and textural properties of the pristine crystalline particles (i.e. shape, morphology, and pore structure) could be successfully transferred to the final products. This strategy allows for the rational design of functional hierarchical porous carbon materials.

Table 2 Nitrogen sorption, elemental analysis and ICP data for the prepared materials.

Compound	**S_{BET} [m^2g^{-1}]**	**Pore volume [cm^3g^{-1}]**			**Elemental Analysis [wt %]**			**ICP [wt.%]**
		Total	*Micro*	*Meso*	*C*	*H*	*O*	*Zn*
SAZn_1_80	67	0.12	0.03	0.09	23.5	2.2	42.4	
SAZn_1_80_CM	519	0.71	0.2	0.51	26.1	0.8	14.1	58.8
SAZn_1_80_PC	1296	1.46	0.52	0.94	89.4	1.6	3.2	0.13
SAZn_1_80_DPC	1957	2.31	0.78	1.53	93.2	1.5	2.9	

4.3. Composite and carbon materials derived from coordination complexes of squarate units with various metal ions

The squarate represents a very versatile ligand system able to adopt a variety of coordination modes in its reaction with various metal ions. In this context, various crystal structures have been reported depending on the nature of the metal ions yielding intriguing 3D architectures, which are stabilized by the coordinate bonds as well as intermolecular hydrogen bonds and π-π interactions among the squarate units.[132, 137, 183] Inspired by this, in chapter 3, we introduced coordination complexes obtained by the reaction of the squarate with the d-block metal ions Cu^{2+}, Ni^{2+}, Co^{2+} and Cd^{2+} in aqueous solution, respectively. The resulting coordination complexes (named SACu_1_80, SANi_1_80, SACo_1_80 and SACd_1_80, respectively) were shown to exhibit varying structures and shapes as a result of the different coordination modes that the squarate ligand can undergo with different metal ions. Benefiting from their unique structural characteristics, which can be easily designed by assembling appropriate building units as well as adjusting the synthesis conditions such as temperature and concentration, the corresponding squarate-metal complexes represent suitable precursors for the rational design of nanoporous carbons following the molecular design concept:

Herein, the complexes SACu_1_80, SANi_1_80, SACo_1_80 and SACd_1_80 are employed as precursors to prepare functional nanoporous carbon materials with various structures, morphologies and porosities. By heat treatment at 900 °C in a nitrogen atmosphere followed by a washing step, these complexes could be successfully converted to the respective composite and carbon materials, respectively. These products are denoted as SACu_1_80_CM, SANi_1_80_CM, SACo_1_80_CM and SACd_1_80_PC, where CM refers to composite materials and PC to porous carbons. The SEM images of the respective materials obtained after the acid washing step are shown in **Figure 4.4** and reveal that the morphologies and shapes of the pristine complexes could be successfully preserved throughout the thermal conversion procedure and therefore transferred to the respective composites and carbons. In this context, SACu_1_80_CM exhibits microparticles with a 2D plate-like morphology and the high-magnification SEM image reveals the presence of nanoparticles which are well-dispersed over the carbon phase.

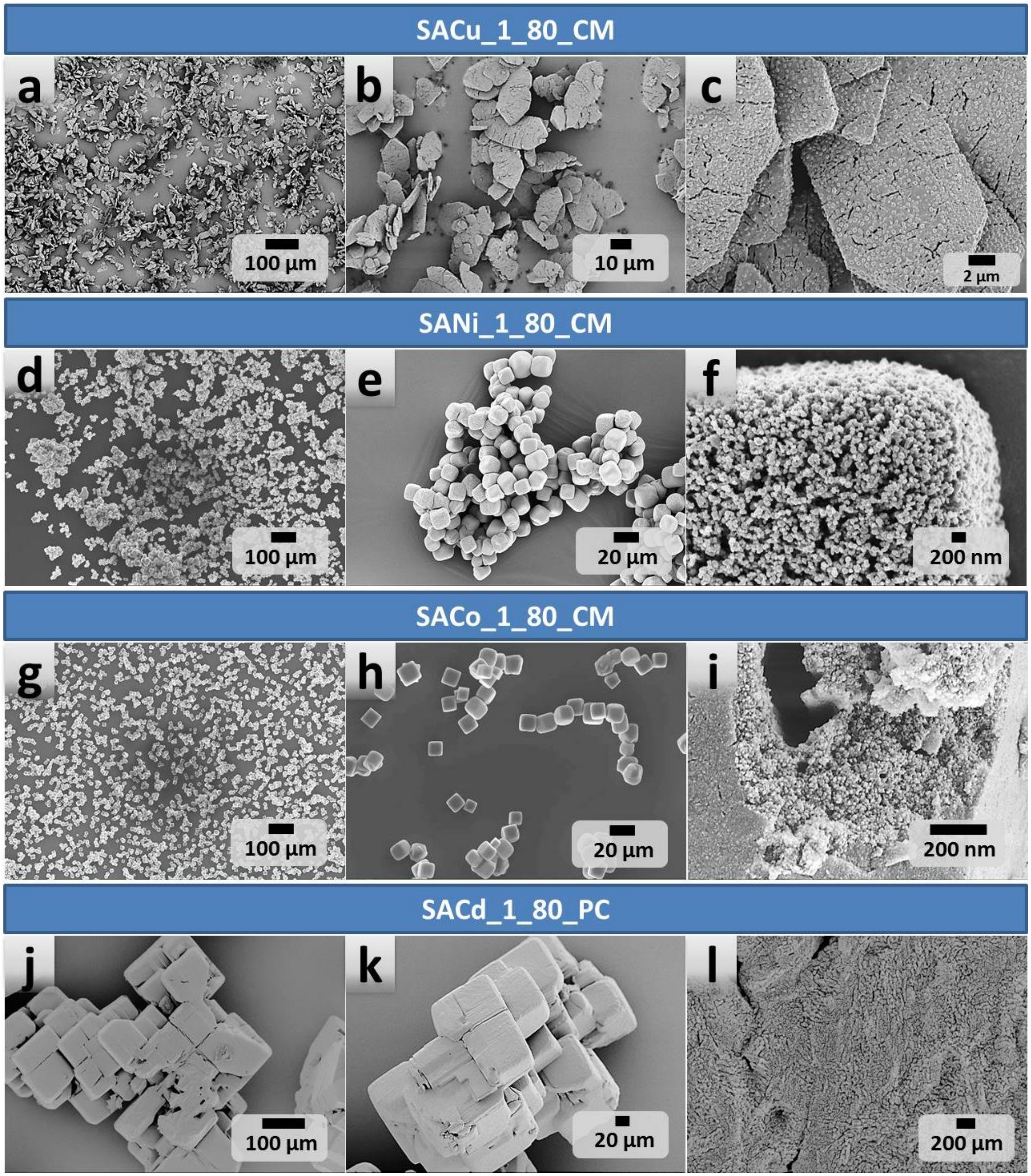

Figure 4.4 SEM micrographs of the composites and carbons derived from the coordination complexes of the squarate units with various metal ions. a-c) SACu_1_80_CM, d-f) SANi_1_80_CM, g-i) SACo_1_80_CM, and j-l) SACd_1_80_PC.

SEM images of SANi_1_80_CM reveal regular shaped microparticles with a 3D cube morphology. The high-magnification SEM image shows that the cube particles are mainly composed of densely packed nanoparticles, whereby interspacial voids between the nanoparticles can be observed. SACo_1_80_CM exhibits a similar 3D cube morphology with nanoparticles dispersed throughout the carbon phase. SEM images of SACd_1_80_PC reveal irregular shaped particles inherited from the corresponding complex.

More insights into the structural differences between the prepared composites and carbon materials were obtained by XRD analysis (**Figure 4.5**). The XRD pattern of SACu_1_80_CM reveals sharp and intense reflexes around 2θ values of 44.5 and 51.9° that can be assigned to the (111) and (200) crystal planes of metallic Cu.[184] The diffractograms of SANi_1_80_CM shows sharp reflections around 2θ values of 44.5 and 51.9° which can be well indexed to the (111) and (200) planes of metallic Ni. The XRD pattern of the composite material SACo_1_80_CM shows broad curves hinting to an amorphous material whereby a small sharp peak can be observed around 2θ=44.3° suggesting the presence of a Co phase with a higher crystallization degree. In contrast, the XRD pattern of SACd_1_80_PC does not reveal reflections characteristic of any crystalline nanoparticles and is suggestive of an amorphous carbon material. Based on the above results, it is suggested that heat treatment of the complexes SACu_1_80, SANi_1_80 and SACo_1_80 at 900 °C in a nitrogen atmosphere leads to the formation of corresponding metal-oxide nanoparticles, which subsequently undergo carbothermal reduction to form the corresponding metallic Cu, Ni and Co nanoparticles, respectively. The as-formed metal nanoparticles are mixed that tightly with the carbon framework that they could not be removed during the acid washing process. However, during the heat treatment of the crystalline SACd_1_80 at 900 °C in a nitrogen atmosphere, CdO was produced, which was then reduced to metallic Cd by the carbon. These structural differences, that can be largely attributed to the different boiling points of the metals, is also evident from the thermal degradation profiles of the respective materials, which reveal differences in their thermal stabilities (**Figure S 14**).

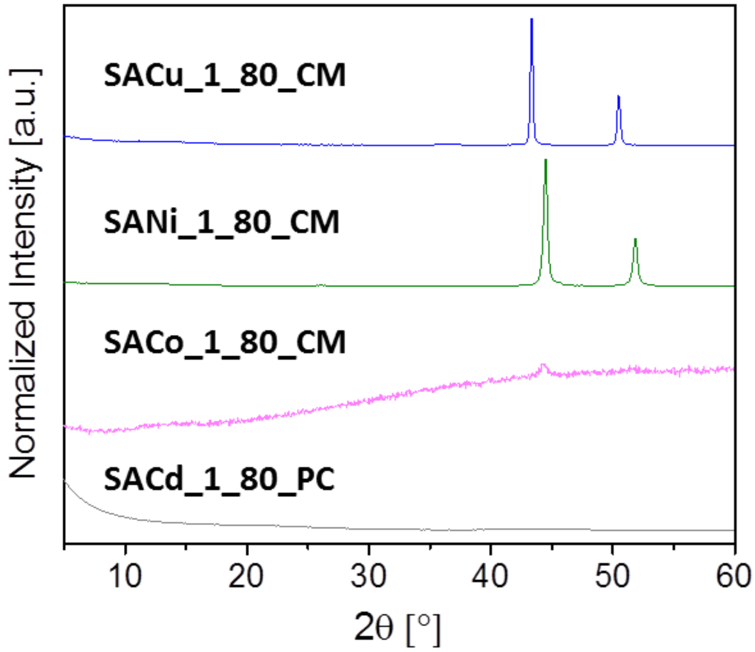

Figure 4.5 XRD diffractograms of SACu_1_80_CM (blue), SANi_1_80_CM (green), SACo_1_80_CM (pink), SACd_1_80_PC (grey).

According to IUPAC classification, the nitrogen sorption isotherm of the Cu-carbon composite, SACu_1_80_CM, reveals combined characteristics of type I and type IV isotherms with a multi-step nitrogen uptake at high relative pressures (P/P0 > 0.8). Furthermore, the isotherm exhibits a type H3/H4 hysteresis with a closure at relative pressures between 0.4 and 0.5, which is typical for a cavitation effect in mesopores. Based on these observations, it is suggested that the composite material SACu_1_80_CM possesses macropores, which are not filled with nitrogen at the saturation pressure, as well as mesopores and micropores, whereby a broad pore size distribution is expected in the mesopores range. The cavitation step in the hysteresis closure hints to the fact that the mesopores are connected to or only accessible by the micropores. SANi_1_80_CM reveals a type III isotherm which is characteristic of a nonporous material. The uptake observed at very high relative pressure ($P/P_0 > 0.9$) can be ascribed to adsorption of nitrogen on the external surface and void spaces between the dense packed nanoparticles. SACo_1_80_CM exhibits a nitrogen isotherm profile similar to SACu_1_80_CM, i.e. contributions of macropores as well as interconnected meso- and micropores. The nitrogen sorption isotherm of SACd_1_80_PC reveals a steep uptake at low relative pressures ($P/P_0 > 0.1$) associated with the presence of micropores followed by two distinct capillary condensation steps that are suggestive of a narrow bimodal pore size distribution in the mesopores range. Based on this isotherm pattern, the carbon SACd_1_80_PC is suggested to possess a hierarchical pore structure with macropores and interconnected meso- and micropores. Moreover, the isotherm of SACd_1_80_PC reveals much higher nitrogen uptakes when compared to the isotherms of the composites materials other (SACu_1_80_CM, SANi_1_80_CM, and SACo_1_80_CM). This indicates that the carbons derived from the squarate-cadmium complexes have a larger surface area and a higher total pore volume compared to other materials displayed in **Figure 4.6 a**. This can be explained by the fact that during the thermal carbonization of SACd_1_80 at 900 °C, carbothermal reduction of the as-formed CdO particles produces metallic Cd which is vaporized and released around 767 °C along with CO and CO_2. This so-called “molecular etching” facilitates the development of well-accessible pores and can increase the accessible surface area and the total pore volume. It is also to be noted that the herein investigated composite materials still possess significant high metal contents and correspondingly high mass densities resulting in lower specific surface areas.

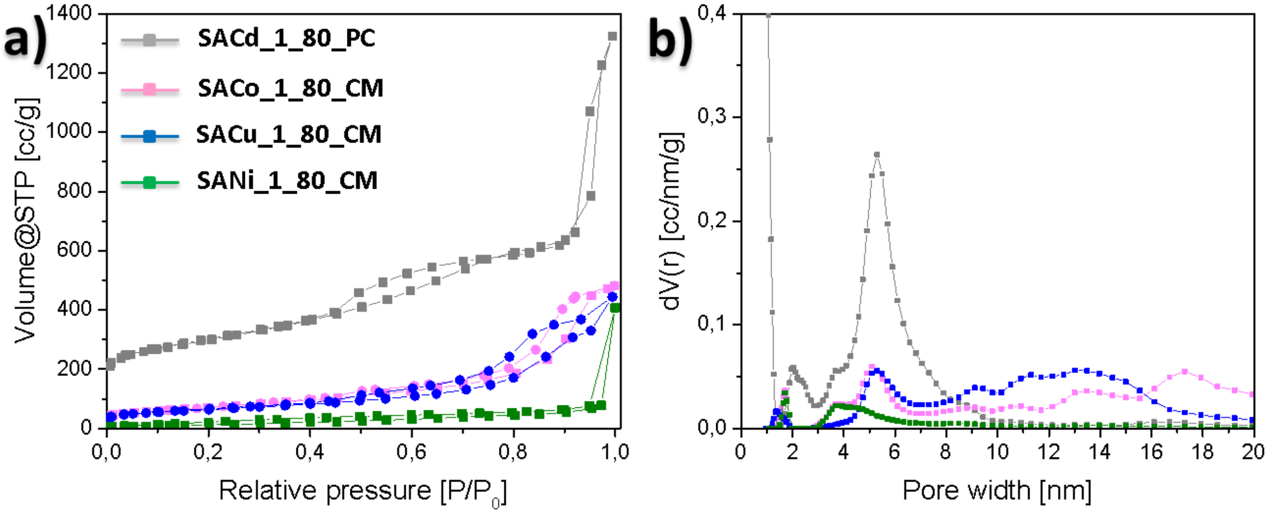

Figure 4.6 a) Nitrogen sorption isotherms of SACu_1_80_CM (blue), SANi_1_80_CM (green), SACo_1_80_CM (pink) and SACd_1_80_PC (grey). b) PSD of the corresponding materials calculated based on the NLDFT model for slit and cylindrical pores.

The corresponding PSD curves are presented in **Figure 4.6 b** and reflect well the results from the nitrogen sorption evaluations, i.e. the composites SACu_1_80_CM and SACo_1_80_CM exhibit a broad pore size distribution in the mesopores range whereby, SACd_1_80_PC reveals a bimodal PSD with peaks maxima around 5.4 and 1.2 nm.

Among these materials, the highest surface area and total pore volume of 1060 $m^2 g^{-1}$ and 2.05 $cm^3 g^{-1,}$, respectively, were obtained for the porous carbon SACd_1_80_PC (**Table 3**).

The above results clearly demonstrate that the pore structure and the accessible surface areas of the produced materials can be determined and tuned by the choice of the squarate-metal ion combination, as different complex structures and functionalities result from different squarate-metal ion coordination.

Table 3 Nitrogen sorption and elemental analysis data for the composites and carbons, respectively, derived from coordination complexes of squarate ions with Cu^{2+}, Ni^{2+}, Co^{2+} and Cd^{2+}, respectively .

Compound	**S_{BET} [m^2g^{-1}]**	**Pore volume [cm^3g^{-1}]**			**Elemental Analysis [wt %]**	
		Total	*Micro*	*Meso*	*C*	*H*
SACu_1_80_CM	226	0.7	0.01	0.06	7.02	0.8
SANi_1_80_CM	51	0.63	0.02	0.51	14.5	0.8
SACo_1_80_CM	286	0.88	0.13	0.75	17	1.0
SACd_1_80_PC	1060	2.05	0.46	1.59	86.4	1.1

4.4. **Carbon materials derived from croconate-zinc coordination complexes**

Herein, the concept of using coordination complexes as precursors for the synthesis of nanoporous carbon materials with pre-defined structural properties is extended to croconate-based complexes. In chapter 3, the complex CAZn_1_80, which is constituent of croconate ions coordinated to Zn^{2+}, was shown to yield crystalline particle possessing a 3D morphology of a distorted hexagonal prism. Direct carbonization of these mesocrystalline particles at 1000 °C for 1h in a nitrogen atmosphere yielded a porous carbon while preserving the intriguing 3D morphology of the pristine mesocrystals (**Figure 4.7**).

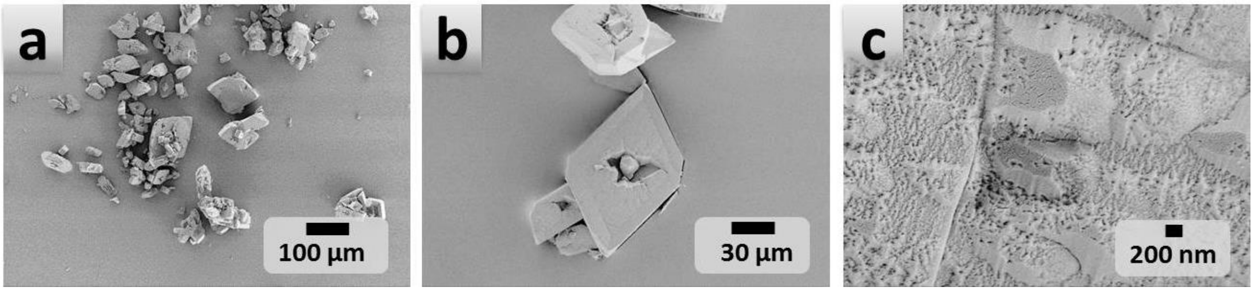

Figure 4.7 SEM micrographs of the carbons CAZn_1_80_PC which are derived from the complex CAZn_1_80.

TGA analysis reveals a multi-step degradation profile for the thermal transformation of the mesocrystals to the corresponding carbon (**Figure 4.8 a**). Here, the mass loss of ca. 21 % at 174 °C can be attributed to the loss of water, which is followed by a two-step release of CO_2 at 358 °C and around 500 °C with an associated mass loss of 16 % and 23 %, respectively. This can be attributed to the partial decomposition of the croconate units. The degradation step at 910 °C with a mass loss of ca. 29 % can be attributed to the release of Zn, which commonly boils at 907 °C, whereby the residual mass of ca. 11 % is considered to mainly be constituent of carbon.[179] This is supported by elemental analysis which reveals that the carbon CAZn_1_80_PC is composed of C (92.1 wt%), H (1.1 wt%) and O (3 wt%). The XRD pattern of the corresponding material (**Figure 4.8 b**) reveals a broad reflection signals at 2θ values of ca. 22 and 44°, which can be assigned to the (002) and (101) planes of a graphitic carbon with low structural ordering.

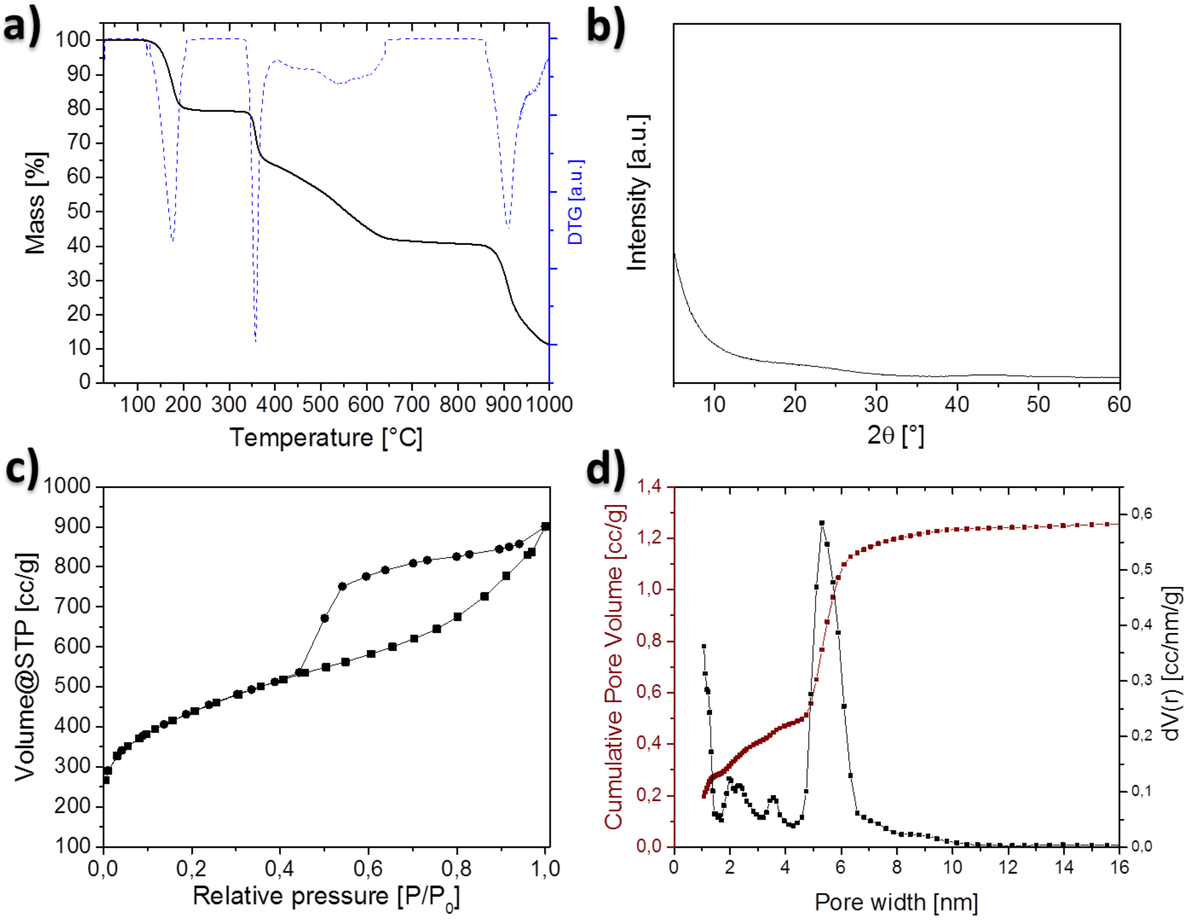

Figure 4.8 a) TGA and DTG curves of the complex CAZn_1_80 measured in nitrogen atmosphere at a heating rate of 10 °C min^{-1}, b) XRD diffractogram of the carbon CAZn_1_80_PC, c) nitrogen sorption isotherms of CAZn_1_80_PC, and d) PSD of the corresponding materials calculated based on the NLDFT model for slit and cylindrical pores.

Nitrogen sorption analysis of CAZn_1_80_PC reveals combined characteristics of type I and type IV isotherms with a steep uptake at low relative pressure area ($P/P_2 < 0.1$), followed by a type H4 hysteresis loop. This is suggestive of a well-developed hierarchical pore structure consisting of micro- and mesopores, whereby a high surface area and large total pore volume of 1557 m^2 g^{-1} and 1.4 cm^3 g^{-1}, respectively, were determined. The calculation of the pore size distribution was based on the NLDFT model, indicating the presence of nearly uniform mesopores of approximately 5.3 nm pore size along with micropores of 1 nm pore width. As shown herein, the concept of using predefined mesocrystalline microparticles to prepare hierarchical porous carbons is also applicable to croconate-based coordination compounds.

5. Applications of Composite and Carbon Materials derived from coordination complexes

5.1. Background and State-of-the-Art

In the preceding chapters, porous carbon materials obtained via heat treatment of squarate-zinc complexes (e.g. SAZn_1_4_PC) have been shown to possess a large BET surface area, a hierarchical pore structure, and intriguing 3D nanocube morphology. Furthermore, the material properties were shown to be easily tunable by the choice of the preparation conditions including the metal ion species, the organic ligand, the solvent, the molar ratio between the organic building units and the metal ion, and the crystal aging temperature. In general, hierarchically porous carbons with well-defined pore dimensions offer minimized diffusion distances by the macropores whereas the mesopores can provide large accessible surface area and minimized mass transport resistance. Owing to these structural features they are considered as material of choice in several energy and environment-based applications. In this context, they can serve as catalyst support, adsorbent, gas storage and electrode material for energy storage applications, among others.[56, 172, 173] Particularly for energy storage applications, a hierarchical pore structure with well-organized and interconnected pores of different pore types can be beneficial as it allows for improved specific capacitances and rate capabilities.[185, 186]

In general, supercapacitors, also called electrochemical capacitors or ultracapacitors, represent a promising class of electrochemical storage systems and are characterized by high power densities, fast charge and discharge rates with high degree of reversibility and long cycle life (> 100 000 cycles).[187-189] Compared to batteries, they possess lower energy densities (5-10 Wh kg) but outperform batteries in terms of high power performance, as depicted in the Ragone plot (**Figure 5.1**).[1].[190] Depending on the energy storage mechanism as well as the nature of the used active material, supercapacitors can be classified into several types of electrochemical capacitors including the electrical double layer capacitors (EDLC), pseudo-capacitors and hybrid capacitors.

Capacitance in EDLCs arises from the reversible adsorption of charge onto active materials which possess large accessible surface areas. Based on the model of Stern and Geary, a compact double layer of oppositely charged ions, called Stern-layer, is formed after applying a potential.[191] It is followed by a diffuse layer of randomly distributed electrolyte ions which accumulate to the electrode surface.[192] Pseudo-capacitors, also known as redox supercapacitors are based on fast and reversible faradaic processes at the interface between the electroactive electrode material and the electrolyte. Here, commonly used pseudo-capacitive materials are transition metal oxides (RuO_2, MnO_2, and V_2O_5), conducting polymers (e.g. polyaniline, polypyrrole, and derivatives of polythiophene) and heteroatom-containing carbons.[193] A hybrid capacitor combines a capacitive or pseudo-capacitive electrode with a battery electrode and thus benefits from both the high power density of the capacitor and high energy densities of the battery.

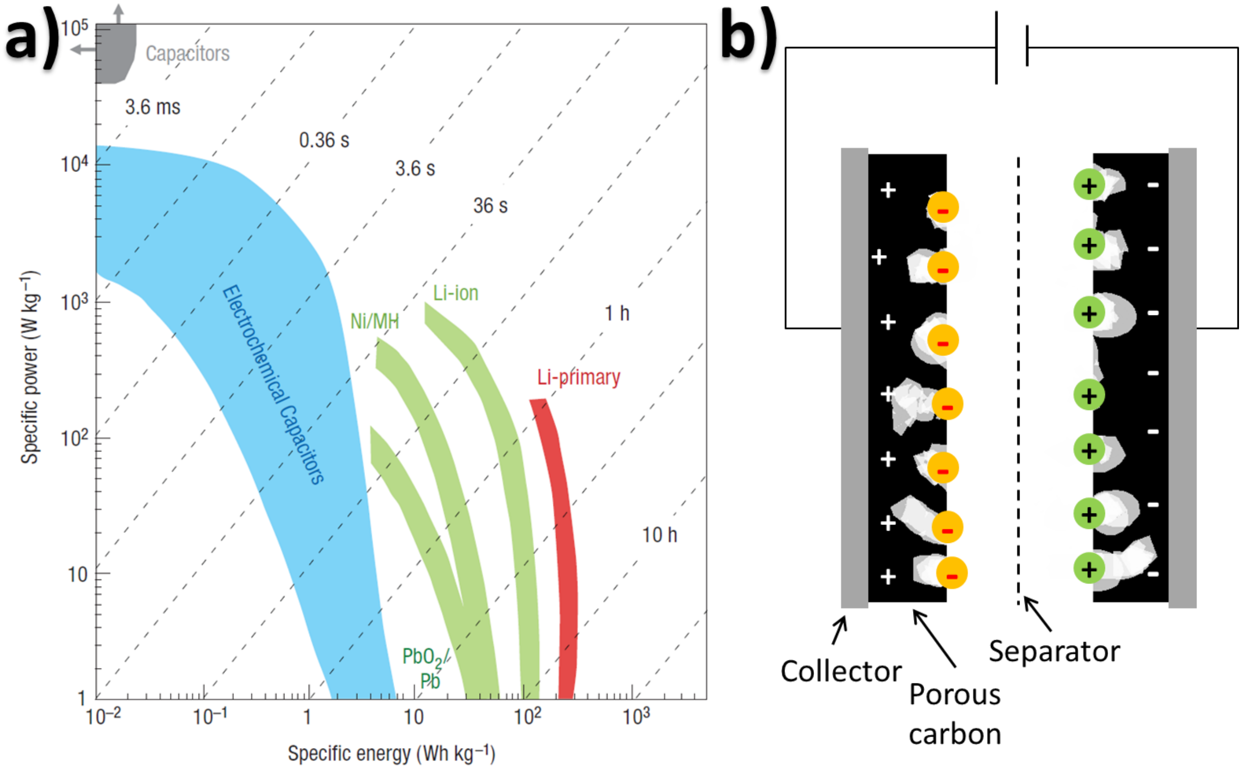

Figure 5.1 a) Ragone plot showing the specific power against the specific energy for various energy storage systems, adapted from Simon and Gogotsi[193], and b) schematic representation of an EDLC during capacitive charge.

In general, EDLCs can store much more energy (per unit mass or volume) compared to conventional capacitors. This can be attributed to the high surface-area electrode material that enables the storage of an increased amount of charge. Moreover, charge separation distances are decreased in the electrical double layer.[187] Among the several factors known to determine the electrochemical performance of a supercapacitor the properties of the electrode material are very crucial.[194]In this context, properties such as high conductivity, electrochemical stability, high temperature stability, high specific surface area, and tunable pore structures are beneficial to achieve high energy storage capacitances.[60, 195]

Porous carbon materials are also widely applied in catalysis, for instance as support material for the immobilization of catalytically active species such as metals, metal carbides and metal oxides, among others. [196, 197] Such composite catalysts exhibit unique catalytic activities resulting from the heterojunction between the immobilized metal species and the support material.[198, 199]

In heterogeneous catalysis, the catalyst and the reactants are basically in different phases. This facilitates the catalyst separation from a reaction mixture and therefore the recovery from expensive catalysts for instance by a facile filtration process. Owing to these points, heterogeneous catalysts are widely applied in the petrochemical industry and become more and more indispensable in bio-refinery applications.[200, 201] In the search for clean and efficient alternatives to conventional petroleum-based fuels in order to tackle environment pollution and global warming issues, DMF is considered to be a promising energy source.[202, 203] This is due to the numerous advantages that 2,5-dimethylfuran (DMF) bears: First, it can be produced effectively from lignocellulosic biomass via intermediates such as fructose and 5-hydroxyemthylfurfural (HMF).[204, 205] Moreover, DMF possesses intriguing physicochemical properties very similar to conventional fuel such as gasoline or diesel fuels and in some points it even outperforms them both. This makes DMF suitable for the effective combustion in internal combustion engines. In this context, DMF exhibits higher research octane number (RON= 119) which is higher than that of gasoline (RON= 90-100) while providing a high energy density (30 kJ cm^{-3}).[206] Compared to ethanol and n-butanol, which have been well investigated in recent years and belong to the first generation biofuels, DMF has lower water solubility and higher low heating value (33.7 MJ kg^{-1}) which is beneficial because it leads to reduced fuel consumption.[202] So far, conventional routes for the production of DMF involve the dehydration of hexose (e.g. fructose) to HMF over an acid catalyst (e.g. HCl, H_2SO_4, and H-form zeolites) (**Figure 5.2**).[207] Following selective hydrodeoxygenation of HMF to DMF employs Ni- or Ru-based catalysts in form of metal nanoparticles dispersed over a support material.[208]

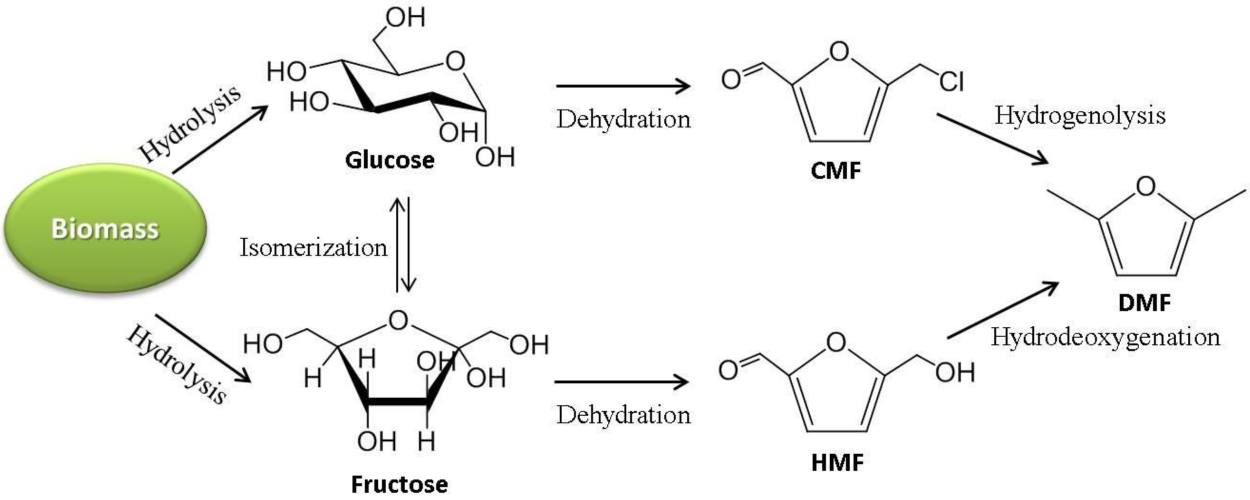

Figure 5.2 Schematic representation of the possible reaction pathways for the production of DMF from biomass.

The porous carbon cubes introduced in chapter 4 are equipped with advantageous properties such as a large surface area and a well-accessible 3D interconnected hierarchical pore structure, which make them promising for applications involving a material's surface and well-accessible pores. To demonstrate the benefits of these features, these hierarchically porous carbon materials are herein first applied as a high structural density electrode material for supercapacitor. This work is developed in conjunction with my colleague Thomas Berthold, whereby my contribution mainly focusses on the material synthesis and evaluation of the electrochemical data. In the second part of this chapter, the carbon is used as support material in order to immobilize nickel-nanoparticles (Ni-NPs). The resulting composite material is then employed as heterogeneous catalyst in the hydrodeoxygenation of HMF to DMF in a fixed-bed flow reactor and evaluated with respect to their column efficiency by conducting pressure drop studies. Alternatively, in a second approach, nickel-carbon (NiC) composites are prepared in a one-pot synthesis by the direct heat treatment of squarate-nickel mesocrystals. This part of the thesis is done in cooperation with the colleagues Max Braun and Marius Bäumel. Here, my own contribution is focused on the concept of a cube-shaped composite catalyst and the coupled advantages as packing material for flow systems, when compared to the standard agents explored by my colleagues.

5.2. **Electrochemical capacitors**

The use of commercial porous carbons in high-power energy storage devices is mostly limited by electrode kinetic problems which can be attributed to inner-pore ion-transport resistance resulting in poor rate performances.[185] For efficient energy storage performance, the carbon electrode material has to fulfill certain requirements in terms of high conductivity, a high surface area and well-accessible pores, among others.[209] In the preceding chapter, the porous carbon derived from squarate-zinc coordination complexes, named SAZn_1_80_PC, was shown to possess large and well-accessible surface areas, high total pore volumes, and a 3D hierarchically porous structure consisting of interconnected micro-, meso- and macropores. In order to elucidate the accessibility of the pores for electrolyte ions, SAZn_1_PC was tested as supercapacitor electrode material. Therefore, the capacitance behavior of the porous carbon was evaluated by means of cyclic voltammetry and charge-discharge measurements at various scan rates and current densities, respectively. A two-electrode setup was used for all measurements. The specific capacity C was calculated according to:

$$\boldsymbol{C = \frac{2}{\Delta V \cdot v \cdot m} \cdot \int I dV} \tag{5.1}$$

whereΔV (V) is the potential difference, v (V s^{-1}) is the scan rate, m (g) is the sample mass and I (A) the current.[190] The energy density E and specific power density P were calculated according to following equations:

$$\boldsymbol{E = \frac{1}{2} C (\Delta V)^2} \tag{5.2}$$

$$\boldsymbol{P = \frac{E}{t}} \tag{5.3}$$

where t (h) is the discharge time of the electrode. CV measurements were performed in 1 *M* H_2SO_4 at varying scan rates (5 – 200 mVs^{-1}). The respective CV curves are shown in **Figure** 5.3 **a** and reveal a quasi-rectangular profile at all the scan rates investigated. This shape is characteristic of double-layer capacitance with reversible adsorption/desorption of the electrolyte ions. In addition, the CV curves are distorted and exhibit slight humps around 0.4 V which hints to pseudo-capacitance contributions.[210] The observed Faradaic pseudo-capacitance can be attributed to the presence of oxygen functionalities (~3 wt.%) at the carbon's surface interacting with the electrolyte ions. Hence, the overall observed capacitance is considered to arise from the combination of pseudo-capacitance and double-layer capacitance.[211] Moreover, the CVs reveal increasing capacitive currents with increasing scan rates whereby the observed quasi-rectangular CV shape with typical Faradaic humps is maintained. This indicates a fast and effective ion transfer which is presumably facilitated by the 3D hierarchical porous structure of the electrode material. In general, a 3D hierarchically porous structure is desirable because it facilitates ion transportation by using the macropores as ion-buffering reservoirs. Thus, diffusion pathways are shortened and the inner-pore resistance is minimized leading to fast ions transfers. Further insights into the capacitive behavior of SAZn_1_80_PC were obtained by galvanostatic charge/discharge measurements carried out at different current densities (2-30 mA cm^{-2}). The corresponding charge/discharge profiles are shown in **Figure 5.3 b** and present a quasi-linear triangular shape with a slight distortion. This can be related to the aforementioned synergistic interaction between double-layer capacitance and pseudo-capacitance, which is consistent with the evaluation of the CV curves.[212] **Figure 5.3 c** depicts the dependence of the specific capacitance of the electrode from the scan rates. The porous carbon SAZn_1_80_PC exhibited a specific capacitance of 133 F g^{-1} at the lowest scan rate (i.e. 5 mV s^{-1}), whereby 67% of its specific capacitance were retained upon increasing the scan rate to 200 mv s^{-1} (89 F g^{-1}). This result demonstrates the effective rate performance which is provided by the 3D hierarchical porous structure of SAZn_1_80_PC. The respective Ragone plot is presented in **Figure 5.3 d**. The storage energy as well as power density were calculated as 2.31 Wh kg^{-1} and 3358 W kg^{-1}, respectively, at a current density of 100 mA cm^{-2}. In general, SAZn_1_80_PC showed superior electrochemical performance compared to commercial activated carbons with a comparable surface area measured under similar conditions.[213] This can be attributed to the well-organized and accessible hierarchical pore structure of the material allowing for short diffusion paths with minimized ion-transport resistance.

The herein presented preliminary results have shown that carbonaceous materials derived from squarate-zinc coordination complexes are promising candidates to be used as electrode material to store energy at high scan rates in supercapacitor applications.

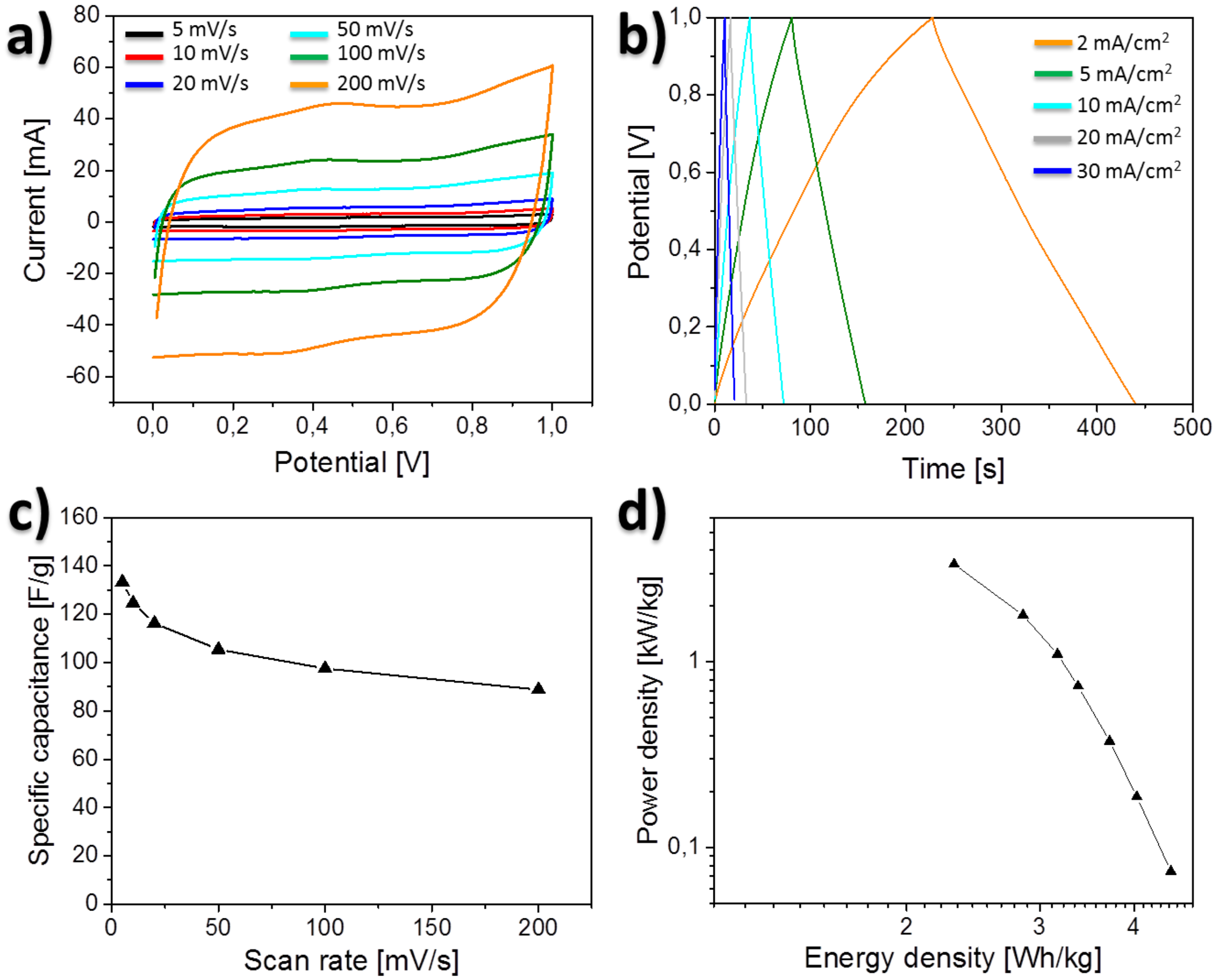

Figure 5.3 Electrochemical performance of SAZn_1_80_PC in 1 *M* H_2SO_4 with a) CV curves at varying scan rates, b) and galvanostatic charge/discharge curves at varying current densities, c) specific capacitances at different scan rates, and d) Ragone plot of the system. Reproduced from Mani *et al.* with the permission from Wiley.[47]

5.3. **Heterogeneous Catalysis**

Most major processes in the chemical industries such as the production of ammonia, ethanol, and the catalytic cracking of gas oil, among others, are based on heterogeneous chemical reactions.[214] Here, the catalyst increases the rate of reaction by decreasing the activation energy barrier required for the conversion of the educts and, furthermore, allows for better control of the selectivity. Besides the right choice of catalyst, the right choice of reactor type is also crucial.[215] Among the various reactor designs used in industry, so-called fixed-bed reactors are very auspicious as they enable large-scale productions in a continuous flow while ensuring efficient temperature control and intensive mixing of the reactants.[216, 217] Furthermore, operation costs are minimized and high conversion rates per unit mass of catalyst can be easily achieved.[218] However, a major drawback is the difficulty to pack the reactor column in an efficient manner in order to minimize the pressure drop. This in turn significantly affects the reactor performance in terms of diffusion and conversion efficiency and thus also affects the costs. Therefore, efficient and uniform packing of the fixed bed reactor is crucial and requires careful design of the catalyst.[219] In industry and on the larger scale, uniform packing is alternatively realized by pressing the catalyst material to regular structured pellets. However, pellets have the disadvantage of becoming brittle and fail over time when subjected to stress.[220] Moreover, they possess very low surface areas ($<150\ m^2g^{-1}$) compared to conventional lab-scale powder catalyst ($<1000\ m^2g^{-1}$) and hence lead to lower catalytic activity.[221, 222] As for the lab scale much smaller reactor dimensions are used, a careful and controlled design of the catalyst structure at the micrometer scale is crucial. This offers the benefit of combining the advantages of pelletized catalysts with characteristics of powder catalysts, i.e. a high surface area, reduced ratio of catalyst mass to reactor volume as well as minimized pressure drop throughout the reactor bed. This was recently targeted by Orrego-Romero *et al.* by synthesizing a Cu-Ni bimetallic catalyst supported on pellets of activated carbon.[223] However, this process required considerable amounts of binder materials to maintain the compressed state. This can be detrimental because the interactions between the binder and the catalyst may affect the catalytic performance. Moreover, the procedure required numerous preparation steps including the synthesis of the porous carbon, the pelletizing step, impregnation with a solution of the metal salts, and a washing step which in total make this process laborious, time- and energy-consuming.

The previously introduced carbon cubes provide a very large surface area, well-accessible 3D interconnected hierarchical pore structure, and a uniformly shaped and micrometer-sized cube morphology. The preparation approach holds the advantage that the materials' properties can be easily adjusted by the selection of the synthesis parameters and the approach does not require any additional hard- and soft templates or binders to maintain and stabilize the cube shape. Owing to these features, they can be used for the synthesis of heterogeneous catalysts, i.e. as support material to immobilize metal nanoparticles. In the concept developed herein (**Figure 5.4 b**), efficient and uniform packing of the fixed-bed reactor along with minimized pressure drop is expected due to the special cube morphology as well as the uniform size of the composite catalyst. In contrast, packing the fixed-bed reactor with an irregular shaped and sized catalyst material, as schematically illustrated in **Figure 5.4 a** is expected to lead to a high pressure drop throughout the reactor.

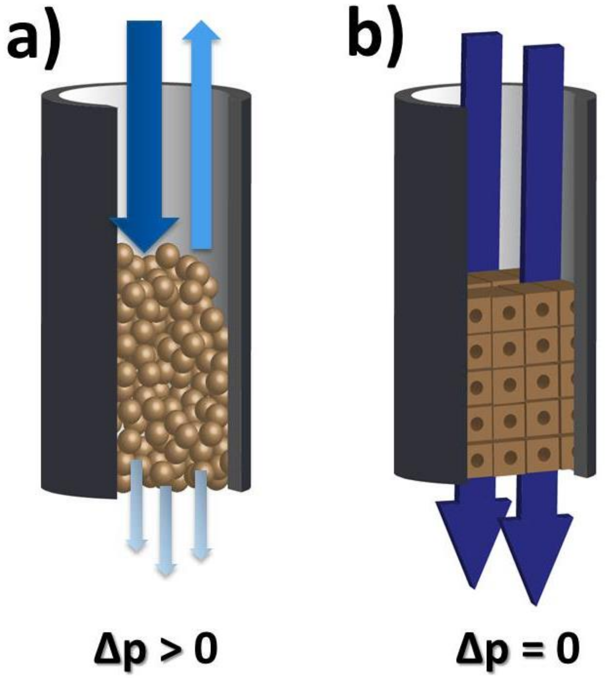

Figure 5.4 Schematic representation of a fixed-bed reactor packed with a) spherical particles of different sizes and b) uniformly sized cube shaped particles. The packing in (a) leads to a high pressure drop (Δp) throughout the packed reactor, whereas in (b) no significant pressure drop is expected.

In the following, nickel-carbon (NiC) composites are prepared via two different preparation approaches.

- In the first approach, the composite catalyst is synthesized via an impregnation method. For the support material, SAZn_1_4 crystals are heat treated to prepare hierarchically porous carbon nanocubes. They are further mixed with a nickel salt solution and subsequently reduced in H_2 environment.
- The second method involves the direct, one-pot synthesis of mesocrystals based on squarate-nickel (SANi) coordination complexes. Here, properties of the desired product can be altered by careful choice of the synthesis conditions. After heat treatment in a N_2 atmosphere, a regular structured carbonaceous material with incorporated nickel nanoparticles is obtained whereby no additional metal reduction step is required.

The resulting composite materials are then employed as heterogeneous catalysts in the hydrogenation of HMF to DMF in a fixed-bed flow reactor and further evaluated with respect to their column efficiency by conducting pressure drop studies.

5.3.1. Synthesis of NiC composite catalyst via an impregnation approach

A composite material (NiC) is prepared in a multi-step approach by immobilizing nickel nanoparticles (Ni-NPs) onto a hierarchically porous carbon support. The support material (SAZn_PC) is obtained as before by heat treatment of squarate-based nanocrystals in a nitrogen atmosphere at 900 °C followed by washing with a 1 *M* HCl solution as well as H_2O. The mesocrystalline carbon precursor in turn is synthesized by preparing squarate-zinc complexes in a molar ratio of 1:1 at 5 °C overnight. The carbon support (SAZn_PC) is then decorated with Ni-NPs by incipient wetness impregnation with an aqueous solution of $Ni(NO_3)_2\,6(H_2O)$. Subsequent treatment in a H_2/Ar atmosphere at 475 °C finally yields the composite material denoted as Ni@SAZn_PC, herein.

As already discussed in chapter 4, the SAZn_PC particles possess an intriguing 3D cube morphology inherited from the precursor mesocrystalls and an average particle size of. 24 µm in diameter. SEM micrographs of the composite Ni@SAZn_PC (**Figure 5.5**) reveal that the characteristics of the precursors i.e. nanocube morphology and uniform particle size could be maintained throughout the impregnation and Ni-reduction approach.

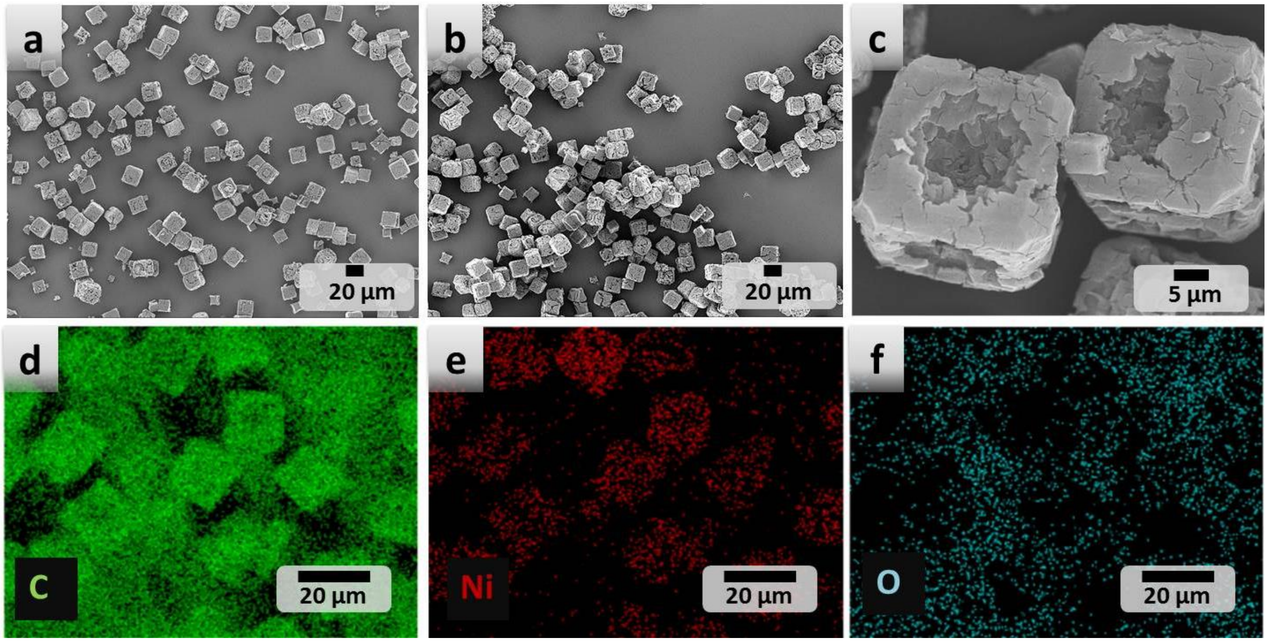

Figure 5.5 SEM micrographs of a) the porous carbon support SAZn_PC and b,c) the composite material Ni@SAZn_PC. EDX elemental mapping of Ni@SAZn_PC showing d) carbon, e) nitrogen and f) oxygen. Reproduced from Mani *et al.* with the permission from Wiley.[224]

Considering that the materials are subjected to high temperatures and have to withstand a multi-step procedure, involving the repeated transfer from one reaction container to another, those observations point to a good stability of the prepared materials. EDX analysis was performed to elucidate the elemental distribution within the NiC composites. The respective elemental mapping (**Figure 5.5 d-f**) reveals that the particles are mainly constituent by C, Ni, and O, and furthermore confirms the homogenous loading of Ni onto the carbon framework. From elemental analysis and ICP_OES, the Ni-loading is determined to be 15 wt%. The homogenous dispersion of Ni-NPs onto the carbon framework is further supported by evaluation of the corresponding TEM images (**Figure 5.6**) which reveal that the Ni-NPs exhibit an average size of 12 nm.

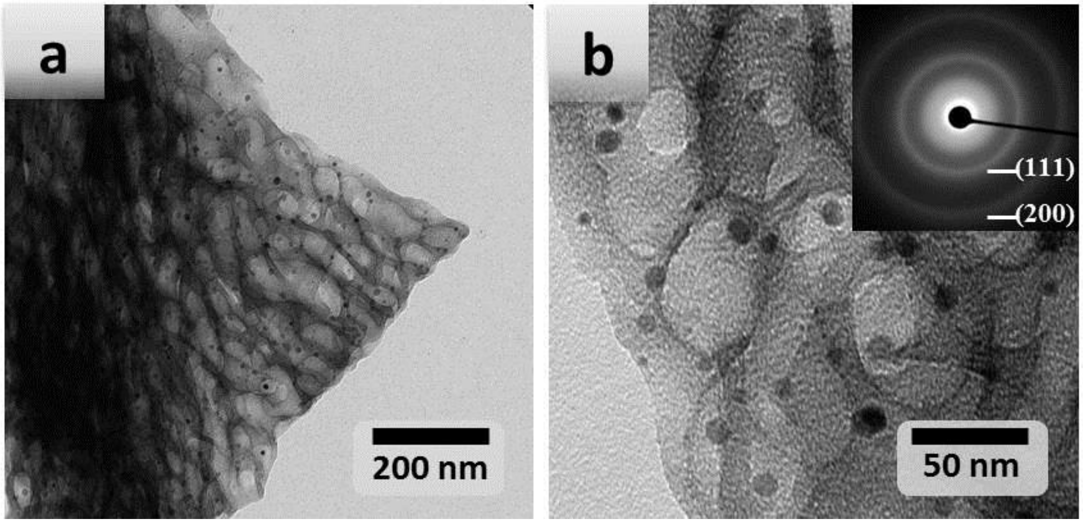

Figure 5.6 a,b) TEM micrographs of the composite Ni@SAZn_PC. The inset in (b) shows the SAED pattern of the Ni-NPs. Reproduced from Mani *et al.* with the permission from Wiley.[224]

XRD analyses of the samples allow for more insights into the crystalline nature of the immobilized Ni species. The diffractogram of SAZn_PC shows two broad reflections at 2θ values around 23.6° and 43.4° which can be assigned to the (002) and (101) planes of a turbostratic form of carbon, respectively. Furthermore, the pattern reveals two narrow reflections at $2\theta = 44.5°$ and 52° assignable to the (111) and (200) crystalline planes of metallic Ni, respectively. The average crystalline domain size of the Ni° particles is determined from the (111) reflection using the Debye-Scherrer formula and accounts for 11.5 nm, which is in close agreement with the TEM evaluation. All the observations made so far point to both the successful immobilization of the Ni species and their reduction to Ni^0.

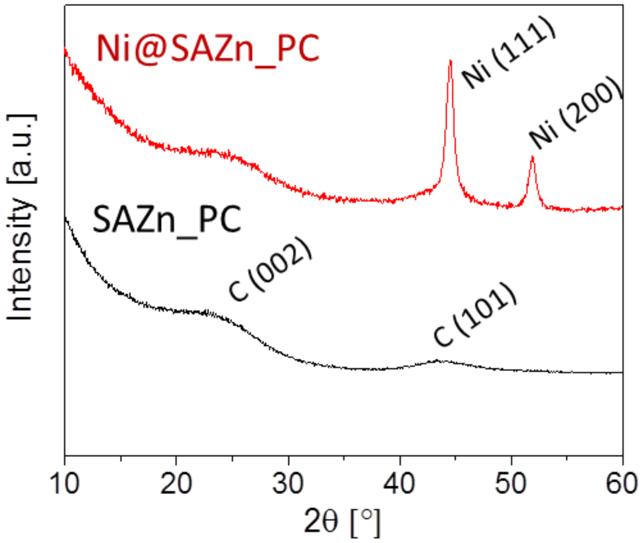

Figure 5.7 XRD patterns of the carbon support SAZn_PC (black line), and the corresponding composite Ni@SAZn_PC (red line).

The pore structure of the prepared materials was evaluated by nitrogen sorption analysis. As discussed before, the carbon support SAZn_PC possesses a large surface area of 1423 $m^2\ g^{-1}$ and a high total pore volume of 1.67 $cm^3\ g^{-1}$. The corresponding sorption isotherm exhibits combined characteristics of type I and IV indicating both micro- and mesopores contributions. The surface area and the total pore volume decrease slightly upon decoration with Ni-NPs to 1291 $m^2\ g^{-1}$ and 1.55 $cm^3\ g^{-1}$, respectively. However, the isotherm shape of the composite Ni@SAZn_PC is very similar to that of SAZn_PC and in both cases the hysteresis closes at a relative pressure of $P/P_0 = 0.5$. This rules out a major pore blocking effect as major cause for the modest loose of porosity. Therefore, the decreased surface area can be attributed to the increased averaged material density upon loading with Ni-NPs. In addition, both materials display similar PSD curves showing meso- and micropores with diameters of 5.7 nm and 1 nm, respectively. Bringing all results together, it is strongly suggested that the hierarchical pore structure of SAZn_PC comprised of micro-, meso- and macropores is maintained throughout the whole preparation procedure and that all carbon pores remain well accessible for the reactants.

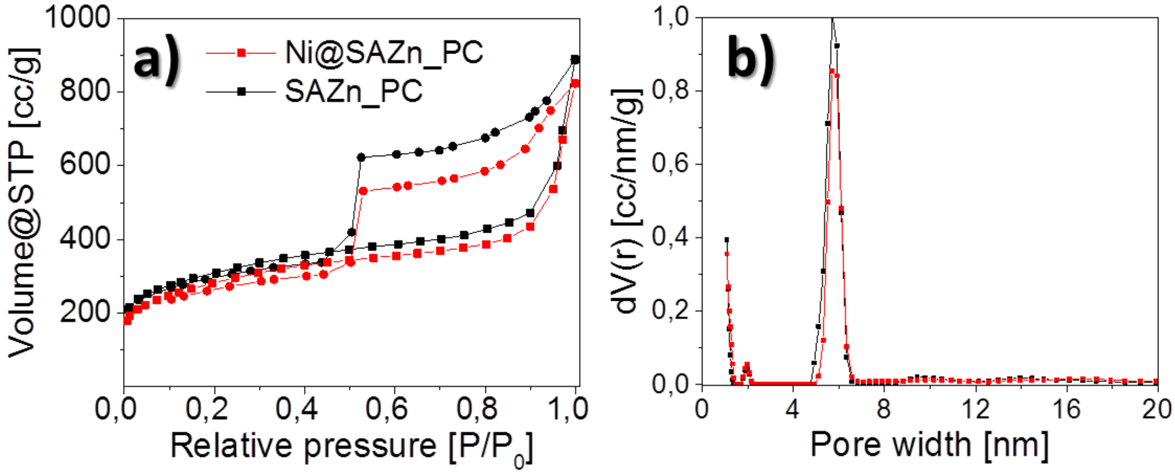

Figure 5.8 a) Nitrogen sorption isotherms of the carbon support SAZn_PC (black line) and the composite Ni@SAZn_PC (red line). b) The corresponding PSD curves.

5.3.2. Synthesis of NiC composite catalyst via an one-pot synthesis approach based on nickel-squarate complexes

In order to increase the volumetric density of the nickel in the material, mesocrystals based on nickel-squarate complexes (SANi_1_80) were prepared via a one-pot synthesis approach by mixing aqueous solutions of squaric acid and Ni $(CH_3COO)_2\ 4H_2O$ in a molar ratio of 1:1 at 80 °C for 1h. Heat treatment of this crystalline precursor at 900 °C in a N_2 atmosphere yielded the NiC composite SANi_CM. As already discussed in chapter 3 and shown in **Figure 5.5**, the coordination complexes of nickel and squarate ions give rise to mesocrystals (SANi_1_80) which possess a 3D cube morphology, whereby the particles measure 12 µm in average edge length. Compared to the zinc-squarate based mesocrystals SAZn_1_80, the cubes of SANi_1_80 are smaller and the material exhibits a broader particle size distribution.

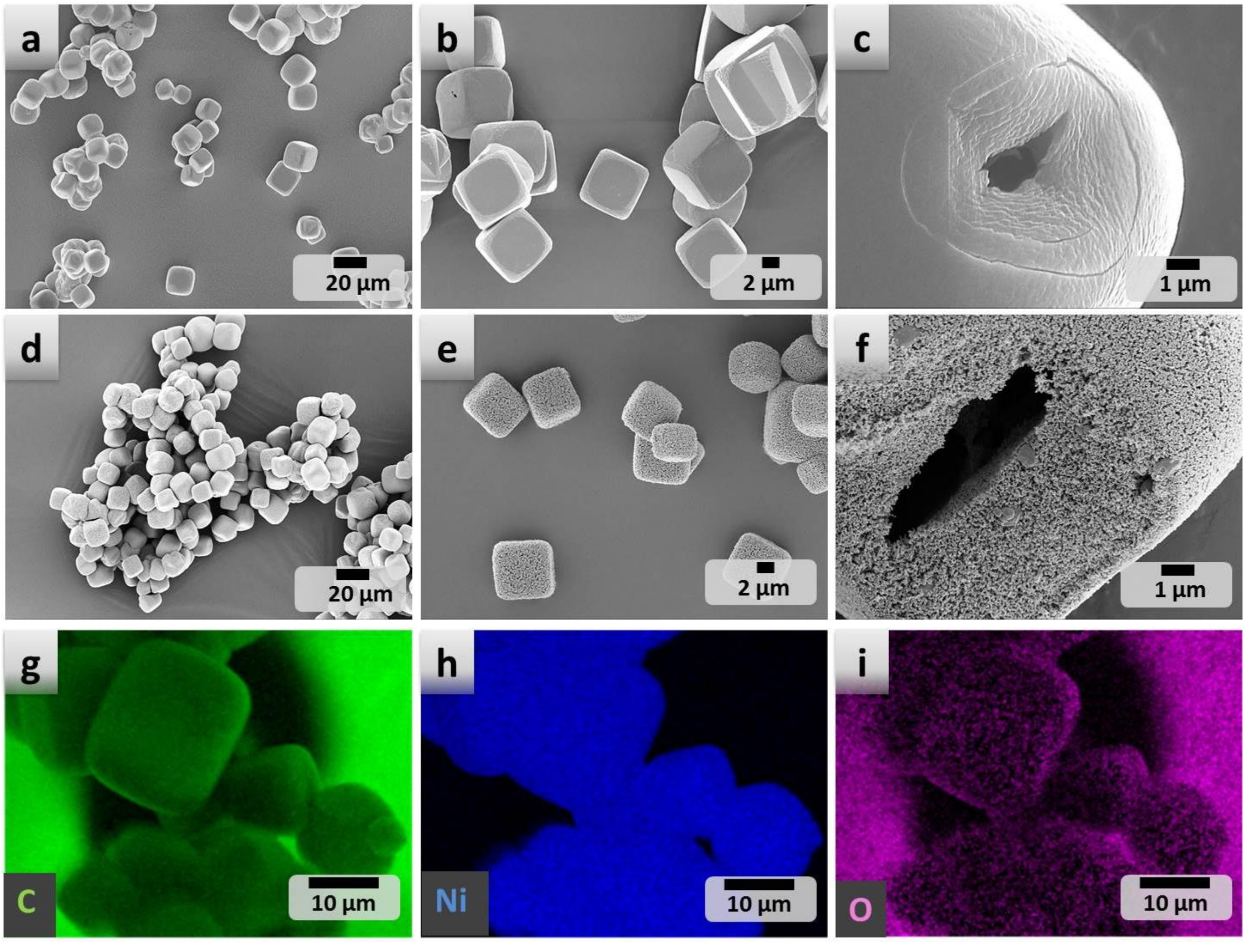

Figure 5.9 a-c) SEM micrographs of the coordination complex SANi_1_80, d-f) the corresponding composite SANi_CM obtained after heat treatment, and (g-i) EDX elemental mapping of SANi_CM showing with carbon (g), nickel (h), and oxygen (i).

After the heat treatment, the particle size of the composite SANi_CM decreased slightly to approx. 9 µm in average edge length and the nitrogen sorption analysis revealed a nonporous material with an external surface area of approximately 51 m^2 g^{-1}.(**Figure 4.6**, chapter 4.3). It is to be noted, that the 3D cube morphology of the pristine mesocrystalline SANi_1_80 could be preserved throughout the heat treatment process. Form the elemental mapping images (**Figure** 5.9 **g-i**) it can be stated that the cubes of the composite SANi_1_CM are mainly constituted of carbon, oxygen, and nickel nanoparticles distributed all over the nanocubes. ICP_OES data revealed an average Ni content of approximately 84 wt%.

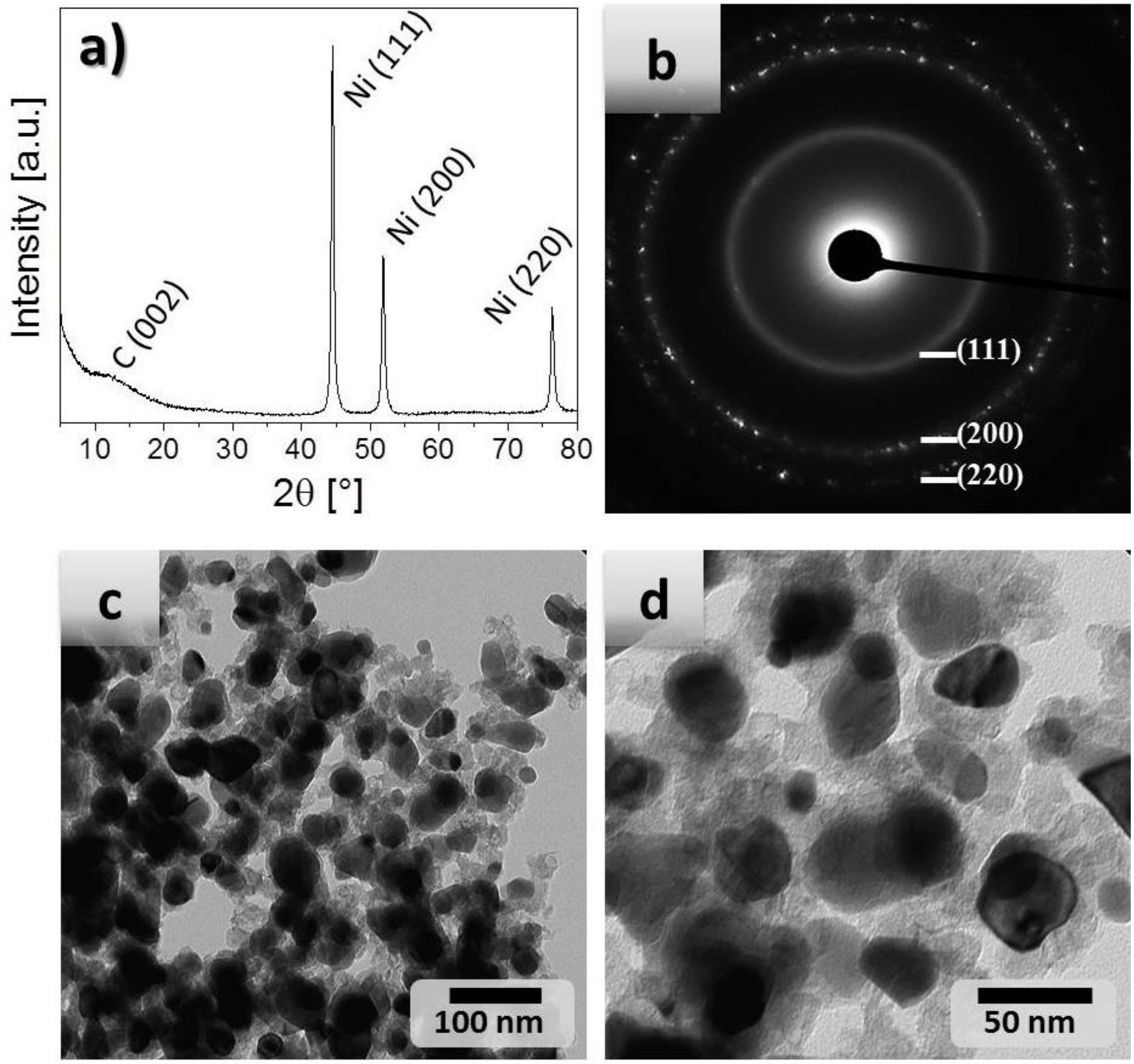

Figure 5.10 a) XRD diffractogram of the composite SANi_CM, (b) the corresponding SAED pattern, (c,d) the corresponding TEM micrographs.

The corresponding XRD pattern (**Figure 5.10 a**) reveals sharp and intense reflections at 2θ= 44.5, 51.8, and 76.4° characteristic of the (111), (200) and (220) planes of the face-centered-cubic structure of metallic Ni. The average crystalline domain size of the Ni-NPs determined from the (111) reflection using the Debye-Scherrer formula accounts for 26 nm, which is double the size of the Ni crystallites in Ni@SAZn_PC (11.5 nm).

It is suggested that during the heat treatment process NiO nanoparticles are formed and subsequently undergo carbothermal reduction to form the corresponding metallic Ni nanoparticles. The as-formed Ni nanoparticles are mixed that tightly with the carbon framework that they could not be removed during the acid washing process. Although the XRD diffractogram does not reveal peaks characteristic of crystalline NiO, it cannot be ruled out that the metal-oxide nanoparticles are present in their amorphous form considering that EDX elemental mapping revealed the presence of O atoms. The corresponding TEM images show large nanoparticle agglomerates enclosed by the carbon phase (**Figure 5.10 c,d**).

5.3.3. Catalytic performance of the NiC composites

Efficient packing of a fixed-bed reactor, i.e. in such a manner that the pressure drop over the packed reactor is minimized, is essential because it impacts mass and heat transfer and hence determines selectivity and conversion to the desired product.[219] In industry, this is achieved by using pellets, which are commonly in the size range of several millimeters. In contrast, lab-scale powder catalysts possess particles in the micro-size range and much larger surface areas hence allowing for higher catalytic activities compared to the pellet-catalysts.[221, 222] In general, the main factors determining the performance of a packed column are the column efficiency and the pressure drop. The latter significantly depends on the structure and geometrical dimensions of the catalyst, whereby uniformly structured and sized catalysts with an open structure are reported to be more beneficial.[225] The prepared NiC composites, Ni@SAZn_PC and SAZn_CM possess a regularly shaped nanocube morphology and hence are promising to tackle the pressure drop issue within a fixed-bed flow reactor. Solids decorated with Ni-NPs are known to be promising catalysts for hydrogenation reactions among other due to their high abundance and low cost when compared to noble metals such as Pt, PD, Ru, etc.[202, 226, 227]

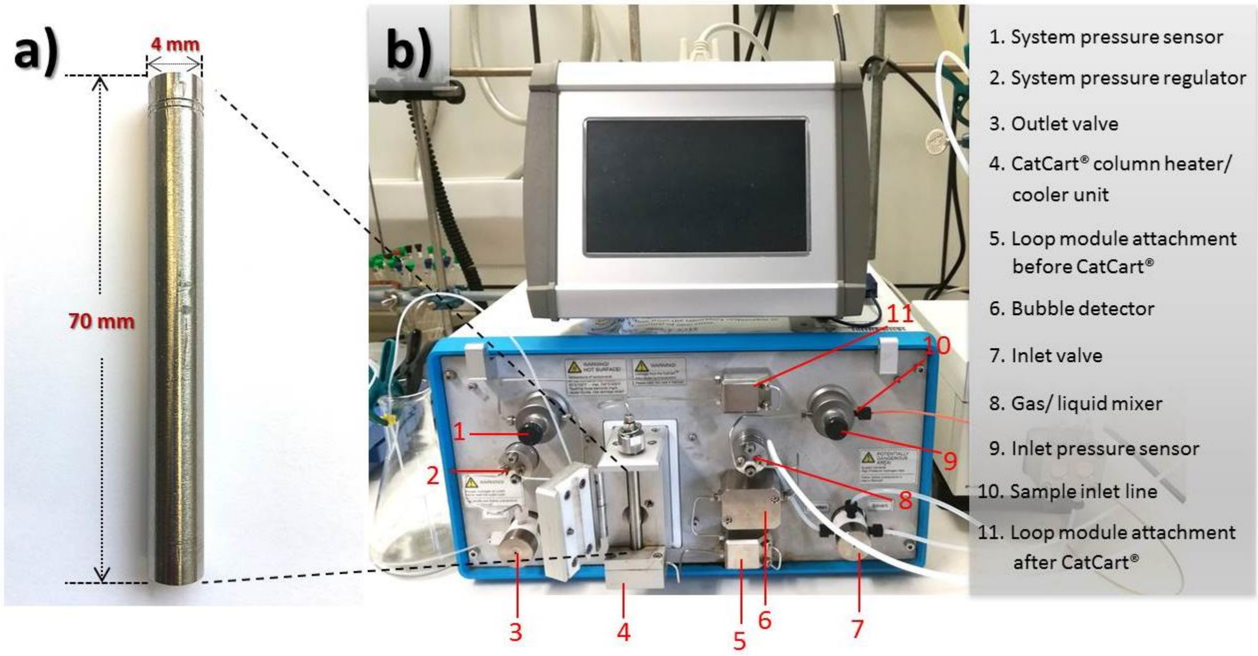

Figure 5.11 a) Catalyst cartridge column with the respective dimensions, b) set-up of the H-Cube Pro^{TM} flow reactor.

In the following, catalytic studies with the NiC composites as catalyst were carried out for the selective conversion of HMF to DMF using a lab-scale hydrogenation continuous flow reactor system (H-Cube Pro^{TM}, **Figure 5.11 b**). For that, a 70 mm (4 mm Ø) catalyst cartridge (**Figure** 5.11 **a**) was packed with Ni@ SAZn_PC (159 mg, 0.04 mmol) and SANi_CM (284 mg, 4.06 mmol Ni), respectively. In order to evaluate the pressure drop, (Δp) i.e. the difference between the inlet pressure (P_{inlet}) and the pressure adjusted at the outlet (P_{set}), the reaction was carried out at different conditions and Δp was monitored in dependence of the temperature (T) and the reactants flow rate (F) (**Table** 4). Thereby, an ideal column packing is expected to exhibit a negligible pressure drop ($\Delta p \approx 0$ bar) and high yields of DMF production. Pressure studies with the catalyst SANi_CM revealed a back pressure of over 90 bars at the set conditions, which is comparable to pressure drops reported for fixed-bed flow reactors packed with fine powder catalysts.[228] In contrast, Ni@SAZn_PC exhibited a negligible back pressure (Δp = 0-1 bar) at all conditions, whereby the highest back pressure (3 - 4 bar) was detected at the highest flow rate of 2 ml min^{-1} at 150 °C and 6 bar. Those low back pressures can be attributed to a combination of high pore volume, well-accessible pores and a hierarchical pore structure. By comparing the results obtained with Ni@SAZn_PC and SANi_CM, the big differences in the observed pressure drops are attributed to several factors including the total pore volume, the pore accessibility, the particles size as well as particle size distribution. In this context, a high total pore volume, good pore accessibility and narrow particle size distribution are shown to result in negligible pressure drops over the packed reactor.

Table 4 Pressure studies on Ni@SAZn_PC (159 mg, 15 wt% Ni) at different conditions in the flow system without using hydrogen.

T [°C]	**P_{set} [bar]**	**F [ml min^{-1}]**	**P_{inlet} [bar]**	**Δp [bar]**
60	6	0.50	6-7	0-1
100	6	0.50	6-7	0-1
120	6	0.50	6	0
140	6	0.50	6-7	0-1
150	6	0.50	6-7	0-1
150	**6**	0.50	6-7	0-1
150	**10**	0.50	10-11	0-1
150	**14**	0.50	14-15	0-1
150	**18**	0.50	18-19	0-1
150	**30**	0.50	30	0
150	6	**0.25**	6	0
150	6	**0.50**	6-7	0-1
150	6	**0.75**	6-7	0-1
150	6	**1.00**	7	1
150	6	**2.00**	9-10	3-4

P_{inlet} = pressure at the entrance of the column; P_{set} = pressure adjusted for the column; all measurements were performed using ethanol.

Besides the pressure drop, the column efficiency is a further important factor to evaluate the quality of a packed column. It is strongly affected by the liquid distribution and redistribution within the packed bed and provides insights into the mass transfer efficiency.[229] A commonly applied concept for the evaluation of the column efficiency includes the model of the theoretical plate number N, which depends not only on the materials properties but also the column dimensions.[230] Here, high *N* values can be associated with an intimate contact between the fluids and the catalyst and hence relates to high column efficiencies. However, for better efficiency comparison between different columns the height equivalent to a theoretical plate (*H*) is mostly used. *H* is inversely proportional to *N* i.e. the more plates a column of a definite length *L* has, the thinner are the plates and the smaller is *H*.[231] They are calculated from the retention time of toluene through the packed column using the following equations:[232]

$$N = 5.545 \times \left(\frac{t_R}{\text{FWHM}}\right)^2 \quad (5.4)$$

$$H = {}^{L}/_{N} \quad (5.5)$$

where t_R is the retention time of toluene, 5.545 represents the retention factor, FWHM is the peak full width at half maximum and L is the length of column in mm.

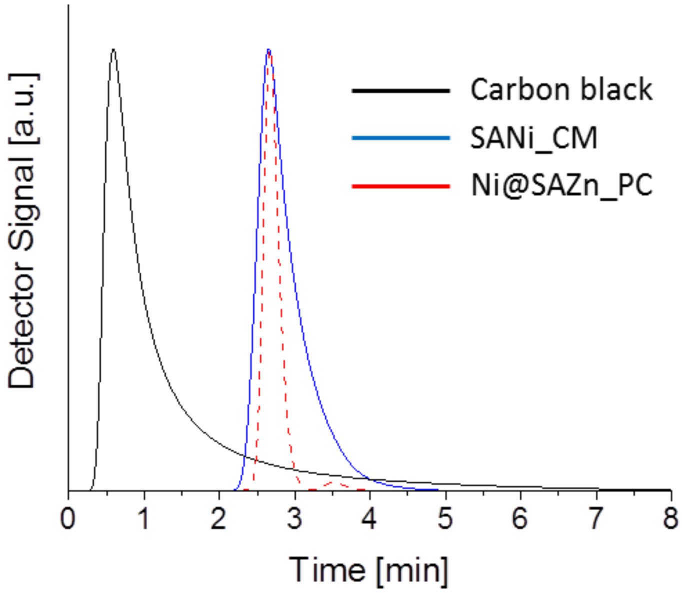

Figure 5.12 Chromatogram of toluene in a column packed with carbon black (black solid line), SANi_CM (blue solid line) and Ni@SAZn_PC (red dashed line).

As can be seen from the respective chromatograms (**Figure 5.12),** both investigated composite catalysts, Ni@SAZn_PC and SANi_CM, exhibit respective peaks at the same retention time (2.7 min) but the peaks differ in their profile. While Ni@SAZn_PC presents a narrow Gaussian peak, SANi_CM reveals a broad asymmetric peak with tailing behavior. Peak tailing can be attributed to an ineffective column packing, adsorptive effects of the packing material and/or dead-volume in the column. Consequently, Ni@SAZn_PC shows superior column performance and efficiency than SANi_CM in terms of higher plate numbers *N* and lower plate height *H*, as presented in **Table 5**. However, SANi_CM exhibits *N* values which are orders of magnitude higher than carbon black, which is a randomly structured fine powder material. This demonstrates that the shape of the catalyst material significantly affects the column efficiency and as shown in this case, the cube morphology is more beneficial. Nonetheless, the particle size as well as particle size distribution of the packing material are also shown to be crucial parameters which need to be considered when designing a packed column. These initial tests support the theory that the herein presented composite cubes are superior to amorphous fine powders as packing material in a flow reactor.

Table 5 Nitrogen sorption data and chromatographic studies of the packed column.

Packing	**S_{BET} [m^2 g^{-1}]**	**PV_{total} [cm^3 g^{-1}]**	***t [min]***	***N***	***H* [mm]**
Ni@SAZn_PC	1291	1.55	2.7	751	0.008
SANi_CM	51.4	0.63	2.7	166	0.036
Carbon Black	280	1.02	0.6	8	0.75

S_{BET} = surface area; PVtotal = total pore volume, t = column residence time; *N* = number of theoretical plates; *H* = height equivalent to one theoretical plate.

From the chromatographic studies (**Table 5**) the two types of NiC composites revealed similar residence times. In general, the longer educts remain in a reactor the more intimate is the contact between the substrates and the packed catalyst and the higher are the conversions. This conversion-residence time relationship is shown exemplarily for Ni@SAZn_PC as it is used as catalyst for the selective conversion of HMF to DMF (**Figure 5.13**). Here, the full conversion of HMF was observed at a flow rate of 0.25 mL min^{-1} corresponding to a residence time of 3.2 minutes.

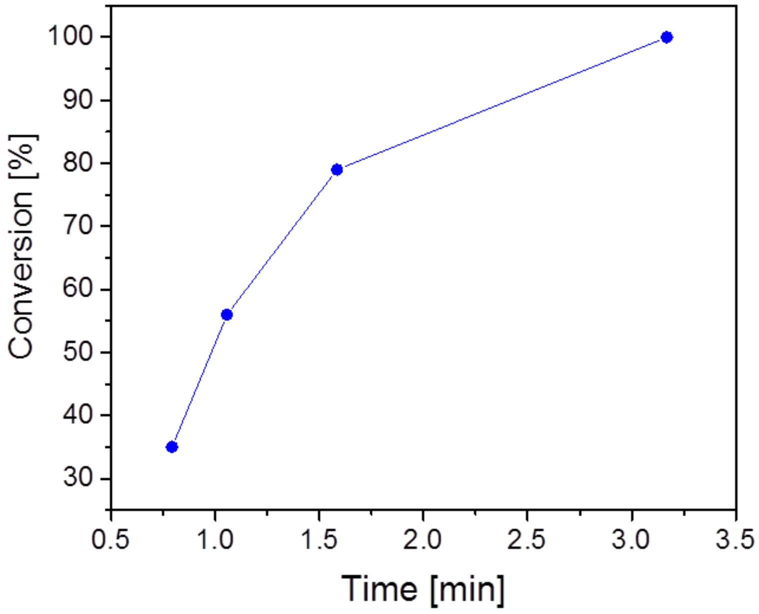

Figure 5.13 HMF conversion over residence time at 150 °C and 6 bar using Ni@SAZn_PC as catalyst.

At these conditions, only 41 % DMF yield was achieved, despite the full conversion of HMF. With increasing flow rate (1 mL min^{-1}) both the DMF yield and the HMF conversion decreased owing to the reduced residence time of the substrates in the reactor (**Table 6**). Possible intermediates or by-products that can be produced in the course of the HMF conversion to DMF (e.g. DHMF, 5-MF, MFA as well as DMTHF, 2,5-hexanediol and 2,5-hexanedione, respectively) are schematically depicted in **Figure 5.14** .

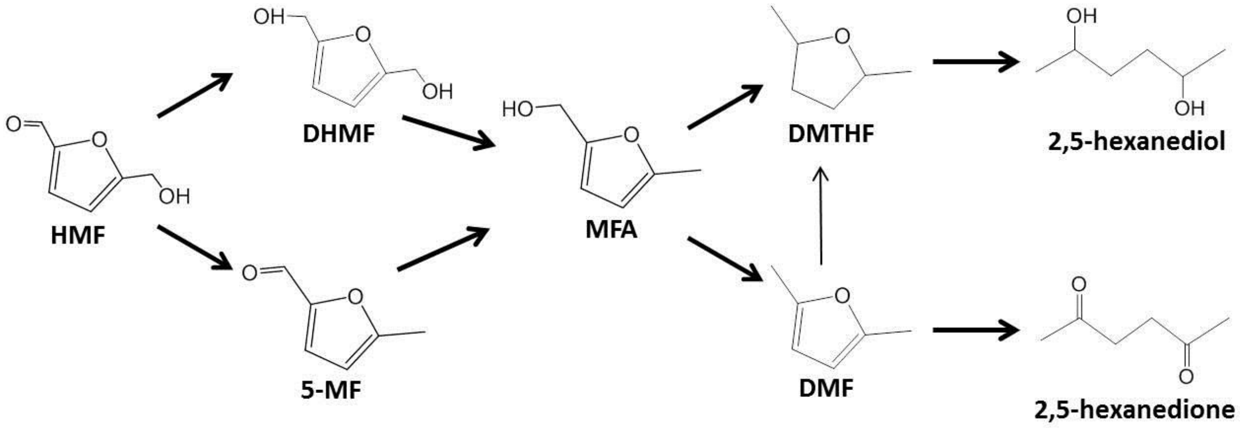

Figure 5.14 Proposed reaction path for the selective hydrodeoxygenation reaction of HMF.

Gas chromatrography- mass spectrometry (GC-MS) studies (**Figure S 15**) revealed the presence of 2,5-hexanediol at a flow rate of 0.25 mL min^{-1}. This hints to the fact that HMF was completely converted to DMF, which in turn was further reduced to DMTHF and then reacted to 2,5-hexanediol by furan ring opening. However, the carbon balance of the detected molecules did not reach 100 %, which may be attributed to undetected humins which presumably were formed in condensation reactions of the HMF. At higher flow rates (0.5-1 mL min^{-1}) 5-MF was detected as unreacted intermediate suggesting that the HMF conversion proceeded via 5-MF and MFA to DMF. The best performance i.e. the highest productivity (ca. 7 mmol h^{-1} g^{-1}), calculated on the base of the full mass of the catalyst, was achieved at 0.75 mL min^{-1}. It is to be noted that the back pressure remained constant between 0-1 bar at all conditions. In contrast, higher back pressures were detected with the fixed-bed reactor packed with SANi_CM which made handling of the reaction difficult especially at harsher conditions i.e. higher temperatures and flow rates. Nevertheless, at a flow rate of 0.3 mL min^{-1} the DMF productivity was determined to be 1.8 mmol h^{-1} g^{-1}. This is comparable to the productivity obtained with Ni@SAZn_PC. In addition, the DMF yield and selectivity are lower (29 and 35 %, respectively) at a HMF conversion of 84 %, which can be attributed to large amounts of by-products produced at such large column residence times. Notably, GC-MS analysis revealed the simultaneous presence of DMF and 5-MF (**Figure S 16**).

Table 6 Catalytic studies with SANi_CM (284 mg, 4.06 mmol Ni) and Ni@SAZn_PC (159 mg, 0.4 mmol Ni) as catalyst for the conversion of HMF (0.1 M and 0.05 M in Ethanol, respectively) to DMF at 150 °C.

Catalyst	F [mL min^{-1}]	X [%]	Y_{DMF} [%]	S_{DMF} [%]	Δp [bar]	Productivity [mmol$_{DMF}$ h^{-1} g$_{cat}^{-1}$]
SANi_CM	0.3	84	29	35	90	1.8
Ni@SAZn_PC	0.25	100	41	41	0	1.9
	0.5	79	68	86	0-1	6.3
	0.75	56	50	89	0-1	7.08
	1.0	35	33	94	1	6.14

X=conversion of HMF; Y=yield of DMF; S= DMF selectivity; Δp= back pressure; productivity is calculate on the basis of the full catalyst mass, i.e. carbon and immobilized Ni-NPs.

Experiments with Ni@SAZn_PC were carried out over 15 h without showing any drop in performance. The catalyst was then recovered and characterized in order to obtain insights into possible structural changes in the course of the catalytic reactions. It is observed that the major part of the composite catalyst retained the initial cube morphology whereby partial fractures of the carbonaceous material into small pieces could also be observed (**Figure 5.15 a**). Corresponding TEM images (**Figure 5.15 b**) still revealed a homogeneous distribution of the Ni-NPs onto the carbon framework whereby the average particle size, determined by evaluation of the TEM images increased to almost the double size (22 nm). As catalysts are dynamic systems i.e. undergo dynamic structural changes during catalysis, any energy input in terms of temperature, pressure or convection may lead to the growth of bigger Ni-NPs at the expense of the smaller ones.[233, 234] This process, known as Ostwald ripening is shown to occur more pronounced at the outer surface of the catalyst as bigger agglomerated nanoparticles can be observed (**Figure S 18**). The corresponding diffractogram (**Figure 5.15 c**) reveals reflections than can be assigned to Ni^0. From the Ni (111) reflection the crystallite size was calculated to 25 nm which is in good accordance with the particle size determined from the evaluation of the TEM images.

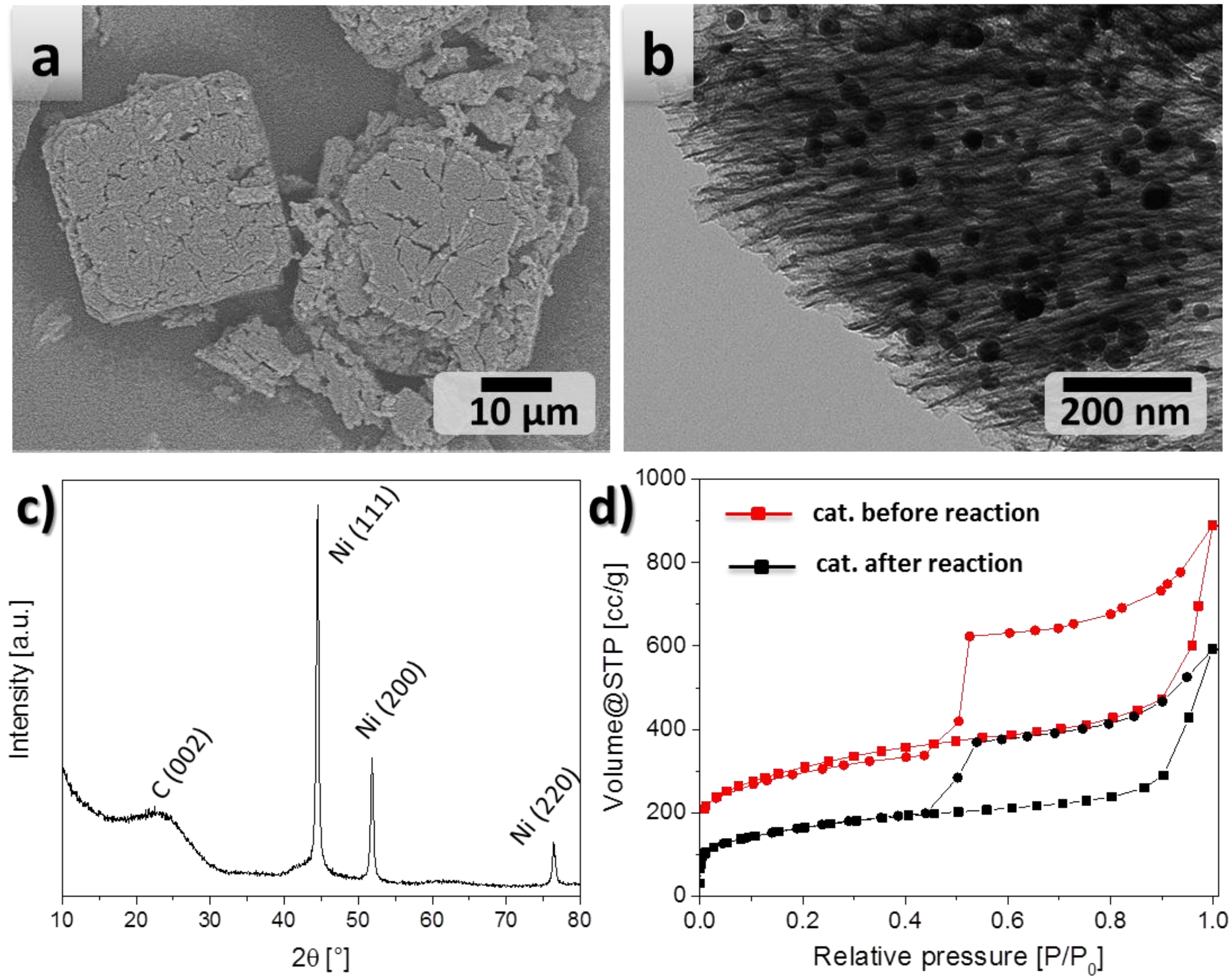

Figure 5.15 Characterization of the composite catalyst Ni@SAZn_PC recovered after the reaction. showing a) SEM micrograph, (b) corresponding TEM image, (c) XRD diffractogram, and (d) nitrogen sorption isotherm of the catalyst Ni@SAZn_PC before the reaction (red) and recovered after 15 h reaction (black). Reproduced from Mani *et al.* with the permission from Wiley.[224]

Nitrogen sorption analysis reveals a loss in surface area and total pore volume for the catalyst after 15 h of reaction (580 $m^2 g^{-1}$ and 0.92 $cm^3 g^{-1}$ compared to 1291 $m^2 g^{-1}$ and 1.55 $cm^3 g^{-1}$, respectively) (**Figure 5.15 d**). Partial pore blocking particularly of the micropores could be observed (**Figure S 19**) and might be caused by the possible presence of humins which were formed by condensation reactions of the HMF and are trapped in the pores. Nonetheless, a major part of the meso- and macropores is still well-accessible as is evident from the isotherm shapes including the shift of the desorption branch to lower relative pressures as well as the decrease of the micropore axis intercept by about 50 %. No leaching of Ni-NPs could be detected as the nickel loading did not change significantly (14.5 wt% compared to the initial 15 wt%, detected by

ICP_OES) even after 15 h of reaction time at the applied high temperatures. Despite the loss in surface area and micropore contribution, no significant decrease in catalytic performance could be observed which might be due to the fact that fluid reactions usually do not take place in this pore size regime. The nickel carbon cubes are shown to efficiently serve for the hydrogenation of HMF to DMF within a flow reactor setup over extended operation times without significant pressure drop decrease in performance. Hence, the observed fractures of the composite catalyst can rather be attributed to the unpacking process of the column. In the following, the catalyst Ni@SAZn_PC is compared to other catalysts reported in the literature for the hydrogenolysis of HMF to DMF with regard to productivity and reaction conditions. Notably, most of the current research regarding the valorization of biomass to platform chemicals and biofuels such as DMF involve batch mode processes as these are easier to handle in lab scale. However, continuous reactor set-ups have the benefit that they allow for large-scale productions of these biomass based platform chemicals and biofuels.[216, 217] As can be seen from **Table 7**, catalysts based on noble metals such as Pt, Co and Pd show the highest productivity which can be simply attributed to the high reactivity of these expensive metals. However, the composite catalyst Ni@SAZn_PC outperforms other nickel based catalysts even at much milder reaction conditions and also reveals comparable productivity to the more precious Pd-based catalysts. Considering the low costs together with the negligible pressure drop in the flow system, the herein presented composite catalyst represent very a promising catalyst for continuous reaction set-ups for biomass upgrade.

Table 7 Overview of the hydrogenolysis of HMF to DMF using different catalysts and reaction modes.

Catalyst	Mass [mg]	H_2 [bar]	T [°C]	X [%]	Time [min]	Mode	Productivity [$mmol_{DMF}$ h^{-1} g_{cat}^{-1}]
PtCo@HCS[235]	50	10	160	100	120	batch	19.20
Pd/C/Zn[236]	50	8	150	>99	8h	batch	8.40
Ni@SAZn_PC	**159**	**6**	**150**	**56**	**2.7**	**conti**	**7.08**
Ni-W_2C/AC[227]	120	40	180	100	180	batch	2.50
Ni/AC[227]	155	40	180	100	180	batch	0.97
Ru/Co_3O_4[237]	100	10	150	>99	24 h	batch	0.60

6. Summary, Conclusions and Outlook

The herein presented thesis deals with the challenge to develop alternative and effective strategies for the rational design of functional nanoporous carbon-based materials. It further aims to contribute to the current fundamental and practical understanding of the relationship between the structure of materials and the resulting properties. The concept developed herein is based on the use of coordination compounds to obtain crystalline materials which can serve as precursor materials to prepare nanoporous carbon-based materials via a facile heat treatment approach. This concept takes advantage of the fact that the structural and textural properties of the final carbonaceous materials such as morphology, porosity and surface area can be easily directed by encoding as much structural information as possible into the crystalline precursor materials. This can be simply achieved by the choice of appropriate crystal synthesis parameters such as the crystal aging temperature, metal ion concentration, solvent and organic ligand system, among others. Benefiting from the fact that the pre-defined structural properties are preserved throughout the heat treatment process at elevated temperatures, it allows circumventing the so-called “black box” issue in carbon synthesis. All coordination complexes presented and discussed herein are mainly based on the two members of the aromatic oxocarbon anions family, namely the squarate and the croconate, which are used as the organic ligand system.

The main focus of **chapter three** was to synthesize crystalline materials based on stable coordination complexes and to investigate the impact of different synthesis parameters on the crystal formation and growth mechanisms. This is important as it is widely acknowledged that the properties of materials at the nanoscale are mainly governed by the way in which the constituent building units are arranged. In the first part of this chapter, crystalline materials were synthesized based on coordination complexes of squarate and Zn^{2+} ions in water using an aging temperature of 80 °. The resulting colorless crystals (SAZn_1_80) were shown to exhibit an unusual 3D cube morphology with truncated edges and striking openings and voids face-centered on each side of the cubes. High-magnification SEM images of the cubes revealed that the cubes consist of several individual nanocrystals which are arranged in a characteristic manner giving rise to mesocrystals with meso- and macropores and an average particle diameter of approx.. 24 µm. Nitrogen sorption analyses revealed a hierarchical pore structure consisting of micro-, meso- and macropores. The crystalline nature of these mesocrystals was confirmed by XRD analysis. Based on these results, it was suggested that the single nanocrystals are based on coordination complexes which are constituted by Zn atoms coordinated by four squarate units and two water molecules in trans-position to each other forming an octahedron. This crystal lattice furthers extends to form a 3D network which is additionally stabilized by strong intermolecular hydrogen bonds between the squarate and the crystallization water molecules. It was further suggested that the resulting nanocrystals arrange either via mesoscale assembly or via oriented attachment into the 3D cube mesocrystals. In order to gain more insights into the crystal growth mechanism, squarate-zinc complexes based mesocrystals were prepared by varying the aging temperature from 4 to 100 °C. The mesocrystals prepared at low aging temperatures exhibited densely packed and smooth surfaces, whereby micrometer-sized openings and voids became visible on the centers of the low index faces along with an increase of the surface roughness as the crystal aging temperature was increased to 80 °C. This intriguing shape evolution was attributed to the Kirkendall effect, which involves the diffusion of Zn ions to the outer surface of the mesocrystals along with the characteristic voids formation. Studies of the impact of the squarate-metal ion molar ratio on the crystal growth process revealed that with increasing SA/Zn molar ratio the particle shape varies from truncated cubes to perfect cubes with right-angled edges. The latter was obtained at a SA/Zn molar ratio of 1:2 and was shown to be the thermodynamic equilibrium shape, i.e. exhibits minimized surface energies. Consequently, exceeding this equilibrium ratio yield a mixture of cubes with right-angled as well as truncated edges. Aiming to understand the impact of the metal ion on the crystal structure and shape, crystals were prepared based on coordination complexes of the squarate with various divalent 3d block metal ions including Cu^{2+}, Ni^{2+}, Co^{2+} and Cd^{2+}. The resulting crystals exhibited different colors as well as different mesocrystal shapes. This was explained on the basis of the crystal field theory and the different coordination geometries the respective metal ions adopt in their complexes due to the differences in the LFSE. In the last part of this chapter, croconate anions, which also belong to the family of the aromatic oxocarbon anions, were employed as organic ligand system to synthesize crystalline materials which are based on coordination complexes. Crystals based on croconate-zinc complexes were shown to possess an intriguing 3D hexagonal prism morphology demonstrating the impact of the organic ligand system on the crystal growth process and the morphology of the resulting mesocrystals.

In **chapter four**, the mesocrystalline materials reported in **chapter three** were used as precursor material to synthesize nanoporous carbonaceous materials. This carbon preparation synthesis takes advantage of the pre-defined structural information encoded in the mesocrystalline precursor material to direct and control the structural and textural properties of the resulting composites and carbons, respectively. All the crystalline precursors studied herein could be successfully converted into the respective composites or carbons, respectively, while maintaining the 3D particle morphologies of the respective pristine mesocrystals. For instance, the mesocrystalline precursor based on squarate-zinc coordination complexes (e.g. SAZn_1_80) could be transformed into the respective ZnO-carbon composite materials by the direct heat treatment of the precursors at 900 °C in a nitrogen atmosphere. An additional acid washing step finally yielded the respective carbon material which was shown to possess a hierarchical pore structure consisting of macropores as well as interconnected meso- and micropores. Alternatively, hierarchically porous carbon could be prepared in a facile one-step approach without the need of an additional washing step by the direct carbonization of the crystalline precursors at 1000 °C. This was explained by the carbothermal reduction of ZnO nanoparticles which were formed along with a carbonaceous framework to metallic Zn during the heat treatment process, whereby the latter was vaporized along with the release of CO_2 and CO as the temperature was raised above 900 °C. This molecular etching process allowed on the one hand for the effective removal of the inorganic compounds and on the other hand for the controlled formation of well-accessible pores. The resulting nanoporous carbons possesses large surface areas and high total pore volumes of up to 1957 $m^2 g^{-1}$ and 2.31 $cm^3 g^{-1}$, respectively, depending on the synthesis parameters.

In general, carbonaceous materials which possess a hierarchical pore structure with well-organized and interconnected pores provide several advantages which make them the material of choice in a wide range of energy and environment-based applications. Particularly for energy storage applications, for instance when used as supercapacitor electrode material, hierarchically porous carbons can be beneficial as they offer minimized diffusion distances and hence facilitate mass transport, allowing for improved specific capacitances and rate capabilities.

Therefore in **chapter five**, the hierarchically porous carbon material (SAZn_1_80_PC) derived from the direct heat treatment of the mesocrystals SAZn_1_80, was tested as a high structural density electrode material for supercapacitors. In this context, the carbon SAZn_1_80_PC showed good capacitive performance with a specific capacitance of 133 F g^{-1} in H_2SO_4 at a scan rate of 5 mV s^{-1}, whereby 67 % of the specific capacitance were retained when increasing the scan rate to 200 mV s^{-1}. This good capacitive behavior was attributed to the well-organized and accessible hierarchical pore structure of the electrode material which enabled short diffusion paths with minimized ion-transport resistance. In the last part of this chapter, the porous carbon SAZn_1_80_PC was additionally used for catalytic studies. Here, SAZn_1_80_PC served as high surface area support material and was decorated with Ni-NPs in order to obtain a composite catalyst. The concept developed herein was based on the preparation of composite materials by using SAZn_1_80_PC as support material to immobilize Ni-NPs. The resulting composite materials (Ni@SAZn_PC) were employed as heterogeneous catalyst in the selective hydrodeoxygenation of HMF to DMF in a fixed-bed flow reactor. Owing to the special 3D cube morphology of the composite catalyst, together with the well-accessible pores and the hierarchical pore structure, they allowed for the efficient and uniform packing of the fixed-bed reactor along with a maximal productivity, which was shown to be comparable to precious metal catalysts. In addition, they allowed for the performance of the hydrodeoxygenation reaction over longer time with negligible pressure drop, showing much promise in upgrading biomass-derived compounds in continuous flow reactors.

Taking into account the variety of metal species that can be immobilized onto the fundamental carbon cube framework, the herein presented synthesis strategy offers a promising route also for other catalytic reactions and opens the access to a wide range of flow conversion reactions. Thinking about the rational design of 3D carbon geometries, the functions and properties of the resulting carbon-based materials can be further expanded by the rational introduction of heteroatoms (e.g. N, B, S, P, etc.) into the carbon structures in order to alter properties such as wettability, surface polarity as well as the electrochemical landscape. In this context, the use of crystalline materials based on oxocarbon-metal ion complexes can open a platform of highly functional material for all processes which involve surface processes.

7. References

1. M. Kittler and D. Yang, *physica status solidi (a)*, 2006, **203**, 653-653.
2. A. H. Castro Neto, *Materials Today*, 2010, **13**, 12-17.
3. E. Roston, *The carbon age: how life's core element has become civilization's greatest threat*, Bloomsbury Publishing USA, 2010.
4. M. Inagaki and F. Kang, in *Materials Science and Engineering of Carbon: Fundamentals (Second Edition)*, Butterworth-Heinemann, Oxford, 2014, pp. 1-15.
5. M. Inagaki, *New Carbon Materials*, 2009, **24**, 193-232.
6. B. McEnaney, in *Carbon Materials for Advanced Technologies*, Elsevier Science Ltd, Oxford, 1999, pp. 1-33.
7. N. Fechler and M. Antonietti, *Nano Today*, 2015, **10**, 593-614.
8. M. Lazzeri and A. Barreiro, *Elements*, 2014, **10**, 447-452.
9. E. L. Wolf, in *Nanophysics and Nanotechnology*, Wiley-VCH Verlag GmbH, 2008, pp. 133-146.
10. V. Hélène, *Measurement Science and Technology*, 2003, **14**, 1487.
11. S. D. Faust and O. M. Aly, *Chemistry of Water Treatment, Second Edition*, Taylor & Francis, 1998.
12. F. H. Gojny, M. H. G. Wichmann, B. Fiedler and K. Schulte, *Composites Science and Technology*, 2005, **65**, 2300-2313.
13. R. W. Fu, Z. H. Li, Y. R. Liang, F. Li, F. Xu and D. C. Wu, *New Carbon Materials*, 2011, **26**, 171-178.
14. S. M. Manocha, *Sadhana*, 2003, **28**, 335-348.
15. J. Liu, N. P. Wickramaratne, S. Z. Qiao and M. Jaroniec, *Nat Mater*, 2015, **14**, 763-774.
16. H.-L. Jiang, B. Liu, Y.-Q. Lan, K. Kuratani, T. Akita, H. Shioyama, F. Zong and Q. Xu, *Journal of the American Chemical Society*, 2011, **133**, 11854-11857.
17. A. Thomas, *Angewandte Chemie International Edition*, 2010, **49**, 8328-8344.
18. J. Tang, J. Liu, N. L. Torad, T. Kimura and Y. Yamauchi, *Nano Today*, 2014, **9**, 305-323.
19. U. Nations, *World Population Prospects: The 2017 Revision, Key Findings and Advance Tables*, P. D. Department of Economic and Social Affairs, 2017.
20. Y. Liu and L. Ma, *Natural Gas Industry B*, 2016, **3**, 493-503.
21. P. M. Vitousek, *Ecology*, 1994, **75**, 1861-1876.
22. Y. Xie, D. Kocaefe, C. Chen and Y. Kocaefe, *Journal of Nanomaterials*, 2016, **2016**, 10.
23. A. H. Lu and F. Schüth, *Advanced Materials*, 2006, **18**, 1793-1805.
24. T.-P. Fellinger, R. J. White, M.-M. Titirici and M. Antonietti, *Advanced Functional Materials*, 2012, **22**, 3254-3260.
25. R. J. White, N. Yoshizawa, M. Antonietti and M.-M. Titirici, *Green chemistry*, 2011, **13**, 2428-2434.
26. M. Antonietti, N. Fechler and T.-P. Fellinger, *Chemistry of Materials*, 2014, **26**, 196-210.
27. L. Borchardt, Q.-L. Zhu, M. E. Casco, R. Berger, X. Zhuang, S. Kaskel, X. Feng and Q. Xu, *Materials Today*, 2017.
28. J. P. Paraknowitsch, J. Zhang, D. Su, A. Thomas and M. Antonietti, *Advanced Materials*, 2010, **22**, 87-92.
29. J. P. Paraknowitsch, A. Thomas and M. Antonietti, *Journal of Materials Chemistry*, 2010, **20**, 6746-6758.
30. N. Fechler, T.-P. Fellinger and M. Antonietti, *Advanced Materials*, 2013, **25**, 75-79.
31. N. Fechler, T.-P. Fellinger and M. Antonietti, *Chemistry of Materials*, 2012, **24**, 713-719.
32. K. Elumeeva, N. Fechler, T.-P. Fellinger and M. Antonietti, *Materials Horizons*, 2014, **1**, 588-594.
33. D. Esposito, S. Kirchhecker and M. Antonietti, *Chemistry-A European Journal*, 2013, **19**, 15097-15100.

34. S. J. Yang, R. Rothe, S. Kirchhecker, D. Esposito, M. Antonietti, H. Gojzewski and N. Fechler, *Carbon*, 2015, **94**, 641-645.
35. G. R. Desiraju, *Journal of Molecular Structure*, 2003, **656**, 5-15.
36. J. C. MacDonald, P. C. Dorrestein, M. M. Pilley, M. M. Foote, J. L. Lundburg, R. W. Henning, A. J. Schultz and J. L. Manson, *Journal of the American Chemical Society*, 2000, **122**, 11692-11702.
37. R. Viswanatha and D. D. Sarma, in *Nanomaterials Chemistry*, Wiley-VCH Verlag GmbH & Co. KGaA, 2007, pp. 139-170.
38. H. Wang, Q.-L. Zhu, R. Zou and Q. Xu, *Chem*, 2017, **2**, 52-80.
39. H. Furukawa, K. E. Cordova, M. O'Keeffe and O. M. Yaghi, *Science*, 2013, **341**, 1230444.
40. N. L. Torad, M. Hu, Y. Kamachi, K. Takai, M. Imura, M. Naito and Y. Yamauchi, *Chemical Communications*, 2013, **49**, 2521-2523.
41. T. Y. Ma, S. Dai, M. Jaroniec and S. Z. Qiao, *Journal of the American Chemical Society*, 2014, **136**, 13925-13931.
42. W. Chaikittisilp, K. Ariga and Y. Yamauchi, *Journal of Materials Chemistry A*, 2013, **1**, 14-19.
43. X. Wang, G. Sun, P. Routh, D.-H. Kim, W. Huang and P. Chen, *Chemical Society Reviews*, 2014, **43**, 7067-7098.
44. P. Zhang, F. Sun, Z. Xiang, Z. Shen, J. Yun and D. Cao, *Energy & Environmental Science*, 2014, **7**, 442-450.
45. R. R. Salunkhe, Y. V. Kaneti, J. Kim, J. H. Kim and Y. Yamauchi, *Acc. Chem. Res*, 2016, **49**, 2796-2806.
46. S. J. Yang, M. Antonietti and N. Fechler, *Journal of the American Chemical Society*, 2015, **137**, 8269-8273.
47. C. M. Mani, T. Berthold and N. Fechler, *Small*, 2016, **12**, 2906-2912.
48. C. Robl and A. Weiss, *Zeitschrift für Naturforschung*, 1986, **41 b**, 1341-1345.
49. D. Braga, L. Maini, F. Grepioni, F. Mota, C. Rovira and J. J. Novoa, *Chemistry – A European Journal*, 2000, **6**, 4536-4551.
50. S. L. Georgopoulos, R. Diniz, M. I. Yoshida, N. L. Speziali, H. F. D. Santos, G. M. A. Junqueira and L. F. C. de Oliveira, *Journal of Molecular Structure*, 2006, **794**, 63-70.
51. S. L. Georgopoulos, R. Diniz, B. L. Rodrigues and L. F. C. de Oliveira, *Journal of Molecular Structure*, 2005, **741**, 61-66.
52. A. Walcarius, *Chemical Society Reviews*, 2013, **42**, 4098-4140.
53. M. Tagliazucchi and I. Szleifer, *Materials Today*, 2015, **18**, 131-142.
54. L. Addadi and S. Weiner, *Nature*, 1997, **389**, 912-915.
55. P. Ruz, S. Banerjee, M. Pandey, V. Sudarsan, P. U. Sastry and R. J. Kshirsagar, *Solid State Sciences*, 2016, **62**, 105-111.
56. C. M. A. Parlett, K. Wilson and A. F. Lee, *Chemical Society Reviews*, 2013, **42**, 3876-3893.
57. D.-W. Wang, F. Li, M. Liu, G. Q. Lu and H.-M. Cheng, *Angewandte Chemie International Edition*, 2008, **47**, 373-376.
58. M. Antonietti and M. Titirici, *Journal*, 2012.
59. S.-A. Wohlgemuth, Dissertation, University of Potsdam, 2012.
60. A. G. Pandolfo and A. F. Hollenkamp, *Journal of Power Sources*, 2006, **157**, 11-27.
61. R. E. Franklin, *Proceedings of the Royal Society of London. Series A. Mathematical and Physical Sciences*, 1951, **209**, 196-218.
62. R. Franklin, *Acta Crystallographica*, 1950, **3**, 107-121.
63. A. Oberlin, *Carbon*, 1984, **22**, 521-541.
64. M. Thommes, K. Kaneko, A. V. Neimark, J. P. Olivier, F. Rodriguez-Reinose, J. Rouquerol and K. S. W. Sing, *Pure and Applied Chemistry*, 2015, **87**, 1051-1069.
65. S. H. Park and Y. Xia, *Advanced Materials*, 1998, **10**, 1045-1048.
66. F. Caruso, *Chemistry-A European Journal*, 2000, **6**, 413-419.

67. G. Gundiah, A. Govindaraj and C. N. R. Rao, *Materials Research Bulletin*, 2001, **36**, 1751-1757.
68. A. Ahmadpour and D. D. Do, *Carbon*, 1996, **34**, 471-479.
69. M. A. Lillo-Ródenas, D. Cazorla-Amorós and A. Linares-Solano, *Carbon*, 2003, **41**, 267-275.
70. J. A. Maciá-Agulló, B. C. Moore, D. Cazorla-Amorós and A. Linares-Solano, *Carbon*, 2004, **42**, 1367-1370.
71. N. Pal and A. Bhaumik, *Advances in Colloid and Interface Science*, 2013, **189**, 21-41.
72. W. Schwieger, A. G. Machoke, T. Weissenberger, A. Inayat, T. Selvam, M. Klumpp and A. Inayat, *Chemical Society Reviews*, 2016, **45**, 3353-3376.
73. S. Lopez-Orozco, A. Inayat, A. Schwab, T. Selvam and W. Schwieger, *Advanced Materials*, 2011, **23**, 2602-2615.
74. J. Čejka, G. Centi, J. Perez-Pariente and W. J. Roth, *Catalysis Today*, 2012, **179**, 2-15.
75. M. S. Holm, E. Taarning, K. Egeblad and C. H. Christensen, *Catalysis Today*, 2011, **168**, 3-16.
76. D. Schneider, D. Mehlhorn, P. Zeigermann, J. Karger and R. Valiullin, *Chemical Society Reviews*, 2016, **45**, 3439-3467.
77. S. L. Jin, H. G. Deng, L. Zhan, W. M. Qiao and L. C. Ling, *New Carbon Materials*, 2012, **27**, 87-92.
78. Y. Deng, C. Liu, T. Yu, F. Liu, F. Zhang, Y. Wan, L. Zhang, C. Wang, B. Tu, P. A. Webley, H. Wang and D. Zhao, *Chemistry of Materials*, 2007, **19**, 3271-3277.
79. A.-H. Lu, G.-P. Hao, Q. Sun, X.-Q. Zhang and W.-C. Li, *Macromolecular Chemistry and Physics*, 2012, **213**, 1107-1131.
80. H. Li, M. Eddaoudi, M. O'Keeffe and O. M. Yaghi, *Nature*, 1999, **402**, 276-279.
81. B. Xiao and Q. Yuan, *Particuology*, 2009, **7**, 129-140.
82. J. L. C. Rowsell and O. M. Yaghi, *Microporous and Mesoporous Materials*, 2004, **73**, 3-14.
83. X. Lin, J. Jia, N. R. Champness, P. Hubberstey and M. Schröder, in *Solid-State Hydrogen Storage*, Woodhead Publishing, 2008, pp. 288-312.
84. J.-R. Li, R. J. Kuppler and H.-C. Zhou, *Chemical Society Reviews*, 2009, **38**, 1477-1504.
85. R. J. Kuppler, D. J. Timmons, Q.-R. Fang, J.-R. Li, T. A. Makal, M. D. Young, D. Yuan, D. Zhao, W. Zhuang and H.-C. Zhou, *Coordination Chemistry Reviews*, 2009, **253**, 3042-3066.
86. J. Lee, O. K. Farha, J. Roberts, K. A. Scheidt, S. T. Nguyen and J. T. Hupp, *Chemical Society Reviews*, 2009, **38**, 1450-1459.
87. X. Lin, J. Jia, P. Hubberstey, M. Schroder and N. R. Champness, *CrystEngComm*, 2007, **9**, 438-448.
88. B. Liu, H. Shioyama, T. Akita and Q. Xu, *Journal of the American Chemical Society*, 2008, **130**, 5390-5391.
89. S. J. Yang, T. Kim, J. H. Im, Y. S. Kim, K. Lee, H. Jung and C. R. Park, *Chemistry of Materials*, 2012, **24**, 464-470.
90. N. L. Torad, M. Hu, S. Ishihara, H. Sukegawa, A. A. Belik, M. Imura, K. Ariga, Y. Sakka and Y. Yamauchi, *Small*, 2014, **10**, 2096-2107.
91. G. R. Desiraju, J. J. Vittal and A. Ramanan, *Crystal engineering: a textbook*, World Scientific, 2011.
92. S. T. Meek, J. A. Greathouse and M. D. Allendorf, *Advanced Materials*, 2011, **23**, 249-267.
93. D. N. Reinhoudt, *Supramolecular materials and technologies*, John Wiley & Sons, 2008.
94. J. W. Mullin, in *Crystallization (Fourth Edition)*, Butterworth-Heinemann, Oxford, 2001, pp. 181-215.
95. J. W. Mullin, in *Crystallization (Fourth Edition)*, Butterworth-Heinemann, Oxford, 2001, pp. 216-288.
96. H. Cölfen and M. Antonietti, *Angewandte Chemie International Edition*, 2005, **44**, 5576-5591.
97. S. Mann, *Biomineralization: principles and concepts in bioinorganic materials chemistry*, Oxford University Press on Demand, 2001.
98. H. Cölfen and S. Mann, *Angewandte Chemie International Edition*, 2003, **42**, 2350-2365.
99. H. Cöelfen and M. Antonietti, *Mesocrystals and nonclassical crystallization*, John Wiley & Sons, 2008.

100. M. Niederberger and H. Colfen, *Physical Chemistry Chemical Physics*, 2006, **8**, 3271-3287.
101. E. R. Leite and C. Ribeiro, *Crystallization and growth of colloidal nanocrystals*, Springer Science & Business Media, 2011.
102. L. Bahrig, S. G. Hickey and A. Eychmuller, *CrystEngComm*, 2014, **16**, 9408-9424.
103. G. H. Nancollas, *Biological mineralization and demineralization: report of the Dahlem Workshop on Biological Mineralization and Demineralization, Berlin 1981, October 18-23*, Springer, 1982.
104. G. Madras and B. J. McCoy, *Acta Materialia*, 2003, **51**, 2031-2040.
105. V. K. LaMer and R. H. Dinegar, *Journal of the American Chemical Society*, 1950, **72**, 4847-4854.
106. Y. Politi, T. Arad, E. Klein, S. Weiner and L. Addadi, *Science*, 2004, **306**, 1161-1164.
107. L. Qi, H. Cölfen, M. Antonietti, M. Li, J. D. Hopwood, A. J. Ashley and S. Mann, *Chemistry – A European Journal*, 2001, **7**, 3526-3532.
108. N. Gehrke, N. Nassif, N. Pinna, M. Antonietti, H. S. Gupta and H. Cölfen, *Chemistry of Materials*, 2005, **17**, 6514-6516.
109. M. Faatz, F. Gröhn and G. Wegner, *Advanced Materials*, 2004, **16**, 996-1000.
110. L. B. Gower, *Chemical Reviews*, 2008, **108**, 4551-4627.
111. J. F. Banfield, S. A. Welch, H. Zhang, T. T. Ebert and R. L. Penn, *Science*, 2000, **289**, 751-754.
112. R. L. Penn and J. F. Banfield, *Science*, 1998, **281**, 969-971.
113. R. L. Penn and J. F. Banfield, *Geochimica et Cosmochimica Acta*, 1999, **63**, 1549-1557.
114. E. J. H. Lee, C. Ribeiro, E. Longo and E. R. Leite, *The Journal of Physical Chemistry B*, 2005, **109**, 20842-20846.
115. R.-Q. Song and H. Cölfen, *Advanced Materials*, 2010, **22**, 1301-1330.
116. L. Zhou and P. O'Brien, *Small*, 2008, **4**, 1566-1574.
117. R. West, H.-Y. Niu, D. L. Powell and M. V. Evans, *Journal of the American Chemical Society*, 1960, **82**, 6204-6205.
118. R. West and J. Niu, in *The Carbonyl Group (1970)*, John Wiley & Sons, Ltd., 2010, pp. 241-275.
119. R. West and D. L. Powell, *Journal of the American Chemical Society*, 1963, **85**, 2577-2579.
120. G. M. A. Junqueira, W. R. Rocha, W. B. De Almeida and H. F. Dos Santos, *Physical Chemistry Chemical Physics*, 2003, **5**, 437-445.
121. O. Kovalchukova and S. Strashnova, *Reviews in Inorganic Chemistry*, 2014, **34**, 1-24.
122. M. Ito and R. West, *Journal of the American Chemical Society*, 1963, **85**, 2580-2584.
123. E. Patton and R. West, *The Journal of Physical Chemistry*, 1970, **74**, 2512-2518.
124. R. West, *Oxocarbons*, Academic Press, New York, 1980.
125. M. J. S. Dewar and C. De Llano, *Journal of the American Chemical Society*, 1969, **91**, 789-795.
126. L. J. Schaad and B. A. Hess, *Journal of the American Chemical Society*, 1972, **94**, 3068-3074.
127. J. Aihara, *Journal of the American Chemical Society*, 1981, **103**, 1633-1635.
128. P. v. R. Schleyer, K. Najafian, B. Kiran and H. Jiao, *The Journal of Organic Chemistry*, 2000, **65**, 426-431.
129. M.-D. Serb, I. Kalf and U. Englert, *CrystEngComm*, 2014, **16**, 10631-10639.
130. A. M. Galibert, B. Soula, B. Donnadieu and P.-L. Fabre, *Inorganica Chimica Acta*, 2001, **313**, 160-164.
131. A. Weiss, E. Riegler, I. Alt, H. Böhme and C. Robl, *Zeitschrift für Naturforschung B*, 1986, **41**, 18-24.
132. G. Bernardinelli, D. Deguenon, R. Soules and P. Castan, *Canadian Journal of Chemistry-Revue Canadienne De Chimie*, 1989, **67**, 1158-1165.
133. B. Zheng, H. Dong, J. Bai, Y. Li, S. Li and M. Scheer, *Journal of the American Chemical Society*, 2008, **130**, 7778-7779.
134. L. A. Hall and D. J. Williams, in *Advances in Inorganic Chemistry*, Academic Press, 2001, vol. Volume 52, pp. 249-291.

135. X. Solans, M. Aguilo, A. Gleizes, J. Faus, M. Julve and M. Verdaguer, *Inorganic Chemistry*, 1990, **29**, 775-784.
136. M. D. ŞErb, B. Braun, O. Oprea and F. Dumitru, *Digest Journal of Nanomaterials & Biostructures (DJNB)*, 2013, **8**, 797-804.
137. S. Neeraj, M. L. Noy, C. N. R. Rao and A. K. Cheetham, *Solid State Sciences*, 2002, **4**, 1231-1236.
138. F. Artizzu, P. Deplano, L. Pilia, A. Serpe, L. Marchiò, K. Bernot and M. L. Mercuri, *Inorganica Chimica Acta*, 2011, **370**, 474-481.
139. A. J. Fatiadi, in *Oxocarbons*, Academic Press, 1980, pp. 59-77.
140. R. West and H. Y. Niu, *Journal of the American Chemical Society*, 1963, **85**, 2586-2588.
141. Y. He, B. Li, M. O'Keeffe and B. Chen, *Chemical Society Reviews*, 2014, **43**, 5618-5656.
142. W. Lu, Z. Wei, Z.-Y. Gu, T.-F. Liu, J. Park, J. Park, J. Tian, M. Zhang, Q. Zhang, T. Gentle Iii, M. Bosch and H.-C. Zhou, *Chemical Society Reviews*, 2014, **43**, 5561-5593.
143. Z.-W. Wang, M. Chen, C.-S. Liu, X. Wang, H. Zhao and M. Du, *Chemistry – A European Journal*, 2015, **21**, 17215-17219.
144. S. Wohlrab, N. Pinna, M. Antonietti and H. Cölfen, *Chemistry – A European Journal*, 2005, **11**, 2903-2913.
145. F.-X. Bu, M. Hu, W. Zhang, Q. Meng, L. Xu, D.-M. Jiang and J.-S. Jiang, *Chemical Communications*, 2015, **51**, 17568-17571.
146. M. Hu, J.-S. Jiang, C.-C. Lin and Y. Zeng, *CrystEngComm*, 2010, **12**, 2679-2683.
147. F.-X. Bu, M. Hu, L. Xu, Q. Meng, G.-Y. Mao, D.-M. Jiang and J.-S. Jiang, *Chemical Communications*, 2014, **50**, 8543-8546.
148. X.-J. Zheng, Q. Kuang, T. Xu, Z.-Y. Jiang, S.-H. Zhang, Z.-X. Xie, R.-B. Huang and L.-S. Zheng, *The Journal of Physical Chemistry C*, 2007, **111**, 4499-4502.
149. B. I. Kharisov, O. V. Kharissova and U. Ortiz Méndez, *Journal of Coordination Chemistry*, 2013, **66**, 3791-3828.
150. C. Y. Tai and C.-k. Chen, *Chemical Engineering Science*, 2008, **63**, 3632-3642.
151. D. B. Patience, University of Wisconsin--Madison, 2002.
152. W. Borchardt-Ott, *Crystallography: an introduction*, Springer Science & Business Media, 2011.
153. A. Krężel and W. Maret, *Archives of biochemistry and biophysics*, 2016, **611**, 3-19.
154. K. L. Haas and K. J. Franz, *Chemical reviews*, 2009, **109**, 4921-4960.
155. Y. Yin, R. M. Rioux, C. K. Erdonmez, S. Hughes, G. A. Somorjai and A. P. Alivisatos, *Science*, 2004, **304**, 711-714.
156. J. X. Wang, C. Ma, Y. Choi, D. Su, Y. Zhu, P. Liu, R. Si, M. B. Vukmirovic, Y. Zhang and R. R. Adzic, *Journal of the American Chemical Society*, 2011, **133**, 13551-13557.
157. L. Gao, C. Pang, D. He, L. Shen, A. Gupta and N. Bao, *Scientific reports*, 2015, **5**, 16061.
158. A. Smigelskas and E. Kirkendall, *Trans. Aime*, 1947, **171**, 130-142.
159. X. Tian, J. Li, K. Chen, J. Han and S. Pan, *Crystal Growth & Design*, 2009, **9**, 4927-4932.
160. J. Greve and C. Naether, *Acta Crystallographica Section E: Structure Reports Online*, 2002, **58**, m653-m655.
161. B. Stuart, *Infrared spectroscopy : fundamentals and applications*, Chichester, West Sussex, England ; Hoboken, NJ : J. Wiley, [2004] ©2004, 2004.
162. G. V. SEGUEL, B. L. RIVAS and C. PAREDES, *Journal of the Chilean Chemical Society*, 2010, **55**, 5-7.
163. A. Novak, in *Large Molecules*, Springer Berlin Heidelberg, Berlin, Heidelberg, 1974, pp. 177-216.
164. M. Thommes, *Chemie Ingenieur Technik*, 2010, **82**, 1059-1073.
165. K. A. Cychosz, R. Guillet-Nicolas, J. Garcia-Martinez and M. Thommes, *Chemical Society Reviews*, 2017, **46**, 389-414.
166. P. Afanasiev, *The Journal of Physical Chemistry C*, 2012, **116**, 2371-2381.
167. B. N. Figgis, *Comprehensive Coordination Chemistry*, 1987, **1**, 213-279.
168. L. H. Gade, *Koordinationschemie*, John Wiley & Sons, 2012.

169. M. Allegrini, N. García and O. Marti, *Nanometer scale science and technology*, IOS Press, 2001.
170. M. C. Roco, R. S. Williams and P. Alivisatos, *Nanotechnology research directions: IWGN workshop report: vision for nanotechnology in the next decade*, Springer Science & Business Media, 2000.
171. Y. Gong, Z. Wei, J. Wang, P. Zhang, H. Li and Y. Wang, 2014, **4**, 6349.
172. D. H. Doughty, B. Vyas, T. Takamura and J. R. Huff, *Materials for electrochemical energy storage and conversion -- Batteries, capacitors and fuel cells*, Materials Research Society, Pittsburgh, PA (United States), 1995.
173. B. Fang, J. H. Kim, M. Kim and J.-S. Yu, *Chemistry of Materials*, 2009, **21**, 789-796.
174. G.-P. Hao, G. Mondin, Z. Zheng, T. Biemelt, S. Klosz, R. Schubel, A. Eychmüller and S. Kaskel, *Angewandte Chemie International Edition*, 2015, **54**, 1941-1945.
175. M. Hu, J. Reboul, S. Furukawa, N. L. Torad, Q. Ji, P. Srinivasu, K. Ariga, S. Kitagawa and Y. Yamauchi, *Journal of the American Chemical Society*, 2012, **134**, 2864-2867.
176. W. Chaikittisilp, M. Hu, H. Wang, H.-S. Huang, T. Fujita, K. C. W. Wu, L.-C. Chen, Y. Yamauchi and K. Ariga, *Chemical Communications*, 2012, **48**, 7259-7261.
177. N. L. Torad, R. R. Salunkhe, Y. Li, H. Hamoudi, M. Imura, Y. Sakka, C. C. Hu and Y. Yamauchi, *Chemistry-A European Journal*, 2014, **20**, 7895-7900.
178. R. R. Salunkhe, Y. V. Kaneti, J. Kim, J. H. Kim and Y. Yamauchi, *Accounts of Chemical Research*, 2016, **49**, 2796-2806.
179. F. C. Porter, *Zinc Handbook:Properties, Processing, and Use in Design*, Mark Dekker, Inc., New York, 1991.
180. H. B. Aiyappa, P. Pachfule, R. Banerjee and S. Kurungot, *Crystal Growth & Design*, 2013, **13**, 4195-4199.
181. C. J. Rasmussen, A. Vishnyakov, M. Thommes, B. M. Smarsly, F. Kleitz and A. V. Neimark, *Langmuir*, 2010, **26**, 10147-10157.
182. M. Zhang, W. X. Bao, X. L. Liu, B. Z. Yu, Z. Y. Ren, J. T. Bai and H. M. Fan, *Journal of materials science*, 2015, **50**, 7875-7883.
183. B. D. Alleyne, L. A. Hall, H.-A. Hosein, H. Jaggernauth, A. J. P. White and D. J. Williams, *Journal of the Chemical Society, Dalton Transactions*, 1998, 3845-3850.
184. J. Hu, W. Yuan, Z. Yan, B. Zhou, Y. Tang and Z. Li, *Applied Surface Science*, 2015, **355**, 145-152.
185. S. Dutta, A. Bhaumik and K. C. W. Wu, *Energy & Environmental Science*, 2014, **7**, 3574-3592.
186. Z. Zheng and Q. Gao, *Journal of Power Sources*, 2011, **196**, 1615-1619.
187. L. L. Zhang and X. S. Zhao, *Chemical Society Reviews*, 2009, **38**, 2520-2531.
188. M. Winter and R. J. Brodd, *Chemical Reviews*, 2004, **104**, 4245-4270.
189. J. R. Miller and P. Simon, *Science*, 2008, **321**, 651-652.
190. A. Davies and A. Yu, *The Canadian Journal of Chemical Engineering*, 2011, **89**, 1342-1357.
191. J. S. L. Philpot, *The London, Edinburgh, and Dublin Philosophical Magazine and Journal of Science*, 1932, **13**, 775-795.
192. D. C. Grahame, *Chemical reviews*, 1947, **41**, 441-501.
193. P. Simon and Y. Gogotsi, *Nat Mater*, 2008, **7**, 845-854.
194. K.-C. Tsay, L. Zhang and J. Zhang, *Electrochimica Acta*, 2012, **60**, 428-436.
195. W. Xin and Y. Song, *RSC Advances*, 2015, **5**, 83239-83285.
196. Y. Liang, J. Wei, X. Zhang, J. Zhang, S. P. Jiang and H. Wang, *ChemCatChem*, 2016, **8**, 1901-1904.
197. M. L. Toebes, J. A. van Dillen and K. P. de Jong, *Journal of Molecular Catalysis A: Chemical*, 2001, **173**, 75-98.
198. M. Okumura, K. Sakata, K. Tada, S. Yamada, K. Okazaki, Y. Kitagawa, T. Kawakami and S. Yamanaka, in *Quantum Systems in Chemistry and Physics: Progress in Methods and Applications*, eds. K. Nishikawa, J. Maruani, E. J. Brändas, G. Delgado-Barrio and P. Piecuch, Springer Netherlands, Dordrecht, 2012, pp. 363-375.

199. X. Xu, Y. Li, Y. Gong, P. Zhang, H. Li and Y. Wang, *Journal of the American Chemical Society*, 2012, **134**, 16987-16990.
200. Y.-C. Lin and G. W. Huber, *Energy & Environmental Science*, 2009, **2**, 68-80.
201. L. Hu, G. Zhao, W. Hao, X. Tang, Y. Sun, L. Lin and S. Liu, *RSC Advances*, 2012, **2**, 11184-11206.
202. Y. Qian, L. Zhu, Y. Wang and X. Lu, *Renewable and Sustainable Energy Reviews*, 2015, **41**, 633-646.
203. L. D. Schmidt and P. J. Dauenhauer, *Nature*, 2007, **447**, 914-915.
204. H. L. S. Y. L. Lu, *Progress in Chemistry*, 2011, **10**, 011.
205. J. B. Binder and R. T. Raines, *Journal of the American Chemical Society*, 2009, **131**, 1979-1985.
206. Y. Roman-Leshkov, C. J. Barrett, Z. Y. Liu and J. A. Dumesic, *Nature*, 2007, **447**, 982-985.
207. B. R. Caes, R. E. Teixeira, K. G. Knapp and R. T. Raines, *ACS Sustainable Chemistry & Engineering*, 2015, **3**, 2591-2605.
208. X. Xiang, J. Cui, G. Ding, H. Zheng, Y. Zhu and Y. Li, *ACS Sustainable Chemistry & Engineering*, 2016, **4**, 4506-4510.
209. J. Chmiola, G. Yushin, Y. Gogotsi, C. Portet, P. Simon and P. L. Taberna, *Science*, 2006, **313**, 1760-1763.
210. D. A. C. Brownson and C. E. Banks, in *The Handbook of Graphene Electrochemistry*, Springer London, London, 2014, pp. 23-77.
211. W. Qian, J. Zhu, Y. Zhang, X. Wu and F. Yan, *Small*, 2015, **11**, 4959-4969.
212. H.-J. Choi, S.-M. Jung, J.-M. Seo, D. W. Chang, L. Dai and J.-B. Baek, *Nano Energy*, 2012, **1**, 534-551.
213. E. Frackowiak, *Physical Chemistry Chemical Physics*, 2007, **9**, 1774-1785.
214. C. H. Bartholomew and W. C. Hecker, *Chemical Engineering*, 1994, **101**, 70.
215. A. Bisio, *Catalysis today*, 1997, **36**, 367-374.
216. K.-D. Henkel, in *Ullmann's Encyclopedia of Industrial Chemistry*, Wiley-VCH Verlag GmbH & Co. KGaA, 2000.
217. V. V. RANADE, *Journal of Chemical Sciences*, 2014, **126**, 341-351.
218. G. Eigenberger, in *Handbook of Heterogeneous Catalysis*, Wiley-VCH Verlag GmbH & Co. KGaA, 2008.
219. G. Eigenberger and W. Ruppel, in *Ullmann's Encyclopedia of Industrial Chemistry*, Wiley-VCH Verlag GmbH & Co. KGaA, 2000.
220. L. L. Hegedus, *Industrial & Engineering Chemistry Product Research and Development*, 1980, **19**, 533-537.
221. V. Z. Mordkovich, V. S. Ermolaev, E. B. Mitberg, L. V. Sineva, I. G. Solomonik, I. S. Ermolaev and E. Y. Asalieva, *Research on Chemical Intermediates*, 2015, **41**, 9539-9550.
222. G. Jacobs, W. E. Alvarez and D. E. Resasco, *Applied Catalysis A: General*, 2001, **206**, 267-282.
223. A. F. Orrego-Romero, O. F. Arbeláez-Pérez, F. Bustamante-Londoño and A. L. Villa-Holguín, *Revista Facultad de Ingeniería Universidad de Antioquia*, 2016, 38-47.
224. C. Mbaya Mani, M. Braun, V. Molinari, M. Antonietti and N. Fechler, *ChemCatChem*, 2017, DOI: 10.1002/cctc.201700506.
225. K. M. Brunner, H. D. Perez, R. P. S. Peguin, J. C. Duncan, L. D. Harrison, C. H. Bartholomew and W. C. Hecker, *Industrial & Engineering Chemistry Research*, 2015, **54**, 2902-2909.
226. T. V. Kotbagi, H. R. Gurav, A. S. Nagpure, S. V. Chilukuri and M. G. Bakker, *RSC Advances*, 2016, **6**, 67662-67668.
227. Y.-B. Huang, M.-Y. Chen, L. Yan, Q.-X. Guo and Y. Fu, *ChemSusChem*, 2014, **7**, 1068-1072.
228. M. W. Losey, M. A. Schmidt and K. F. Jensen, *Industrial & Engineering Chemistry Research*, 2001, **40**, 2555-2562.
229. M. F. Mendes, in *Mass transfer in chemical engineering processes*, ed. J. Markoš, InTech, Rijeka, Croatia, 2011.

230. A. S. Said, *AIChE Journal*, 1956, **2**, 477-481.
231. W. L. R. Souza, C. S. Silva, L. A. C. Meleiro and M. F. Mendes, *Brazilian Journal of Chemical Engineering*, 2016, **33**, 415-426.
232. A. G. Williamson, *Journal of Chemical Education*, 1962, **39**, 579.
233. J. Cao, R. Farra, Z.-J. Wang, A. Rinaldi, R. Schlögl and M. G. Willinger, in *European Microscopy Congress 2016: Proceedings*, Wiley-VCH Verlag GmbH & Co. KGaA, 2016.
234. W. Yuan, Y. Wang, H. Li, H. Wu, Z. Zhang, A. Selloni and C. Sun, *Nano Letters*, 2016, **16**, 132-137.
235. G.-H. Wang, J. Hilgert, F. H. Richter, F. Wang, H.-J. Bongard, B. Spliethoff, C. Weidenthaler and F. Schüth, *Nat Mater*, 2014, **13**, 293-300.
236. B. Saha, C. M. Bohn and M. M. Abu-Omar, *ChemSusChem*, 2014, **7**, 3095-3101.
237. Y. Zu, P. Yang, J. Wang, X. Liu, J. Ren, G. Lu and Y. Wang, *Applied Catalysis B: Environmental*, 2014, **146**, 244-248.

A. Applied Methods

Powder X-ray diffraction

X-ray diffraction (XRD) is a non-destructive and important analytical technique allowing for the structural characterization of crystalline materials. It is mainly based on the interaction and scattering of monochromatic electromagnetic radiation (X-ray) on the lattice planes of a crystalline material. Here, the scattered x-ray waves can interfere with each other in a constructive or destructive manner. According to Bragg's Law (Equ. 7.1), constructive interference results when the wavelength of the incident beam of X-rays is in the same range than the interlayer spacing d of the lattice planes and the reflected waves are phase shifted by any integer multiple n. In contrast, if the waves are out-of-phase, then destructive interference results meaning that the waves cancel each other out.

$$\boldsymbol{n\,\lambda = 2d\,sin\,(\theta)} \tag{7.1}$$

By proper interpretation of the characteristic x-ray diffraction pattern and comparison with standard reference patterns, it is possible to identify crystalline components in a material. Commonly, crystalline materials yield diffractograms with intense and narrow reflections, whereas broader and weaker reflections are obtained with increasing lattice imperfection in the material. Moreover, depending on the 2θ range observed, it is distinguished between Small Angle X-ray Scattering (SAXS) and Wide Angle X-ray Scattering (WAXS). The former refers to the analysis of colloidal structures of sizes between 1-100 nm, which typically cause reflections at very small angles ($2\theta < 5°$). In contrast, WAXS is applied for the analysis of atomic structures observed at 2θ values above 5°. The crystallite size Δd can be determined by using the Scherrer equation:

$$\boldsymbol{\Delta d = \frac{K\lambda}{\beta \cos\,(\theta)}} \tag{7.2}$$

where K is a dimensionless shape factor ($K = 0.9$), β is the full width at half maximum (in radian measure) and θ is the Bragg angle.

XRD measurements were conducted on a Bruker D8 Advance instrument equipped with a scintillation detector using Cu Kα radiation (λ = 1.5418 Å). All reference patterns used herein were obtained from the ICDD PDF 4+ database.

Nitrogen sorption analysis

Nitrogen sorption is widely applied for the characterization of the texture of porous materials and provides information regarding the pore structure, specific surface area, total pore volume and pore size distribution. In general, it is based on the interaction between a gas (adsorbate) and a porous solid (adsorbent) at a constant temperature and at the equilibrium vapor pressure of the respective gas. For instance, when using nitrogen as adsorbate the measurement is conducted at 77 K until reaching the atmospheric pressure ($P/P_0 = 1$). In a typical measurement, nitrogen is given in dosed amounts into measurement cell filled with the adsorbent whereby the gas volume is slowly increased until reaching the atmospheric pressure. Thereby, the amount of gas adsorbed by the specimen is monitored with respect to the relative pressure thus giving rise to the adsorption branch of the isotherm. The desorption branch is subsequently obtained upon lowering the gas pressure which consequently leads to desorption of the gas molecules from the adsorbent's pores and surface, respectively. The resulting isotherm exhibits a characteristic shape which provides insight into the pore structure in the specimen.

In general, pores are classified by the IUPAC based on their pore diameters d into micropores ($d < 2$ nm), mesopores ($d = 2\text{-}50$ nm) and macropores ($d > 50$ nm). Depending on the pore size regime and the pore network, different sorption effects can be observed resulting in different isotherm shapes, which are grouped into the following types:

Isotherms of type I are reversible and characteristic of microporous materials which possess relatively small external surface. Here, it is further distinguished between type I (a) and type I (b) isotherms. The former is obtained in case of microporous solids which mainly contain narrow micropores of widths smaller than 1 nm. In contrast, type I (b) isotherms are obtained for materials with wider micropores and possibly narrow mesopores with pore widths smaller than 2.5 nm. In general, a steep uptake at low relative pressures (P/P_0) can be observed and attributed to enhanced interactions between the adsorbent and adsorbate resulting in micropores filling. Reversible type II isotherms are mostly observed in case of nonporous or microporous solids. Here, the point B hints to a completed monolayer coverage which is followed by multilayer adsorption. This gives rise to the characteristic isotherm shape with an infinite amount of adsorbed gas at the saturation pressure $P/P_0 = 1$.

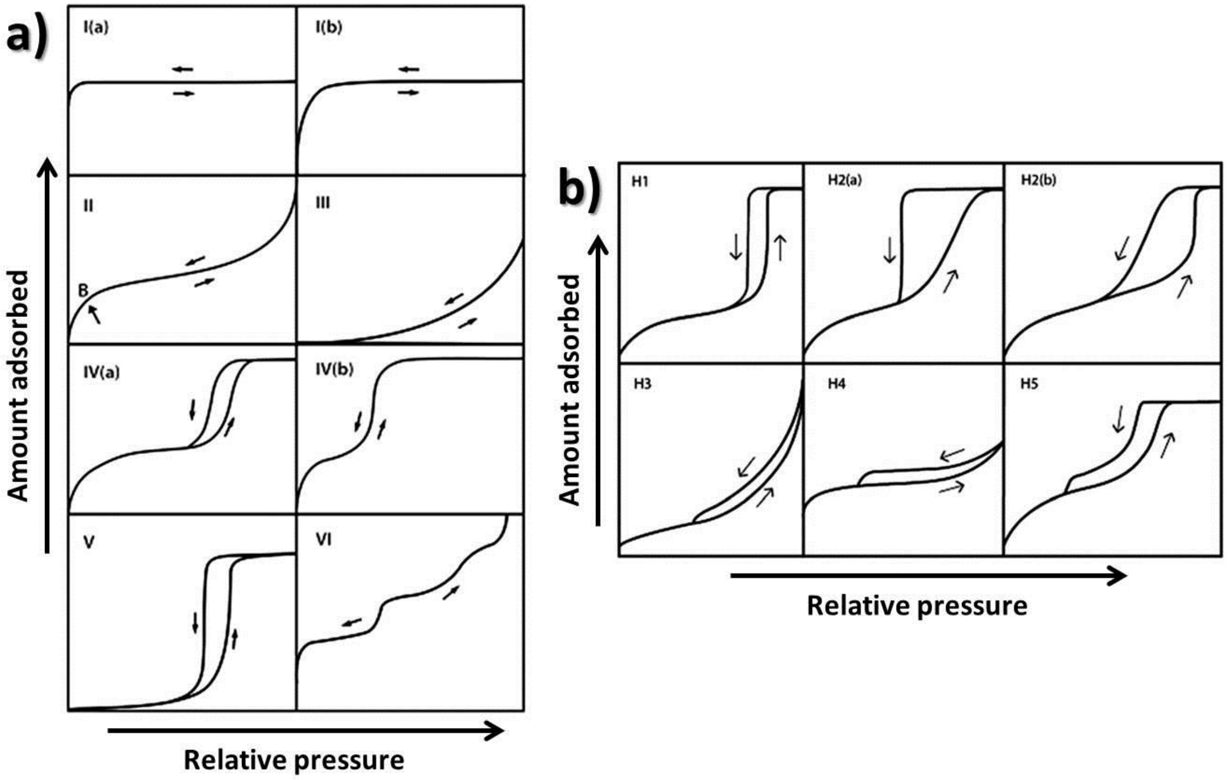

Figure 7.1 IUPAC classification showing a) different types of nitrogen sorption isotherms, b) different types of hysteresis loops. Adapted from Thommes *et al.*[64]

A type III isotherm is also typical of a nonporous or microporous material. However, as can be seen in **Figure 7.1 a** it lacks a point B and therefore possesses no identifiable monolayer formation. This can be attributed to very weak adsorbate-adsorbent interactions. Isotherms of type IV are characteristic of mesoporosity. Here, the isotherm shape is governed by the adsorbate-adsorbent interactions as well as by the interactions between the condensed molecules. A typical feature of type IV isotherms it the presence of a hysteresis loop which typically results from capillary condensation in pores wider than *d* = 4 nm. Depending on the pore shape and pore structure, the hysteresis loops can exhibit different forms, which have been classified by IUPAC into six types (**Figure 7.1 b**). Type V and VI isotherms are rarely observed and point to weak adsorbent-adsorbate interactions in a mesoporous solid and to a layer-by-layer adsorption on the surface of a nonporous material.

Nitrogen sorption measurements were performed on a Quantachrome Quadrasorb SI porosimeter using nitrogen as adsorbate at 77 K. The apparent surface area was calculated based on the BET (Bruanauer-Emmett-Teller) method of the adsorption branch.. The pore size distributions were determined by using the non-local density functional theory (NLDFT) model of both the adsorption and desorption branch. Prior to the measurements, the samples were degassed at 150 °C under vacuum for 20 hours.

Fourier transform infrared spectroscopy

The Fourier transform infrared (FTIR) spectroscopy allows for the characterization of molecular structures and is useful to identify functional groups. It is based on the interaction of infrared radiation with matter and the absorption of particular wavelengths, hence causing vibrational and vibrational-rotational transitions in the molecules. In order to absorb infrared radiation, the frequency of the incoming radiation has to match the frequency of a vibrational mode. Furthermore, the electric dipole moment of the molecule must change during the vibrations. In general, the resonance frequency is significantly related to the atomic mass and to the bond strength. In this context, vibrations can involve stretching or bending of the molecule i.e. change in bond length and bond angle, respectively, whereby the stretching vibrations can further be symmetrical (i.e. in phase) or asymmetrical (out-of-phase), as shown in **Figure 7.2**. IR spectra are commonly presented as the percentage transmittance of the radiation plotted against the wavenumber. Each band observed in a spectrum is characteristic of a specific molecule or atoms and relates to the particular stretching, bending or deformation movement.

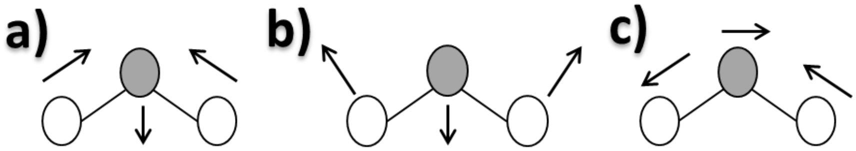

Figure 7.2 Schematic representation of possible vibration modes of a non-linear polyatomic molecule showing a) symmetric stretching, b) bending, and c) asymmetric stretching.

Depending on the wavenumber, it is distinguished between three different regions: the far-infrared (< 400 cm^{-1}), mid-infrared (4000-400 cm^{-1}) and near-infrared region (13000-4000 cm^{-1}).

Each region is associated with specific group frequencies, i.e. with vibration bands characteristic of certain functional groups and molecules. For instance, absorptions observed in the far-infrared region are mostly attributed to vibrations of molecules possessing heavy atoms as well as crystal lattice vibrations. The mid-infrared region mostly shows absorption bands attributed to X-H stretching (X = O, C, N) as well as double- and triple bonds. Absorption bands observed in the region around 1500-650 cm^{-1} are commonly regarded as a fingerprint of a whole molecule, which is why this spectral region is referred to as the fingerprint region. The near-infrared region involves combinations of the fundamental vibration bands due to C-H, N-H or O-H stretching, among others.

FTIR measurements were performed using a Varian 600FTIR Spectrometer equipped with an ATR support.

Ultraviolet-visible spectroscopy

Ultraviolet-visible spectroscopy (UV-Vis) represents a further absorption spectroscopy and deals with the UV and visible region of the electromagnetic spectrum. In this spectral region (i.e. UV range: 200-400 nm, and Vis range: 400-800 nm), atoms and molecules can undergo electronic transitions. In general, when light is passed through a sample molecule, parts of its energy will be absorbed by the molecules. Depending on the wavelength, i.e. when the energy of the incoming light matches the energy required for a certain electronic transition, energetically favored electrons will be excited from the highest occupied molecular orbital (HOMO) to the lowest unoccupied molecular orbital (LUMO). The possible electronic transitions are shown in **Figure 7.3** in dependence of the energy.

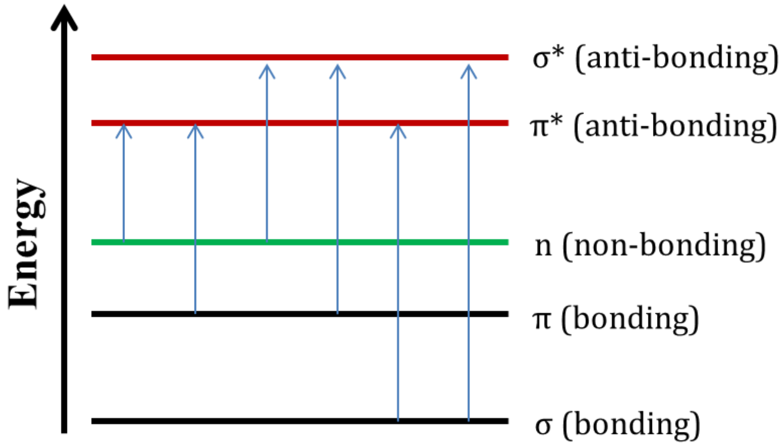

Figure 7.3 Schematic representation of the electronic orbital energies showing different types of electronic transitions upon absorption of light energy.

The resulting UV-Vis spectrum, which is commonly shown as the plot of the absorbance (A) vs. the wavenumber (cm^{-1}), reflects the wavenumbers at which absorption occurs as well as the degree of absorption at each wavenumber and thus provides insights into the molecular structure and geometry.

UV-Vis spectroscopy measurements were performed on a Varian 50Conc UV-Vis spectrometer equipped with neoLab semi-micro polystyrene cuvettes.

Scanning electron microscopy

The scanning electron microscopy (SEM) is a microscopy technique which is widely applied for the imaging and characterization of materials' surface topology down to the nanometer scale. It basically involves the interaction of an electron beam with the specimen and the detection of secondary electrons i.e. electrons which are released from the specimen's surface. In order to achieve an efficient electron release and to avoid accumulation of electrostatic charge at the surface, the materials should preferably be conductive. However, non-conductive materials can be sputtered with a conductive compound (commonly platinum, gold or silver) in order to generate a conductive surface suitable for SEM measurements.

SEM images were recorded on a LEO 1550 Gemini microscope and the samples were puttered with platinum prior to the measurements.

Transmission electron microscopy

The transmission electron microscopy (TEM) represents a further efficient and widely-applied microscopy technique which is suitable for the visualization of particles down to 1 nm. Here, an electron beam is focused on an ultrathin section of the specimen which is suspended on a grid and the respective image is obtained from the detection of the transmitted electrons. The resulting image is visualized onto an imaging device (e.g. a fluorescent screen or a photographic films).Thereby, the contrast of the image strongly relates to the thickness of the prepared sample as well as on the electron density, i.e. sample regions containing heavier elements scatter more and hence appear darker whereas regions with lighter elements are shown brighter.

TEM images were recorded on a Zeiss EM 912Ω microscope operating at an acceleration voltage of 120 kV.

Elemental analysis

The elemental analysis (EA) is a facile combustion method which allows for the quantitative determination of the elemental composition of materials with regard to carbon, nitrogen, sulfur and hydrogen. Therefore, the materials of investigation are burnt in O_2 atmosphere at elevated temperatures and possible decomposition gases such as CO_2, H_2O, SO_3, and N_2 are consequently detected and quantified by heat conductance detectors.

Inductive Coupled Plasma-Optical Emission Spectroscopy (ICP-OES) is applied for the quantitative determination of further elements (e.g. metals). It is based on the element-characteristic atom spectra and involves the use of argon plasma to induce the emission of atoms and ions.

Elemental analysis was conducted on a Vario Micro instrument. ICP-OES measurements were performed on a ICP-OES Optima 2100 DV device from Perkin Elmer.

Thermogravimetric Analysis Differential Scanning Calorimetry

Thermogravimetric analysis (TGA) allows monitoring the thermal degradation and decomposition profile of a material while heating to a certain degree in either inert or oxygen atmosphere.
Differential scanning calorimetry (DSC) is mostly applied in combination with the TGA method and used to detect the phase transitions during the heating process. Therefore, the heat flow is measured in comparison to a reference sample, thus showing endothermal or exothermal reactions.

TGA data were recorded on a Netzsch TG 209 F1 device using Al_2O_3 crucibles. Here, the samples were heated to 1000 °C in a nitrogen atmosphere at a heating rate of 10 C min^{-1}.

Electrochemistry

The cyclic voltammetry (CV) is commonly applied to study the electrochemical properties of analytes. It is based on the measurement of the current which results between two electrodes within a defined potential window, whereby the applied potential is swept at a constant sweep rate. The resulting current is consequently measured as a function of the potential. In general, CV data can provide thermodynamic and kinetic information in terms of the redox potentials, equilibrium constants and electrochemical reaction rates, among others.

Herein, electrochemical measurements were performed using a two electrode Swagelok-cell on a Bio-Logic VMP3 device. The specific capacity C was calculated using following equation:

$$\boldsymbol{C = \frac{2}{\Delta V \cdot v \cdot m} \cdot \int I dV} \qquad \textbf{(7.3)}$$

where I (A) is the current, ΔV (V) the potential difference, m (g) is the sample mass and v (V s^{-1}) is the scan rate.

B. Experimental part

Synthesis of 3D crystals based on coordination compounds

Chemicals

3,4-Dihydroxy-3-cyclobutene-1,2-dione (squaric acid, SA, 98.5-101.00 %) and nickel acetate tetrahydrate (NAT, 98%) were purchased from Sigma-Aldrich. Zinc acetate dihydrate (ZAD, > 99.5 %) and nickel nitrate hexahydrate were purchased from Carl Roth. 4,5-dihydroxycyclopentenetrione (croconic acid, CA, 98%) and cobalt acetate tetrahydrate (CoAT, 98%) were obtained from Alfa Aesar. Cadmium acetate dihydrate (CdAD, 98%) was obtained from Acros Organics, respectively. Cupric acetate monohydrate (CuAM, > 99%) and 1 *M* hydrochloric acid (HCl) were purchased from Flaka Chemika and Merck, respectively. All reagents were used as received, without further purification. Deionized water was used throughout the experiments.

Squarate-zinc based coordination compounds

In a typical synthesis, squaric acid (518 mg, 4.54 mmol) was dissolved in 30 mL deionized water at 80 °C and ZAD (997 mg, 4.54 mmol) was dissolved in 10 mL deionized water at room temperature. The ZAD solution was added to the SA solution after the latter was cooled to RT. The subsequently precipitated colorless crystals were aged at the respective temperature overnight, whereby for aging at 2 °C the samples were placed in a conventional lab fridge and for aging at 80 °C in a conventional lab oven, respectively. After decantation and washing three times with 50 mL deionized water, the sample was dried overnight in vacuum at 60 °C. Throughout this thesis, the resulting crystalline particles are denoted as SAZn_R_T, where R refers to the SA/Zn molar ratio and T to the aging temperature.

Squarate-copper based coordination compounds

Squaric acid (518 mg, 4.54 mmol) was dissolved in 30 mL deionized water at 80 °C and CuAM (907 mg, 4.54 mmol) was dissolved in 10 mL deionized water at room temperature. The CuAM solution was added to the SA solution after the latter was cooled to RT. The subsequently precipitated colored crystals were aged at the respective temperature overnight, whereby for aging at 2 °C the samples were placed in a conventional lab fridge and for aging at 80 °C in a conventional lab oven, respectively. After decantation and washing three times with 50 mL deionized water, the sample was dried overnight in vacuum at 60 °C. Throughout this thesis, the resulting crystalline particles are denoted as SACu_R_T, where R refers to the SA/Cu molar ratio and T to the aging temperature.

Squarate-nickel based coordination compounds

Squaric acid (518 mg, 4.54 mmol) was dissolved in 30 mL deionized water at 80 °C and NiAT (1130 mg, 4.54 mmol) was dissolved in 10 mL deionized water at room temperature. The NiAT solution was added to the SA solution after the latter was cooled to RT. The subsequently precipitated colored crystals were aged at the respective temperature for one hour, whereby for aging at 2 °C the samples were placed in a conventional lab fridge and for aging at 80 °C in a conventional lab oven, respectively. After decantation and washing three times with 50 mL deionized water, the sample was dried overnight in vacuum at 60 °C. The resulting green crystals are denoted as SANi_R_T, where R refers to the SA/Ni molar ratio and T to the aging temperature.

Squarate-cobalt based coordination compounds

Squaric acid (518 mg, 4.54 mmol) was dissolved in 30 mL deionized water at 80 °C and CoAT (1131 mg, 4.54 mmol) was dissolved in 10 mL deionized water at room temperature. The CoAT solution was added to the SA solution after the latter was cooled to RT. The subsequently precipitated colored crystals were aged at the respective temperature for one hour, whereby for aging at 2 °C the samples were placed in a conventional lab fridge and for aging at 80 °C in a conventional lab oven, respectively. After decantation and washing three times with 50 mL deionized water, the sample was dried overnight in vacuum at 60 °C. The resulting crystals are denoted as SACo_R_T, where R refers to the SA/Co molar ratio and T to the aging temperature.

Squarate-cadmium based coordination compounds

Squaric acid (518 mg, 4.54 mmol) was dissolved in 30 mL deionized water at 80 °C and CdAD (1210 mg, 4.54 mmol) was dissolved in 10 mL deionized water at room temperature. The CdAD solution was added to the SA solution after the latter was cooled to RT. The subsequently precipitated colored crystals were aged at the respective temperature for one hour, whereby for aging at 2 °C the samples were placed in a conventional lab fridge and for aging at 80 °C in a conventional lab oven, respectively. After decantation and washing three times with 50 mL deionized water, the sample was dried overnight in vacuum at 60 °C. The resulting green crystals are denoted as SACd_R_T, where R refers to the SA/Cd molar ratio and T to the aging temperature.

Croconate-zinc based coordination compounds

In a typical synthesis, croconic acid (CA, 518 mg, 3.65 mmol) was dissolved in 30 mL deionized water and ZAD (800 mg, 3.65 mmol) was dissolved in 10 mL deionized water at RT, respectively. The two solutions were then mixed at RT and the subsequently precipitated colored crystals were aged at 80 °C overnight. After decantation and washing three times with 50 mL deionized water, the sample was dried overnight in vacuum at 60 °C. The resulting crystals are named CAZn_1_80.

Synthesis of nanoporous composite materials

The composite materials based on the coordination compounds of the squarate with various metal ions were obtained by transferring the crystalline SAX_R_T precursor to a ceramic crucible followed by heat treatment in N_2 atmosphere. The oven was flushed with N_2 for 30 min at room temperature prior to the heating. The samples were then heated to 900 °C at a heating rate of 10 °C min^{-1}. After holding the final temperature for 1h, the samples were allowed to cool down to room temperature. The hereby obtained composite is denoted as SAX_R_T_CM, where X refers to the metal ion (X= Zn, Cu, Ni and Co, respectively) and the extension CM indicates composite material.

Synthesis of nanoporous carbon materials

The nanoporous carbon materials were obtained by washing the respective composite materials in 200 mL of a 1 *M* HCl solution, followed by filtration, washing with 300 mL deionized water and drying in vacuum at 60 °C overnight. The hereby obtained porous carbon materials are denoted as SAX_R_T_PC, whereby PC indicates porous carbon.

Alternatively, direct heat treatment of the crystalline precursors based on squarate-zinc as well as croconate-zinc coordination compounds at 1000 °C in N_2 atmosphere yielded the respective hierarchically porous carbons without the requirement of an additional washing step. The resulting carbons are named SAZn_1_80_DPC and CAZn_1_80, respectively.

Synthesis of the composite catalyst Ni@SAZn_PC

Herein, the nanoporous carbon SAZn_1_80_PC was used as support material and decorated with NiNPs via an incipient wetting impregnation. Therefore, $Ni\,(NO_3)_2$ (50 mg, 0.27 mmol) was dissolved in 154 µL H_2O and added dropwise to 100 mg SAZn_1_80_PC. The sample was then transferred to a ceramic crucible reduced in a H_2/Ar stream (5 vol. % H_2) with a flow rate of 5 $dm^3\ h^{-1}$ at 475 °C for three hours.

Electrochemical analysis

Herein, the nanoporous carbon SAZn_1_80_PC was used as supercapacitor electrode material. For the preparation of the working electrodes, a sonicated suspension consisting of 95 wt% of the carbon SAZn_1_80_PC, 5 wt% binder (poly ionic liquid, PILs)[19] and 100 µl methanol was drop-casted on a platinum disc. After the methanol was evaporated, the electrode ink was dried for 60 min at 60 °C. Subsequently, 5.0 mg of the carbon material were loaded on each electrode with an area of 0.785 cm^2. Afterwards, the two carbon electrodes were assembled in a Swagelok-cell, whereby the two electrodes were separated by a filter paper which was soaked with 50 µL of 1 *M* H_2SO_4, which was used as electrolyte. Cyclic voltammetry (CV) experiments were conducted using scan rates from 5-200 mV s^{-1}, whereby the voltage window was set to 1 V.

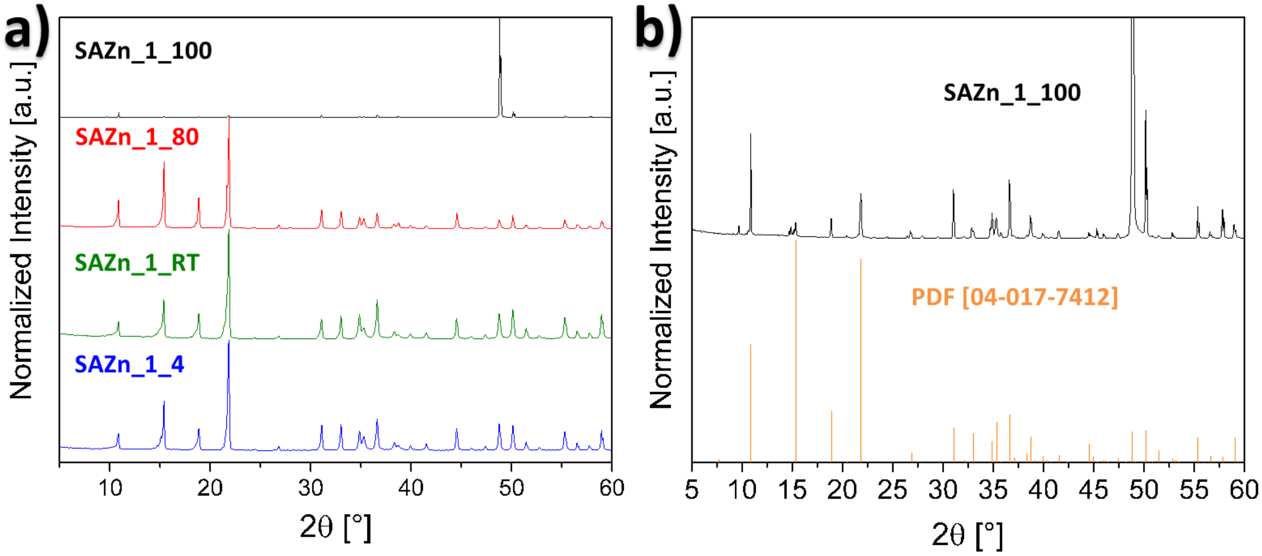

Figure S 1 XRD diffractograms of the crystals aged at different temperatures showing in a) SAZn_1_4 (blue), SAZn_1_RT (green), SAZn_1_80 (red), and SAZn_1_100 (black). (b) XRD pattern of SAZn_1_100 (black) and the reference pattern PDF [04-017-7412].

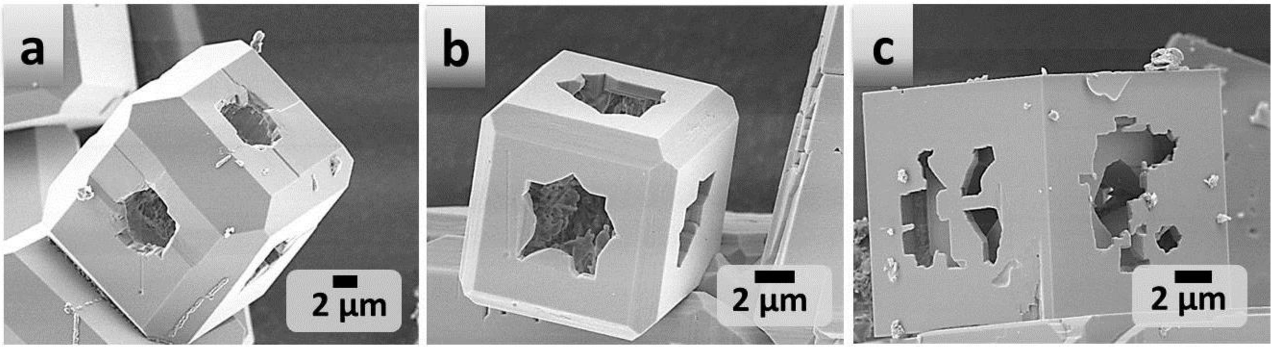

Figure S 2 SEM micrographs of the crystalline particles of the squarate-zinc coordination complexes aged at 80 °C at different SA/Zn molar ratios. a) SAZn_05_80, b) SAZn_1_80, and c) SAZn_2_80.

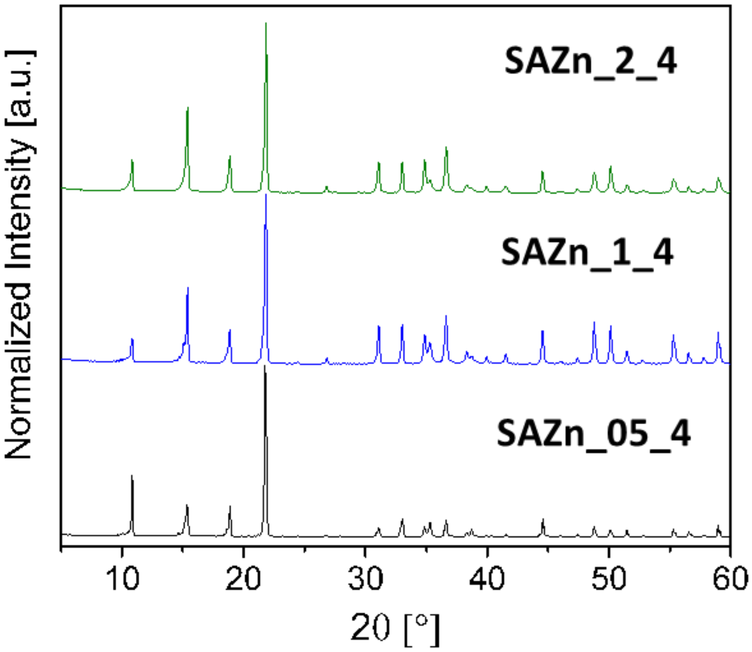

Figure S 3 XRD diffractograms of the crystals of the squarate-zinc coordination complexes aged at 4 °C at different SA/Zn molar ratios, showing SAZn_05_4 (black), SAZn_1_4 (blue), and SAZn_2_4 (green).

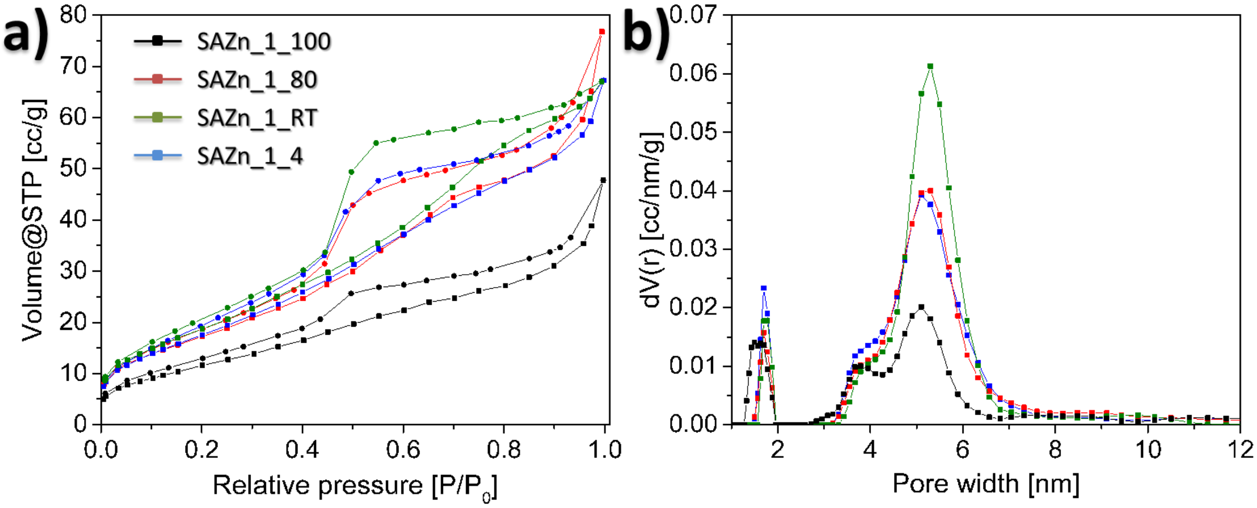

Figure S 4 a) Nitrogen sorption isotherms of the porous crystals of the squaric-zinc coordination compounds aged at different temperatures with SAZn_1_4 (blue), SAZn_1_RT (green), SAZn_1_80 (red) and SAZn_1_100 (black). b) The corresponding PSD curves cylindrical pores.

Table S 1 Nitrogen sorption data for the porous crystals of the squaric-zinc coordination compounds aged at different temperatures.

Compound	S_{BET} [m^2 g^{-1}]	**Pore volume [cm^3 g^{-1}]**		
		Total	*Micro*	*Meso*
SAZn_1_100	45	0.07	0.02	0.05
SAZn_1_80	67	0.12	0.03	0.09
SAZn_1_RT	70	0.11	0.03	0.08
SAZn_1_4	67	0.1	0.03	0.07

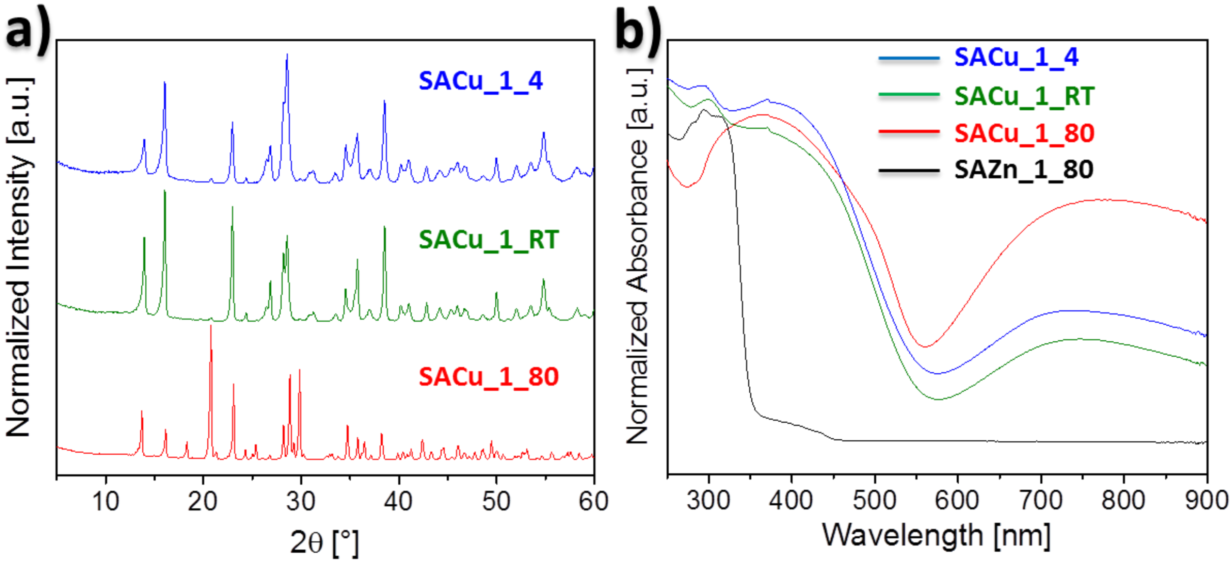

Figure S 5 a) XRD diffractograms of the crystals based on squarate-copper coordination complexes aged at different temperatures with SACu_1_4 (blue), SACu_1_RT (green) , and SACu_1_80 (red). b) UV-Vis spectra of the respective squarate-copper coordination complexes as well as SAZn_1_80 (black).

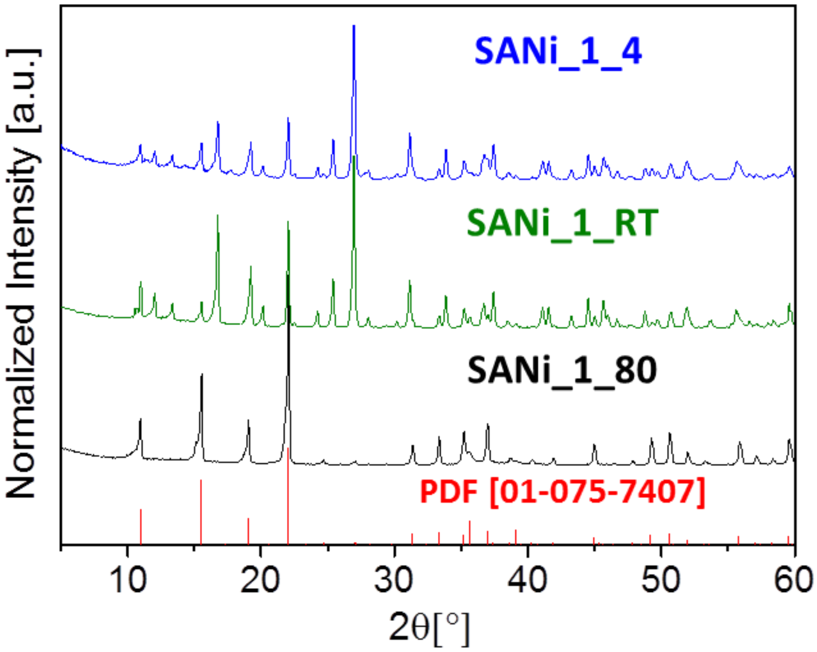

Figure S 6 XRD diffractograms of the crystals based on squarate-nickel coordination complexes aged at different temperatures with SANi_1_4 (blue), SANi_1_RT (green), SANi_1_80 (black), and the reference pattern PDF[04-017-7412] (red).

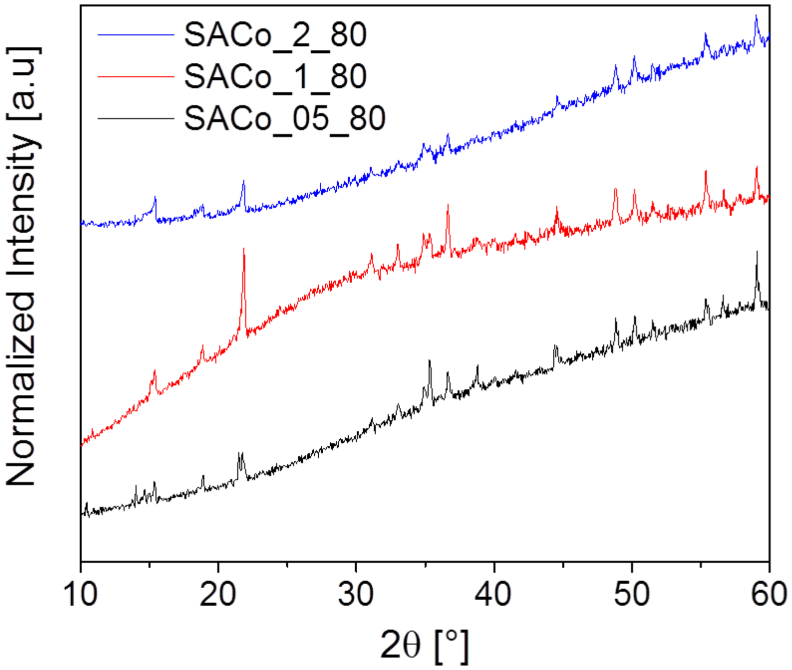

Figure S 7 XRD diffractograms of the squarate-cobalt complexes prepared at various molar ratio and aged at 80 °C with SACo_05_80 (black), SACo_1_80 (red), and SACo_2_80 (blue).

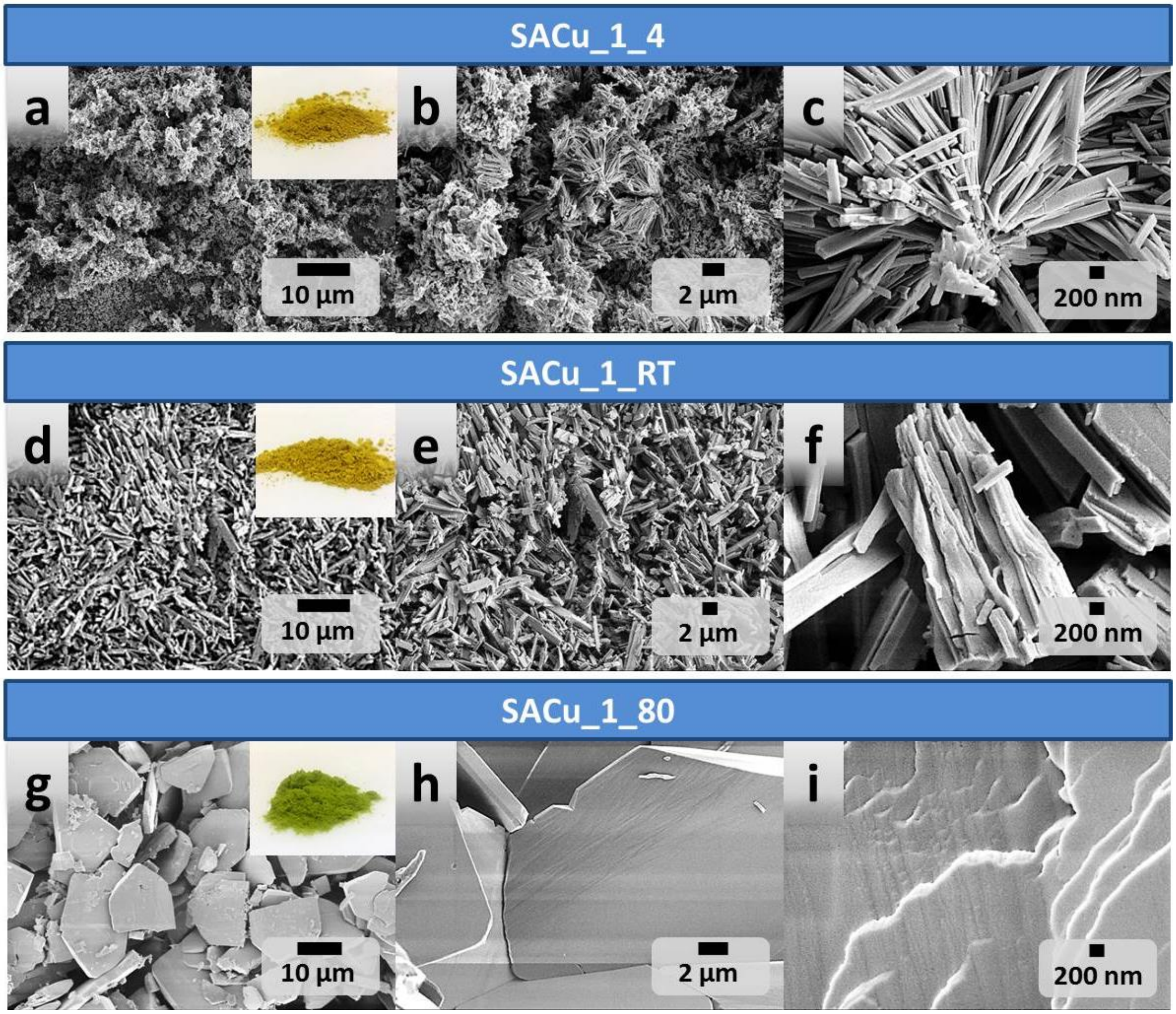

Figure S 8 SEM micrographs of the squarate-copper complexes prepared at various aging temperatures with a-c) SACu_1_4, d-f), SACu_1_RT, and g-i) SACu_1_80. The insets in a, d and g show the colored microcrystalline powders samples of the complexes SACu_1_4, SACu_1_RT and SACu_1_80, respectively.

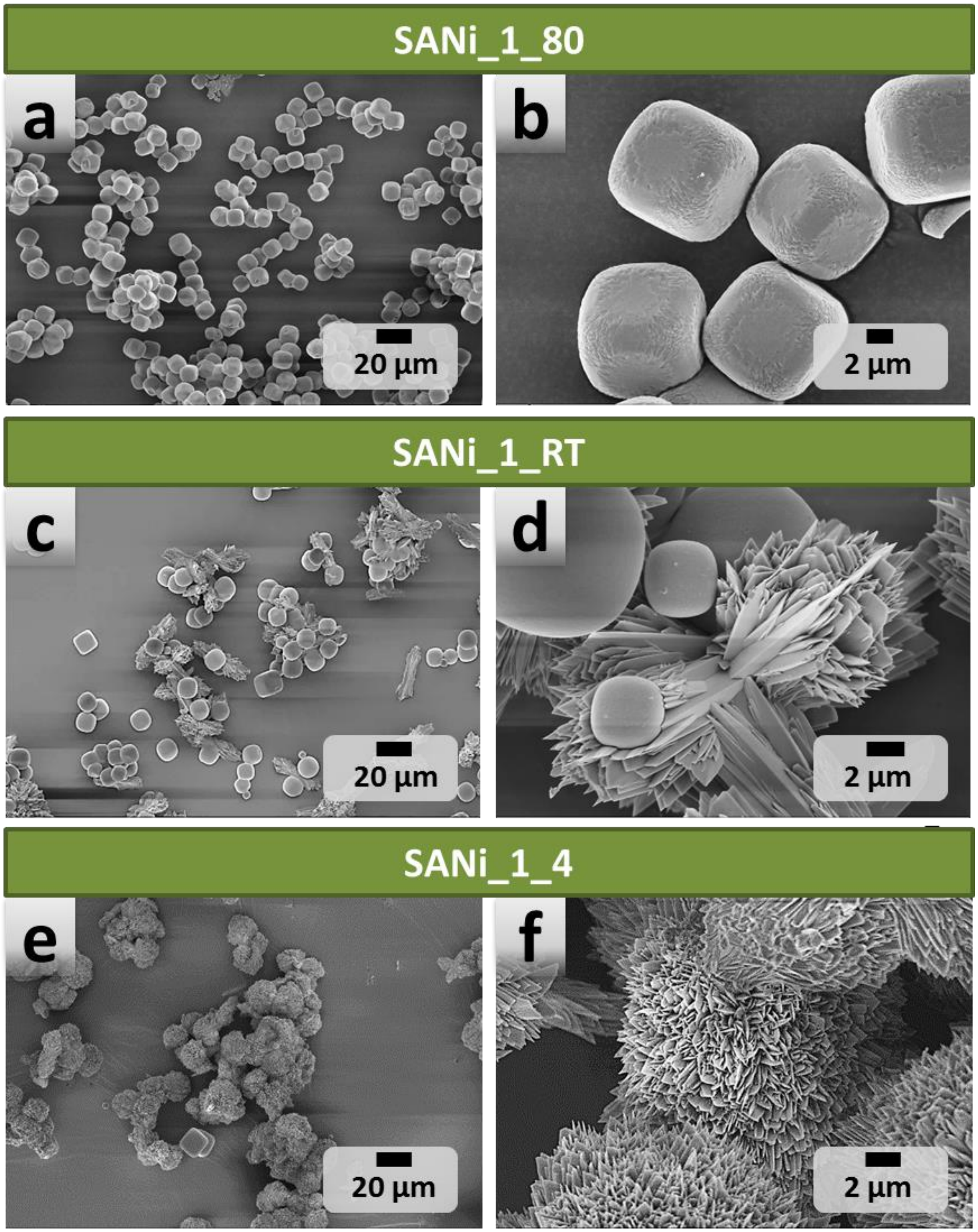

Figure S 9 SEM micrographs of the squarate-nickel complexes prepared at various aging temperatures with a, b) SANi_1_80, c, d), SANi_1_RT, and e, f) SANi_1_4.

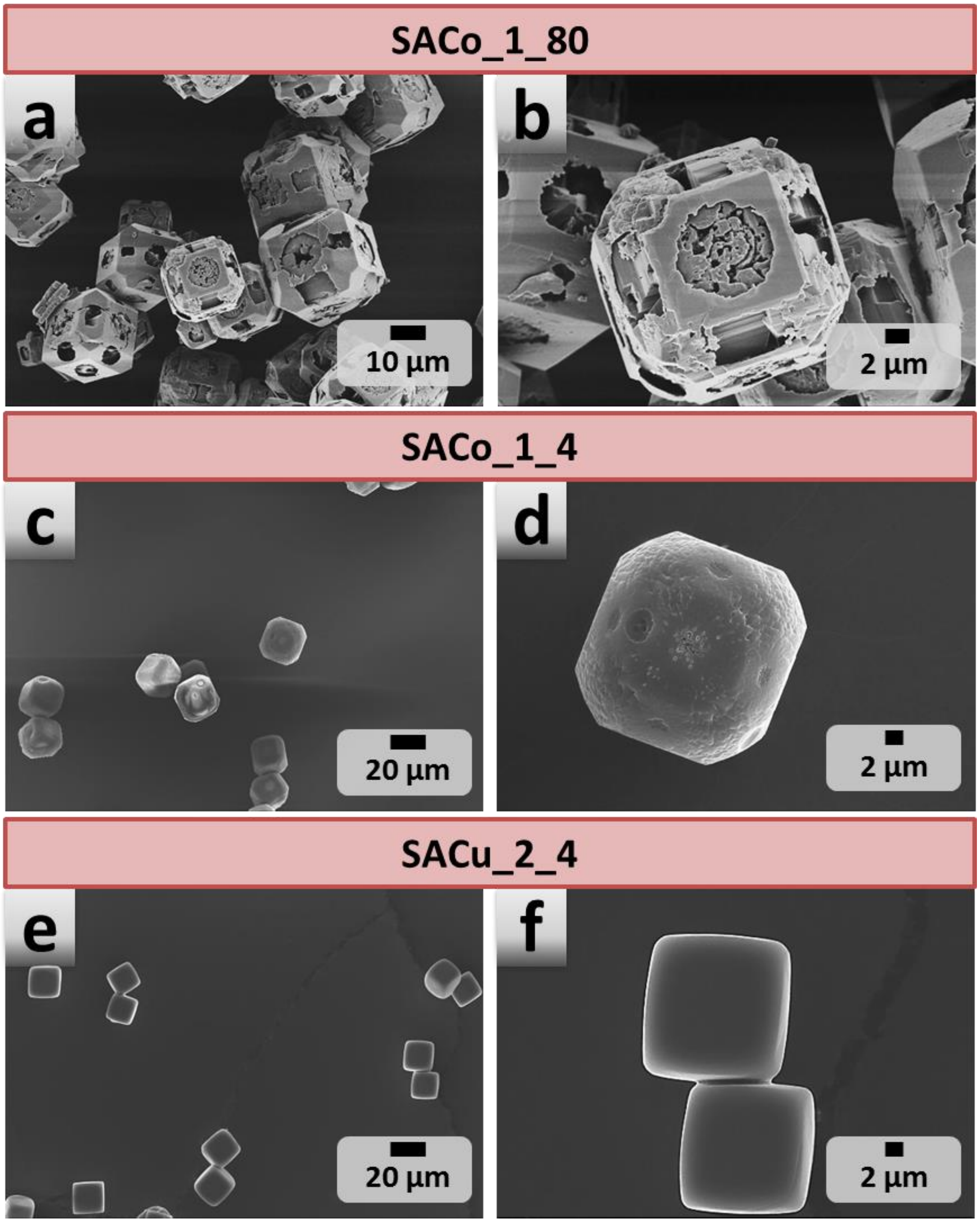

Figure S 10 SEM micrographs of the squarate-cobalt complexes prepared at various aging temperatures with a, b) SACo_1_80, c, d) SACo_1_RT, and e, f) SACo_1_4.

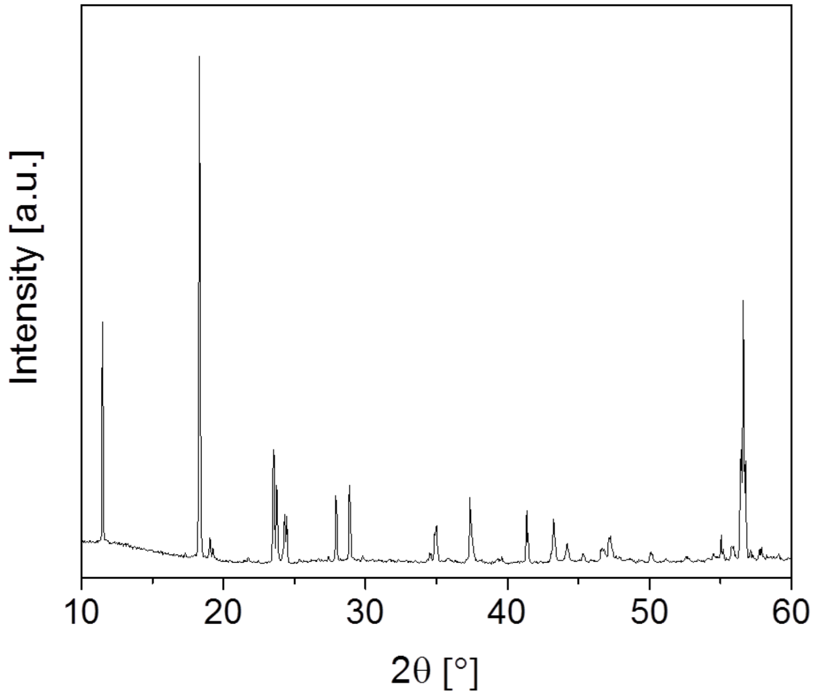

Figure S 11 XRD diffractogram of CAZn_1_80 crystals.

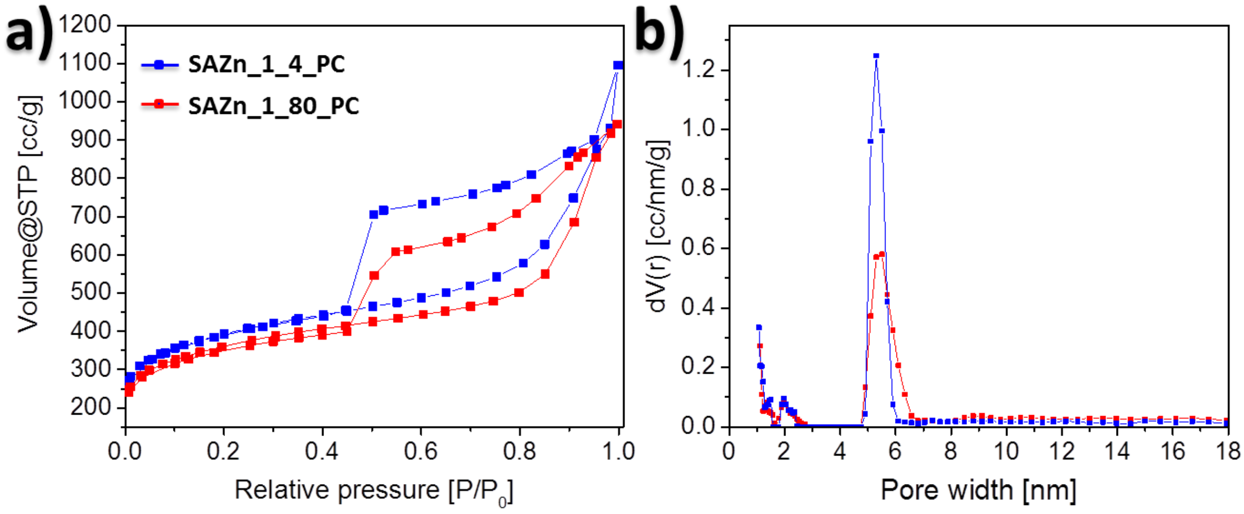

Figure S 12 a) Nitrogen sorption isotherms of the porous carbons SAZn_1_4_PC (blue) and SAZn_1_80_PC (red). b) Corresponding PSD curves calculated based on the QSDFT model for slit and cylindrical pores.

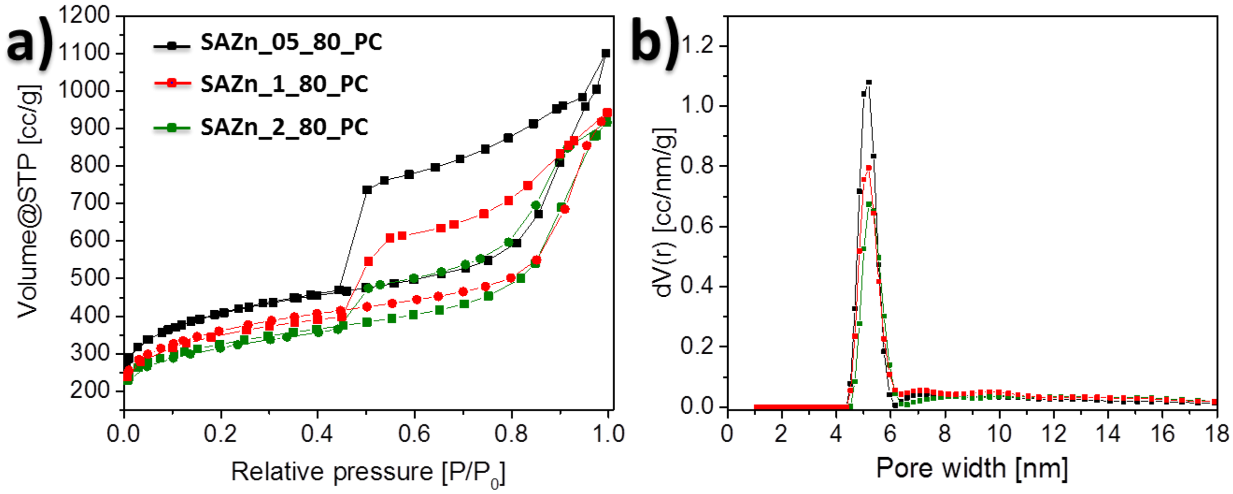

Figure S 13 a) Nitrogen sorption isotherms of the porous carbons SAZn_05_80_PC (black), SAZn_1_80_PC (red) and SAZn_2_80_PC (green). b) Corresponding PSD curves calculated based on the QSDFT model for slit and cylindrical pores.

Table S 2 Nitrogen sorption data for the porous composites and carbon materials derived from the squaric-zinc coordination compounds aged at various temperatures as well as various molar ratios..

Compound	**S_{BET} [$m^2 g^{-1}$]**	**Total pore volume [$cm^3 g^{-1}$]**
SAZn_05_80_CM	580	0.72
SAZn_1_80_CM	519	0.71
SAZn_2_80_CM	488	0.62
SAZn_05_4_CM	726	0.89
SAZn_1_4_CM	519	0.62
SAZn_2_4_CM	366	0.58
SAZn_05_80_PC	1462	1.71
SAZn_1_80_PC	1296	1.46
SAZn_2_80_PC	1223	1.62
SAZn_1_4_PC	1416	1.7
SAZn_2_4_PC	1277	1.48

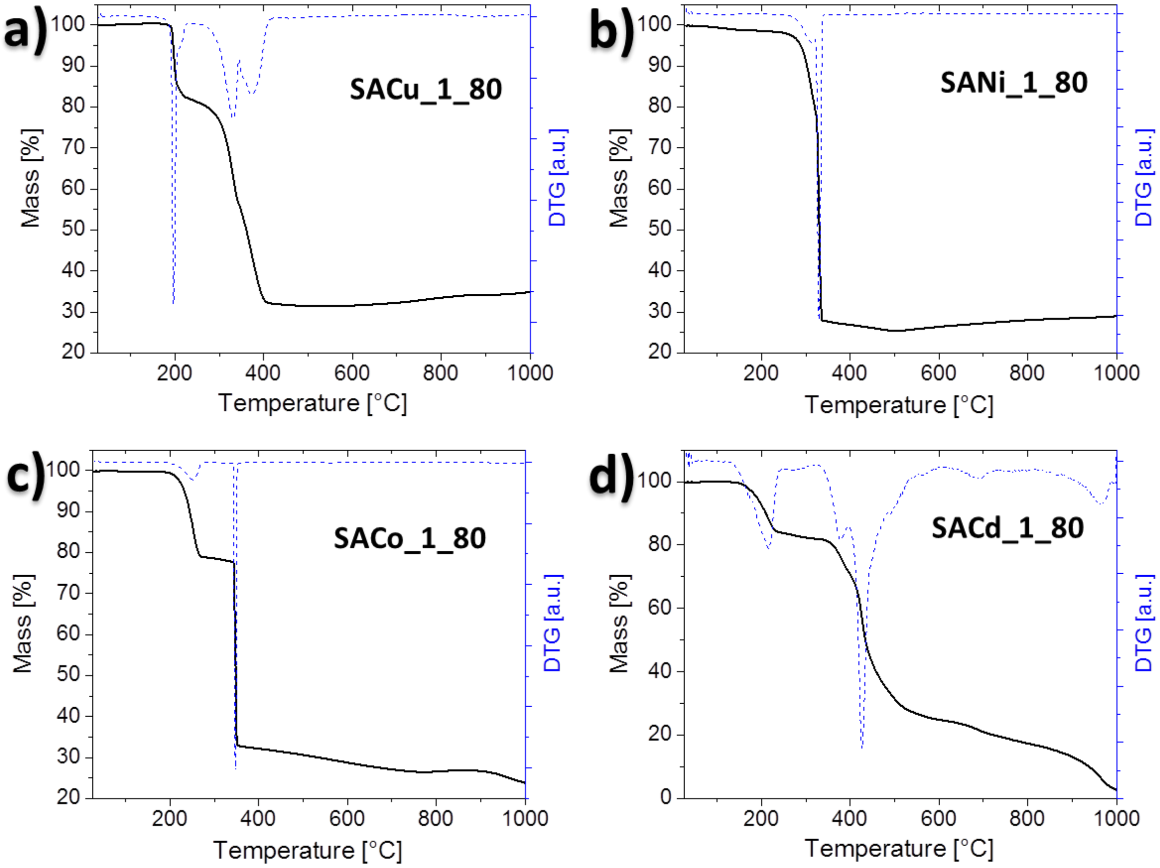

Figure S 14 TGA curves (solid black line) and DTG curves (dashed blue line) of the coordination complexes a) SACu_1_80, b) SANi_1_80, c) SACo_1_80, and d) SACd_1_80. All samples were heated from room temperature to 1000 °C under N_2 atmosphere at a heating rate of 10 °C min^{-1}.

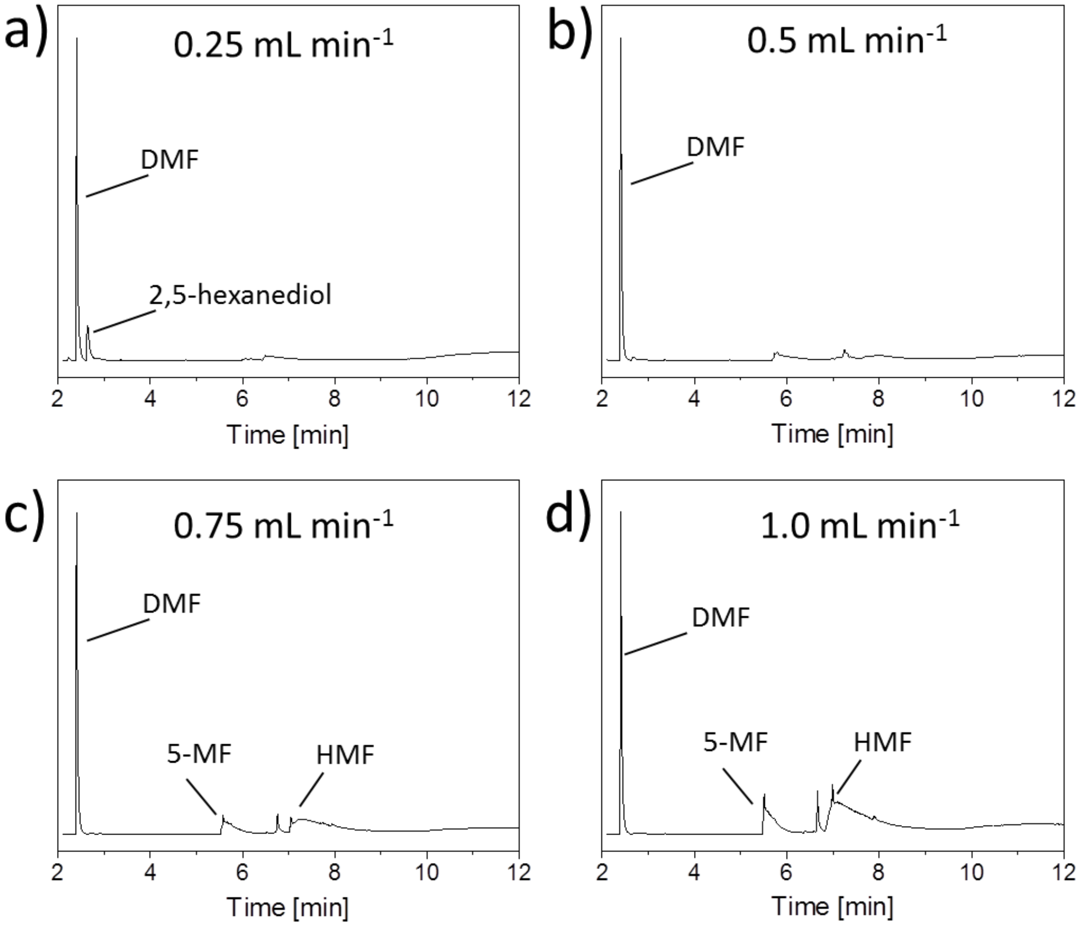

Figure S 15 GC-chromatogram for the hydrogenolysis of HMF to DMF using the catalyst Ni@SAZn_PC at different flow rates, a) 0.25 mL min^{-1}, b) 0.5 mL min^{-1}, c) 0.75 mL min^{-1}, and d) 0.1 mL min^{-1}.

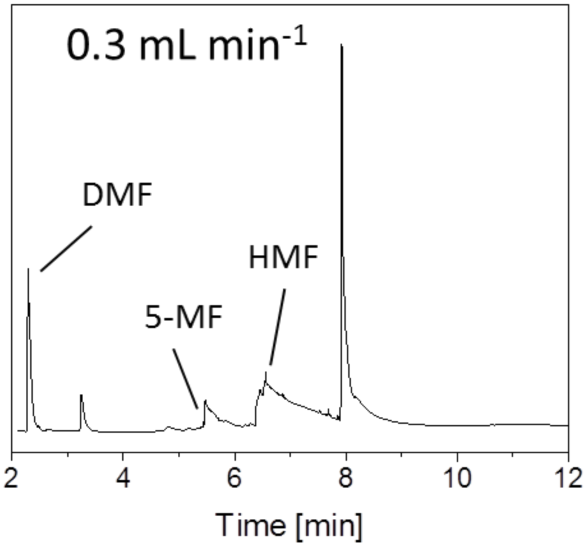

Figure S 16 GC-chromatogram for the hydrogenolysis of HMF to DMF using the catalyst SANi_CM at a flow rates of 0.m mL min^{-1}.

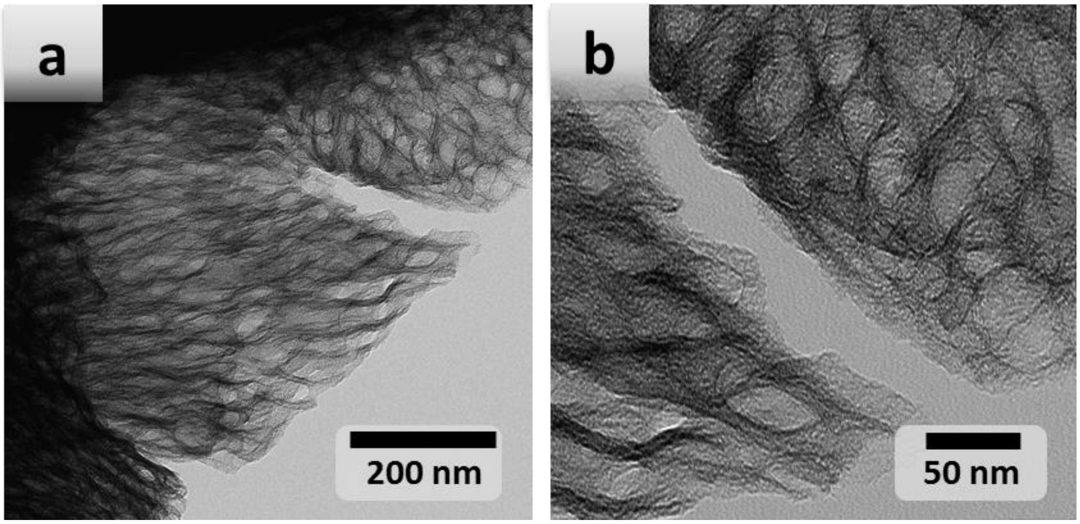

Figure S 17 TEM images of the porous carbon SAZn_1_80_PC.

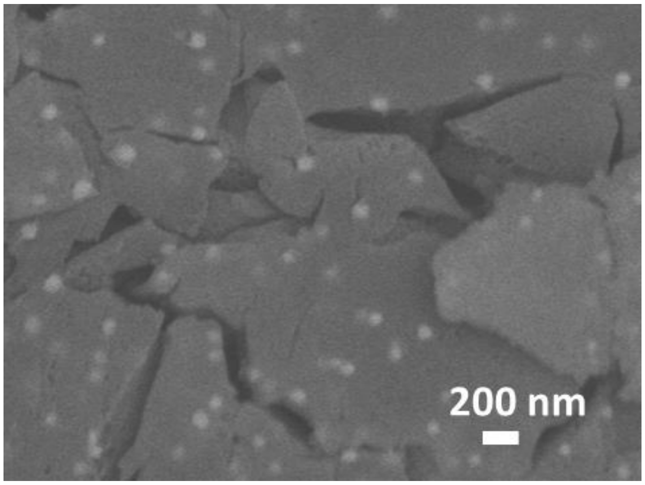

Figure S 18 SEM image of the composite the catalyst Ni@SAZn_PC recovered after 15 h reaction. Reproduced from Mani *et al.* with the permission from Wiley.[224]

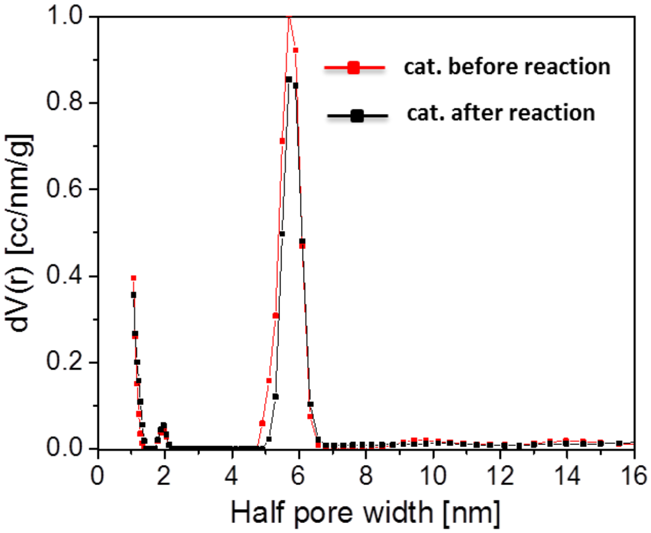

Figure S 19 PSD curves of the catalyst Ni@SAZn_PC before the reaction (red) and recovered after 15 h reaction (black).

D. List of abbreviations

BET	Brunauer-Emmet-Teller
CFT	Crystal Field Theory
EA	Elemental analysis
EDLC	Electric double-layer capacitor
FTIR	Fourier transform infrared spectroscopy
HKUST	Hong Kong University of Science & Technology
HTC	Hydrothermal carbonization
ICDD	International Centre for Diffraction Data
ICP-OES	Inductively coupled plasma optical emission spectroscopy
IL	Ionic liquid
IUPAC	International Union of Pure Applied Chemistry
LFSE	Ligand Field Stabilization Energy
MIL	Matériaux de l'Institut Lavoisier
MOF	Metal-organic framework
MS	Mass spectroscopy
NICS	Nucleus-independent chemical shift
Ni-NP	Nickel nanoparticle
NLDFT	Non-local density functional theory
OM	Optical microscope
ORR	Oxygen reduction reaction
PB	Prussian blue
PSD	Pore size distribution
RT	Room temperature

SA	Squaric acid
SEM	Scanning electron microscopy
TGA	Thermogravimetric analysis
XRD	X-ray diffraction
ZAD	Zinc acetate dihydrate
ZIF	Zeolitic imidazolate framework

E. List of publications

C. Mbaya Mani, M. Braun, V. Molinari, M. Antonietti, N. Fechler, “A high-throughput composite catalyst based on Nickel carbon cubes for the hydrogenation of 5-hydroxymethylfurfural to 2,5-dimethylfuran”, *ChemCatChem* **2017**, *9*, 3388-3394.

C. Mbaya Mani, T. Berthold, N. Fechler, „Cubism on the Nanoscale: From Squaric Acid to Porous Carbon Cubes”, *Small* **2016**, *12, No. 21*, 2906-2912.

T. Franken, **C. Mbaya Mani**, R. Palkovits, „Crystalline ordered mesoporous $Cu_{0.25}Co_{2.75}O_4$ prepared with selected mesoporous silica templates and their performances as DeN_2O catalysts“, *Journal Microporous and Mesoporous Materials* **2016**, *221*, 91-100.

F. Declaration

Hiermit erkläre ich, dass die vorliegende Dissertation selbstständig angefertigt wurde und keine anderen als die angegebenen Hilfsmittel und Quellen verwendet wurden.

I hereby declare that I have written this dissertation independently, without assistance from external parties and without use of other sources than those indicated.

Christian Mbaya Mani

Potsdam, 29.09.2017